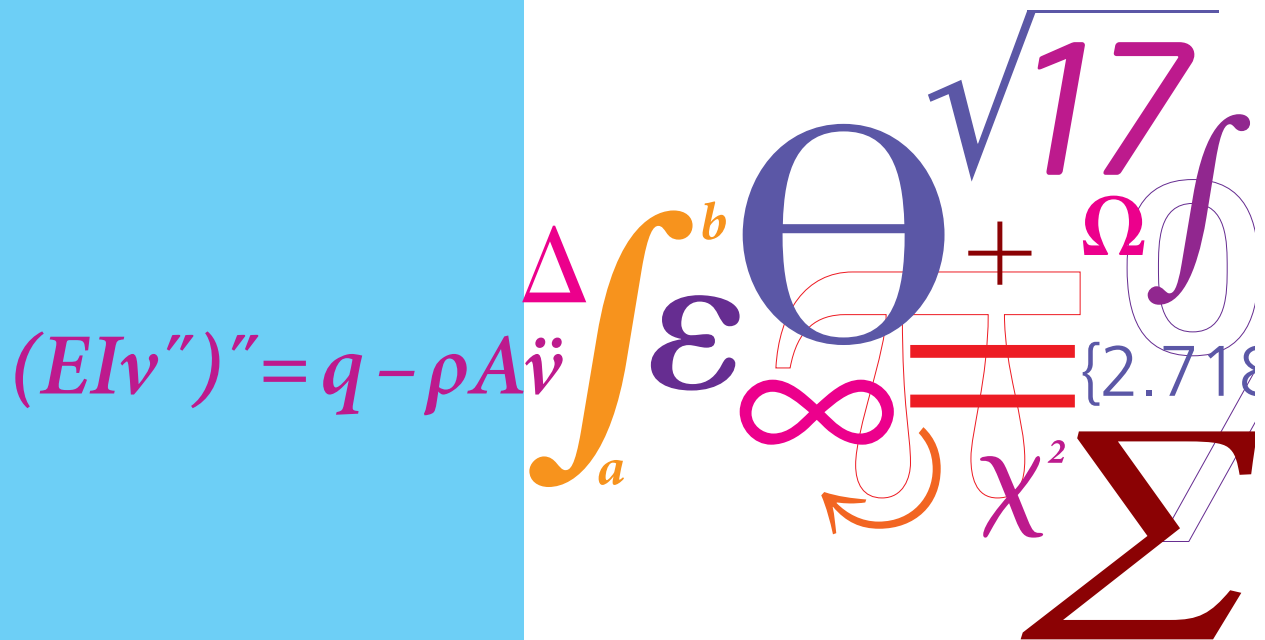


Wave Manipulation by Topology Optimization

PhD Thesis



Jacob Andkjær
 DCAMM Special Report No. S140
 January 2012

Wave manipulation by topology
optimization

by

Jacob Andkjær

DEPT. OF MECHANICAL ENGINEERING
Solid Mechanics



TECHNICAL UNIVERSITY OF DENMARK

Title of the thesis:

Wave manipulation by topology optimization

Ph.D. student:

Jacob Andkjær

E-mail: jban@mek.dtu.dk

Supervisors:

Ole Sigmund

E-mail: sigmund@mek.dtu.dk

Olav Breinbjerg

E-mail: ob@elektro.dtu.dk

N. Asger Mortensen

E-mail: namo@fotonik.dtu.dk

Address:

Department of Mechanical Engineering, Solid Mechanics

Technical University of Denmark

Nils Koppels Allé, Building 404, 2800 Kgs. Lyngby, Denmark

Preface

This thesis is submitted in partial fulfillment of the requirements for obtaining the degree of Ph.D. in mechanical engineering at the Technical University of Denmark (DTU). The Ph.D. project was funded by DTU and the Danish Council for independent Research | Technology and Production Sciences (FTP) through the project: "Topology Optimization of Electromagnetic Metamaterials for Miniaturization of Wireless Communication Antennas (TopAnt)". The work was carried out at the Department of Mechanical Engineering, Solid Mechanics, at DTU in the period February 1st 2009 - January 31st 2012. Supervisors on the project were Professor Dr.techn. Ole Sigmund (Department of Mechanical Engineering), Professor Dr.techn. N. Asger Mortensen (Department of Photonics Engineering) and Professor Ph.D. Olav Breinbjerg (Department of Electrical Engineering).

I am very grateful to my three supervisors for their inspiring support and for always taking their time to discuss the work and the results during the project.

Part of this work was carried out during a 10 months visit to Professor Ph.D. Shinji Nishiwaki and his research group at the Department of Mechanical Engineering and Science, Kyoto University, Japan, from March 2010 to December 2010. Ph.D. Tsuyoshi Nomura from Toyota Central R&D Labs., Inc. co-supervised me during my visit. I am very grateful to Professor Ph.D. Shinji Nishiwaki and Ph.D. Tsuyoshi Nomura for the supervision as well as making the stay possible and to my colleagues at Kyoto University for creating a friendly and welcoming atmosphere. I am also very thankful to Ph.D.-student Masaki Otomori for discussions on electromagnetic wave propagation during my visit to Kyoto University and his visit to DTU.

I am thankful to Krister Svanberg at Royal Institute of Technology, Sweden, who has granted me permission to use the MMA-code. Thanks to my colleagues in the TopOpt and TopAnt Group, at the section of Solid Mechanics and in particular the other phd-students for creating a cheerful and inspiring working environment.

Finally, I wish to thank my family and friends for their support. Special thanks to my girlfriend Maria Ota for her support and patience during the project.

Kgs. Lyngby, January 31st 2012.

Jacob Andkjær

Resumé (in Danish)

Lyd og lys udbreder sig i bølger og spredes, reflekteres og ændrer retning ved møde med andre medier og forhindringer. Ved at optimere udformningen og fordelingen af de medier bølgerne møder på deres vej kan man opnå nyttige og interessante effekter. Denne afhandling beskriver hvorledes topologioptimering kan anvendes til at designe strukturer for manipulering af elektromagnetiske og akustiske bølger. De betragtede bølge-problemer opdeles i tre klasser.

Den første klasse omhandler udformningen af en struktur, som når den er placeret rundt om et objekt, vil gøre objektet usynligt for en iagttager. I undersøgelsen er materialet i strukturen begrænset til materialer med isotropiske materiale parametre, der er let tilgængelige i naturen. Usynlighedseffekten for de optimerede dielektriske strukturer viser sig at være næsten perfekt for et begrænset antal diskrete indfaldsvinkler i et begrænset frekvensområde. Materialestrukturen forsinker bølger i regioner med højere permittivitet end baggrundsmaterialet således at når de efterfølgende forlader strukturen, er de i fase med bølgerne udenfor. Retningsbestemte akustiske materialestrukturer, der kan skjule et objekt for en akustisk bølge, kan også konstrueres ved hjælp af topologioptimeringsmetoden. Designet udgøres af aluminiumscyindre hvor deres placering og størrelse er optimeret således at deres samlede spredningsmønster annullerer spredningen fra en stor cylinder. Hvis kun tilbagespredningen af et cylindrisk objekt i et begrænset vinkelinterval ønskes elimineret opnås en overraskende simpel ringformet Bragg-lignende gitterstruktur med lag, hvis dimensioner afhænger af objektets radius.

Den anden klasse omhandler optimering af overflader til effektiv ind- og udkobling af elektromagnetiske overfladeplasmoner på metalliske medier. Resultaterne indikerer, at effektiviteter, der overstiger 68%, er mulige for gitre med skrå fordybninger.

Den tredje klasse omhandler design af plane Fresnel zoneplader med henblik på fokusering af elektromagnetiske bølger. De topologioptimerede zoneplader forbedrer fokuseringen i forhold til de resultater, der er kendt fra litteraturen.

Abstract

Sound and light propagate as waves and are scattered, reflected and change direction when encountering other media and obstacles. By optimizing the spatial placement and distribution of the media, which the waves encounter, one can obtain useful and interesting effects. This thesis describes how topology optimization can be used to design structures for manipulation of the electromagnetic and acoustic waves. The wave problems considered here fall within three classes.

The first class concerns the design of cloaks, which when wrapped around an object will render the object undetectable for an outside observer. In the study the material layout of cloaks are restricted to isotropic materials readily available in nature. For fully enclosed, all-dielectric cloaks the cloaking is shown to be nearly perfect for a few discrete angles of incidences in a limited frequency range. The working principle for the cloak is to delay the waves in regions of higher permittivity than the background and subsequently phase match them to the waves outside. Directional acoustic cloaks can also be designed using the topology optimization method. Aluminum cylinders constitutes the design and their placement and size is optimized such that their combined scattering pattern cancel the scattering from a big cylinder. If only the backscattering in a limited angular range needs to be eliminated the electromagnetic cloak design simplifies to surprisingly simple annular Bragg-like grating structures with layer dimensions that depend on the obstacle radius.

The second class concerns the optimization of grating couplers for efficient in- and out-coupling of electromagnetic surface waves at a metal-dielectric interface. Results indicate that efficiencies beyond 68% are possible for slanted groove-based gratings.

The third class concerns the design of planar Fresnel zone plate lenses for focusing electromagnetic waves. The topology optimized zone plates improve the focusing performance compared to results known from the literature.

Publications

The following publications are part of the thesis

- [P1] J. Andkjær and O. Sigmund, "Topology optimized low-contrast all-dielectric optical cloak", *Applied Physics Letters*, Vol. 98, 021112, 2011.
- [P2] J. Andkjær, N. A. Mortensen and O. Sigmund, "Towards all-dielectric, polarization-independent optical cloaks", *Applied Physics Letters*, Vol. 100, 101106, 2012.
- [P3] J. Andkjær and O. Sigmund, "Topology optimized acoustic and all-dielectric optical cloaks", proceedings of Metamaterials '2011: The Fifth International Congress on Advanced Electromagnetic Materials in Microwave and Optics, Barcelona, Spain, October 10-13, 2011.
- [P4] J. Andkjær and O. Sigmund, "Annular Bragg gratings as minimum backscattering cloaks", submitted, 2011.
- [P5] J. Andkjær, S. Nishiwaki, T. Nomura and O. Sigmund, "Topology optimization of grating couplers for the efficient excitation of surface plasmons", *Journal of the Optical Society of America B*, Vol. 317, pp. 1828-1832, 2010.
- [P6] J. Andkjær, S. Nishiwaki, T. Nomura and O. Sigmund, "Topology optimized Fresnel zone plate lenses", to be submitted.

Contents

Preface	i
Resumé (in Danish)	ii
Abstract	iii
Publications	iv
Contents	v
1 Introduction	1
1.1 Motivation and goal	1
1.2 Structure of the thesis	1
2 Time-harmonic acoustic and electromagnetic wave propagation	3
2.1 Acoustic and electromagnetic waves	3
2.2 Electromagnetic vector wave equations	3
2.3 Helmholtz' equation	5
2.3.1 Energy and power flow of a wave	6
2.4 Solution of Helmholtz' equation	7
2.4.1 Scattered field formulation	7
2.4.2 Implementation	8
3 Topology optimization of wave problems	9
3.1 Topology optimization of acoustic and electromagnetic wave propagation problems	9
3.2 Design parametrization	10
3.2.1 Density method	11
3.2.2 Material mask overlay strategy	12
3.3 Formulating the optimization problem	12
3.4 Filtering	14
3.5 Sensitivity analysis	15
3.5.1 Sensitivity-corrections for filters	16
3.5.2 Sensitivities for the MMOS parametrization	16
3.6 Optimization algorithm	17

4	Topology optimized electromagnetic and acoustic cloaks	19
4.1	Transformations Optics	19
4.1.1	Metamaterials	21
4.1.2	All-dielectric cloaking	21
4.2	Method	22
4.3	Topology optimized all-dielectric cloaks[P1]	23
4.4	Effect of polarization and background material[P2]	25
4.5	Topology optimized acoustic cloaks [P3]	28
5	Backscattering cloak	33
5.1	Topology optimized backscattering designs	33
5.2	Analytic solution of the Helmholtz' equation	34
5.3	Method	35
5.4	Results	36
6	Efficiently coupling into the surface plasmon mode	39
6.1	Surface plasmon polaritons	39
6.2	Method	41
6.3	Results	42
7	Fresnel zone plate lens	45
7.1	Fresnel zone plate lenses	45
7.2	Method	47
7.3	Results	48
8	Concluding remarks	51
8.1	Future work	52
	References	53

Chapter 1

Introduction

1.1 Motivation and goal

With the rapid advancement in the areas of material science, nano-photonics, acoustics and scientific computing, many interesting new optical and acoustic devices have emerged in the recent years. The majority of these devices work by manipulating wave propagation inside the device in order to enhance certain desirable physical properties. The wave manipulation characteristics are a result of the spatial placement and distribution of materials in the device. Hence control of the material distribution inside the device enables manipulation of wave propagation for various purposes.

The aim of this thesis is to study wave manipulation of acoustic and electromagnetic waves by topology optimization. Topology optimization is a gradient based optimization method that work by means of varying the distribution of materials within a bounded design domain. The wave manipulation problems studied here falls within three different class of problems. The first problem concerns minimization of the scattered field in all directions or a specified angular range leading to cloak designs for electromagnetic or acoustic waves. Optimization of grating couplers for efficient in and out-coupling of electromagnetic surface waves propagating at a metal-dielectric interface is considered in the second class of problems. Finally planar Fresnel zone plate lenses are optimized for energy focusing. The physics for the problems treated in this thesis are all governed by the same second order scalar differential equation. The boundary value problems are either solved by the finite element method or by analytic means.

1.2 Structure of the thesis

This thesis is a summary of the work done during the Ph.D. study. It gives an overview of the main results presented in the six publications [P1]-[P6].

Chapter 2 presents a general introduction to acoustic and electromagnetic waves. It is shown how the two types of waves are governed by the same scalar second order differential equation in the special case of in-plane electromagnetic wave propagation.

The topology optimization method is introduced in chapter 3. Two different design parametrizations in the realm of topology optimization are employed in this thesis. Furthermore, the topology optimization algorithm, objective functions and corresponding sensitivity analysis are described.

Chapter 4 is dedicated to the design of electromagnetic and acoustic cloaks by topology optimization. The aim of this study is to examine how efficiently objects can be cloaked when using conventional simple isotropic dielectric media readily available in nature. For electromagnetic cloaks the permittivity is varied using the standard density approach in order to minimize the scattered field in the surroundings of the cloak. The initial study concerns the evolution of the optimized designs along with the corresponding cloaking properties for increasing number of incident angles, i.e. increased symmetry. In the second cloaking problem the effect of background material and polarization is studied. For the acoustic cloaks the position and size of subwavelength aluminum cylinders are varied in order to minimize the scattered pressure wave. To aid realization the final design is constrained to consist of cylinders with radii that fall within 3 discrete values. The chapter is a summary of publications [P1], [P2] and [P3].

In chapter 5 the full cloaking problem is relaxed by only requiring elimination of backscattering in a limited angular range. As it turns out, this relaxation results in omnidirectional cloak design made of isotropic, low-contrast, all-dielectric materials readily available in nature. Due to the simple omnidirectional ring design the electromagnetic field can be computed analytically. A parametrization based on topology optimized designs is used in the optimization approach based on the analytic expression. Presented method and results are based on findings from [P4].

The wave manipulation problem studied in chapter 6 deals with the efficient excitation of surface plasmon polaritons propagating along a dielectric-metal interface. Standard density based topology optimization is employed to find topologies for grating couplers, such that the in and out-coupling efficiency of the plasmonic surface waves are maximized. The chapter is a summary of publication [P5].

The final design problem of this thesis is presented in chapter 7 and concerns focusing of a propagating wave by half opaque Fresnel zone plate. The transition boundary condition can model full transmission or opacity at a specified design boundary depending on the surface impedance. This property can be exploited in the standard density approach allowing the surface impedance in each boundary element to be varied. Method and results are based on findings from [P6].

Finally the thesis is concluded in chapter 8 and ideas for future work are presented.

Chapter 2

Time-harmonic acoustic and electromagnetic wave propagation

In this chapter acoustic and electromagnetic waves are introduced. It is shown how the physics of time-harmonic acoustic waves and time-harmonic electromagnetic waves are governed by second order differential equations. The governing differential equations with appropriate boundary conditions form boundary value problems, which for the majority of the problems covered by this thesis are solved by the finite element method.

2.1 Acoustic and electromagnetic waves

Acoustic waves are a special form of elastic waves propagating in inviscid fluids with zero shear modulus[1]. The inviscid fluid particles oscillate back and forth about their equilibrium positions creating regions of high density (compression) and low density (decompression). This motion effectively creates a traveling longitudinal pressure wave with oscillations parallel to the direction of propagation. Just as for mechanical waves, it is the disturbance that travels not the individual particles in the medium. Because acoustic waves work by means of compressing matter it can only propagate in a medium and not in vacuum.

In contrast to acoustic waves, electromagnetic waves are transverse in character. The electric and magnetic fields oscillate perpendicular to each other and to the propagation direction[2]. Electromagnetic waves also differ from acoustic waves in the sense that they can propagate in vacuum as well as in a medium. Electromagnetic waves are caused by the interaction of a time-varying electric field and a time varying magnetic field.

In the following detailed description of wave propagation we will focus our attention on electromagnetic waves because manipulation of acoustic waves constitutes only a minor part of this thesis. However we will in our derivations end up with the well-known duality between acoustic and in-plane electromagnetic wave propagation in two dimensions (e.g. [3]). That is, the two different wave phenomena are governed by the same scalar wave equation.

2.2 Electromagnetic vector wave equations

Electromagnetic wave propagation is governed by Maxwells equations[4]. The magnetic and electric field are coupled through Maxwell-Ampere's and Faraday's laws, which in source-free regions with isotropic, linear and inhomogeneous material can

be stated in the instantaneous differential form as

$$\nabla \times \mathbf{H} = \sigma \mathbf{E} + \epsilon \frac{\partial \mathbf{E}}{\partial t} \quad (2.1)$$

$$\nabla \times \mathbf{E} = -\mu \frac{\partial \mathbf{H}}{\partial t} \quad (2.2)$$

where $\mathbf{H} = \mathbf{H}(\mathbf{r}, t)$ and $\mathbf{E} = \mathbf{E}(\mathbf{r}, t)$ is the magnetic and electric field, respectively, $\mathbf{r} = (x, y, z)$ is the (Cartesian) position vector and t is the time. The three constitutive parameters, the permittivity $\epsilon = \epsilon(\mathbf{r})$, the permeability $\mu = \mu(\mathbf{r})$ and the conductivity $\sigma = \sigma(\mathbf{r})$ determines how an applied electromagnetic wave behaves in a medium. Control of these material properties allows us to manipulate wave propagation which we will return to in the next chapter.

The two coupled first order differential equations can by trivial manipulations be decoupled at the expense of increasing the order of differential equations to second order. For both the electric and magnetic field we thereby get a system of three time dependent second order differential equations, which for the electric field are given by

$$\nabla \times \left(\mu_r^{-1} \nabla \times \mathbf{E} \right) + \frac{\epsilon_r}{c^2} \frac{\partial^2 \mathbf{E}}{\partial t^2} + \mu_0 \sigma \frac{\partial \mathbf{E}}{\partial t} = \mathbf{0} \quad (2.3)$$

where $c = 1/\sqrt{\mu_0 \epsilon_0}$ is the speed of light in vacuum, $\epsilon_0 \approx 8.8542 \cdot 10^{-12}$ F/m is the free space permittivity and $\mu_0 = 4\pi \cdot 10^{-7}$ H/m is the free space permeability. The two remaining constants $\epsilon_r = \epsilon/\epsilon_0$ and $\mu_r = \mu/\mu_0$ are the relative material properties to that of vacuum.

For time-harmonic problems the electric field can be written in the form $\mathbf{E}(\mathbf{r}, t) = \hat{\mathbf{E}}(\mathbf{r}) \cos(\omega t + \phi)$ where ω and ϕ is the frequency and phase of the wave, respectively. Expressing the time-dependence using an exponential function enables us to construct the complex phasor $\tilde{\mathbf{E}}(\mathbf{r})$, which contains both amplitude and phase information of the field as well as being time-independent.

$$\mathbf{E}(\mathbf{r}, t) = \hat{\mathbf{E}}(\mathbf{r}) \cos(\omega t + \phi) = \text{Re} \left[\hat{\mathbf{E}}(\mathbf{r}) e^{j\phi} e^{j\omega t} \right] = \text{Re} \left[\tilde{\mathbf{E}}(\mathbf{r}) e^{j\omega t} \right] \quad (2.4)$$

where $\text{Re}[\cdot]$ denotes the real part. Furthermore, the time derivative $\partial/\partial t$ corresponds to a multiplication by $j\omega$ in the above phasor notation. In the remainder of this thesis we only use the phasor notation, not only for the electric field but also for the magnetic as well as the acoustic field, hence we omit the "tilde". Using this phasor notation for time-harmonic waves we convert the wave equation from time domain to frequency domain and get three frequency dependent second order differential equations

$$\nabla \times \left(\mu_r^{-1} \nabla \times \mathbf{E} \right) - k_0^2 \epsilon_c \mathbf{E} = \mathbf{0} \quad (2.5)$$

where $k_0 = \omega/c$ is the free space wavenumber and the complex permittivity is given as $\epsilon_c = \epsilon_r - j\sigma/(\omega\epsilon_0)$. The imaginary part of the permittivity represents the losses[5]. It is important to remember that the solution to equation (2.5) is a phasor and not

Wave-type	u	A	B	k_0
E-polarized	E_z	μ_r^{-1}	ϵ_r	$\omega\sqrt{\mu_0\epsilon_0}$
H-polarized	H_z	ϵ_r^{-1}	μ_r	$\omega\sqrt{\mu_0\epsilon_0}$
Acoustic	p	ρ_r^{-1}	κ_r^{-1}	$\omega\sqrt{\rho_0\kappa_0^{-1}}$

Table 2.1 Parameter relations for general notation.

a physical field. The physical field at time $t = 0$ is easily obtained as the real part of the complex phasor. Multiplying an obtained phasor solution with $e^{j\phi_1}$ results in the phasor field for the phase, ϕ_1 .

2.3 Helmholtz' equation

Throughout the thesis we will assume wave propagation in structures with infinite extension in one dimension. In-plane modes describe wave propagation in a plane perpendicular to the infinite extension. Traditionally in a Cartesian coordinate system in-plane modes are given in the (x, y) -plane with the z -axis being out-of-plane. With the $\mathbf{E} = (0, 0, E_z)^T$ field being out-of-plane and $\mathbf{H} = (H_x, H_y, 0)^T$ field being in-plane the wave equation in (2.5) simplifies to the scalar Helmholtz' equation (here presented in a general form)

$$\nabla \cdot (A\nabla u) + k_0^2 Bu = 0 \quad (2.6)$$

where $u = E_z$, $A = \mu_r^{-1}$ and $B = \epsilon_c$ for the E_z polarization. In case of the magnetic field being out-of-plane we instead use $u = H_z$, $A = \epsilon_c^{-1}$ and $B = \mu_r$ for the H_z polarization. The big advantage is of course that the out-of plane scalar field only needs to be computed in the (2D) plane thereby easing the computational efforts. Having obtained the solution for the out-of-plane field the in-plane field can easily be derived from Maxwell-Amperes or Faradays laws in equations (2.1) and (2.2), respectively.

The scalar Helmholtz' equation does not only govern the in-plane wave propagation for an electromagnetic wave. It also covers acoustic wave propagation[6] as well as certain types of elastic wave propagation[7], with appropriate choice of the coefficients A and B , c.f. table 2.1. In case of acoustic wave propagation u describes the pressure field, p , with A being the inverse of the mass density, ρ_r , and B being the inverse of the bulk modulus, κ_r . Here we have related the acoustic material properties to that of air at room temperature to cast the acoustic wave propagation in the same form as the electromagnetic case. Thus $k_0 = \omega/c$ is the wave number in air with $c = 1/\sqrt{\rho_0\kappa_0^{-1}}$ being the speed of sound in air, where $\rho_0 = 1.204 \text{ kg m}^{-3}$ and $\kappa_0 = 1.42 \cdot 10^5 \text{ Pa}$.

Appropriate boundary conditions along with the stated Helmholtz equation complete the boundary value problem which governs the physics for the problems considered in this thesis. In order to solve the boundary value problem numerically

we need to truncate the otherwise infinite wave problems into a finite domain[8]. However, reflections from the boundaries are very likely without proper choice of the truncation boundary conditions. First order absorbing boundaries are used for the cloaking studies, whereas perfectly matched layers (PMLs) backed up with first order absorbing boundaries are employed for problems regarding surface plasmons and Fresnel zone plate lenses. The first order absorbing boundary conditions only exhibit good performances under tailored circumstances (specific frequency and angle of incidence) thus limiting their use. In contrast, PML works for arbitrary angles of incidence and frequencies provided the PMLs are sufficiently large. The idea of the PMLs is to surround the computational domain with a region of reflectionless artificial absorbing material. When a wave enters the absorbing region, it is attenuated and decays exponentially. The fictive loss of energy is governed by the imaginary part of the material parameters in the PMLs (just like a lossy medium). If the loss function is chosen wisely[9], all the energy of the entering waves will be absorbed without reflections.

2.3.1 Energy and power flow of a wave

Energy and power flow of a wave are important factors for different performance measures in the optimization process. Both terms are described in Poynting's theorem[2] which in the instantaneous volume form and in the absence of sources can be written as

$$-\oint_{\partial\Omega} \mathbf{n} \cdot \mathbf{S} \, d\mathbf{r} = \int_{\Omega} \sigma |\mathbf{E}|^2 \, d\mathbf{r} + \frac{\partial}{\partial t} \int_{\Omega} \epsilon |\mathbf{E}|^2 \, d\mathbf{r} + \frac{\partial}{\partial t} \int_{\Omega} \mu |\mathbf{H}|^2 \, d\mathbf{r} \quad (2.7)$$

where $\mathbf{S} = (\mathbf{E} \times \mathbf{H})$ is the Poynting vector representing the directional energy flux. The equation states the conservation of energy for electromagnetic fields in a volume Ω where the power flowing into the domain equals the sum of the power dissipation and the rate of change in stored electric and magnetic energy. The theorem simplifies for time-harmonic waves governed by the scalar Helmholtz equation. In the coming chapters we will make extensive use of both the time-averaged energy and time-averaged power flow. The time-averaged energy U in a domain Ω are in general notation given as

$$U = \frac{1}{4} \int_{\Omega} B |u|^2 \, d\mathbf{r} \quad (2.8)$$

whereas the time-averaged power flow P through a boundary Γ in the direction $\mathbf{n} = \{n_x, n_y\}^T$ is

$$P = \int_{\Gamma} \mathbf{n} \cdot \frac{1}{2\omega} \text{Re} [jA\bar{u}\nabla u] \, d\mathbf{r} \quad (2.9)$$

where $(\bar{\cdot})$ denotes the complex conjugate and A , B and u are given in table 2.1.

2.4 Solution of Helmholtz' equation

Helmholtz' equation with appropriate boundary conditions form a boundary value problem, for which it is not possible in most cases to find an analytic expression for the state field. However, in this thesis we will encounter one problem (further details in chapter 5) where the geometry of homogeneous material is so simple that it allows us to compute the field analytically. For more complex geometries the boundary value problem must be relaxed in order to find an approximate solution with a numerical technique. In this work we use the finite element method[8]. There exist other numerical schemes that are used for electromagnetic problems such as the finite difference method[10] or discontinuous Galerkin methods[11], but these are normally used in the time domain.

In the finite element method the outlined boundary value problem for the physical system is relaxed into an equivalent integral form called the weak formulation. Next we subdivide the domain of the problem into elements and choose an interpolation function that gives an approximation of the unknown state field within an element. On the element level the nodal values are interpolated as

$$u(\mathbf{r}) \approx \sum_e^M u_e(\mathbf{r}) = \sum_e^M \mathbf{N}_e(\mathbf{r}) \mathbf{u}_e \quad (2.10)$$

where M is the number of elements, \mathbf{N}_e is the element shape functions and \mathbf{u}_e is the unknown nodal solutions within the element. Following the standard Galerkin method we assemble the element equations from all elements into a linear system of equations to be solved in order to determine the approximate solution

$$\mathbf{S}\mathbf{u} = \mathbf{f} \quad (2.11)$$

where \mathbf{S} is the system matrix, \mathbf{u} is a vector of the discretized nodal values of the state field u and \mathbf{f} is the load vector. The system matrix, \mathbf{S} , is dependent on the element wise constant material properties A and B , c.f. table 2.1.

2.4.1 Scattered field formulation

One should keep in mind that an error in the phase of the simulated propagating incident wave will occur[12], when solving the scalar Helmholtz equation as stated in equation 2.6 using the finite element method. The basis functions cannot represent the true solution exactly. This error is named dispersion error and it can grow substantially over a number of wavelengths. Using higher order elements, changing the formulation and/or using boundary integral equations for tighter mesh truncation can remedy the problem of solution accuracy. In this work we change the presented total field formulation to the scattered field formulation. That is, the unknown (total) field, u , can be written as the sum of the known incident field, u^i , and the unknown generated scattered field, u^s . This gives us the freedom to

insert $u = u^i + u^s$ in the Helmholtz' equation as well as the boundary conditions and change the dependent variable from the total field to the scattered field. Thus equation (2.6) is reformulated into the inhomogeneous Helmholtz' equation

$$\nabla \cdot (A \nabla u^s) + k_0^2 B u^s = -\nabla \cdot (A \nabla u^i) - k_0^2 B u^i \quad (2.12)$$

The major difference between the two formulations is how the incident wave (the load) enters the boundary value problem. In the total field formulation the incident wave is excited on truncation boundaries whereas in the scattered field formulation the incident wave is excited in regions where a scattering material is present and on conducting boundaries. The dispersion errors are thereby eliminated because the incident field does not have to propagate numerically across the computational domain between the truncation surface and the scattering object.

2.4.2 Implementation

The implementation of the wave propagating problems is based on the high-level programming language COMSOL Multiphysics with Matlab[13, 14]. COMSOL Multiphysics is an engineering, design, and finite element analysis software package for the modeling and simulation of various physics-based problems described by partial differential equations. The program allow the user to state the boundary value problem in weak as well as strong form or utilize the predefined templates (application modes) for specific physical problems with appropriate boundary conditions. For the problems regarding cloaking or surface plasmon polaritons we state the boundary value problems in strong form, whereas we use the RF application module for in-plane waves when designing Fresnel zone plate lenses. The state field is given by second order Lagrange elements with at least 6 elements per wavelength. Accuracy of the various finite element implementations have been verified with analytic solutions when possible and by Poynting's theorem in equation (2.7) regarding the conservation of energy.

Chapter 3

Topology optimization of wave problems

As briefly mentioned in the previous chapter the spatial placement and distribution of the material properties determines how a wave behaves in a medium. Control of these material properties allows us to manipulate wave propagation for various purposes. The material as well as material layout needed in wave devices like Bragg gratings[15], invisibility cloaks[16] and Fresnel zone plate lenses[17] can be derived directly by analytic means. Such applications were developed by ingenious physicists with great physical insight. However, in some cases the derived material properties are very challenging to realize especially in the optical regime (e.g. invisibility cloaks[16]), and in other cases the geometrical layout rule is known not to be optimal (e.g. Fresnel zone plate lenses[18]). Optimization methods may be used as an efficient design tool for such problems. Topology optimization is a gradient based optimization method that work by varying the distribution of materials within a bounded design domain. The strength of this method is that it can change the shape topology without any geometrical constraints on the design. Originally the method was developed by Kikuchi and Bendsøe using a homogenization technique to minimize the compliance of continuum structures[19]. Since then the method has been extended to other fields of engineering such as heat transfer (e.g. [20]), fluid dynamics (e.g. [21]), micro electro-mechanical systems (e.g. [22, 23]), photonics (e.g. [24, 25]) and acoustics (e.g. [6]). Today implementations[26, 27] of the topology optimization method for structural problems are available free of charge intended for educational purposes and even commercial software packages such as OptiStruct by Altair and TOSCA by FE-Design exist. The purpose of this chapter is to give a brief introduction to topology optimization and how it is applied to the acoustic and electromagnetic wave manipulation problems covered in this thesis. A thorough description of the topology optimization method can be found in the monograph by Bendsøe and Sigmund[28].

3.1 Topology optimization of acoustic and electromagnetic wave propagation problems

The behavior of electromagnetic waves is determined by the distribution of dielectric material, magnetic material, air and/or metal. The first material distribution technique concerning electromagnetic waves was reported more than a decade ago[29, 30]. In the study, dielectric material was distributed in order to maximize the band gap in 2D photonic crystals. Not long after the initial study, the transmission through photonic crystal wave guide bends[24] and splitters[31] was maximized

for single frequency as well as broad banded behavior. Realizations of the optimized dielectric layouts for the photonic crystal wave guide verified the results obtained by topology optimization[25, 32]. Topology optimization has also been applied to antenna design, e.g. patch antennas[33, 34], dielectric resonator antennas[35] and sub-wavelength antennas[36]. However, at microwave the skin-depth is many orders of magnitude smaller than the wavelength which poses a problem of capturing the physics correctly in the framework of the topology optimization method. An efficient skin-depth resolving methodology for distributing conducting material has been developed in [37] to remedy this problem. Material layouts for optimized efficiency of various coupling devices, e.g. [38, 39, 40], for electromagnetic waves has also been reported in the literature. For the majority of the above studies topology optimization has been applied to problems in the frequency domain. However, it is more appropriate to define the problem in the time-domain when designing filter and pulse modulation devices[41, 42, 43, 44]. A comprehensive review of topology optimization applied to nano-optical design can be found in [45].

Topology optimization was applied to acoustic problems for the first time in 2003 where a Horn-like antenna device was optimized[46] and a similar study was later reported in [47]. Topology optimization of vibro-acoustic problems in which the elastic and acoustic governing equations are coupled has also been studied[48]. Furthermore, a thorough study of noise reduction by topology optimized sound barriers was presented in [6]. The latter study also covers 3D acoustic design.

Topology optimization has shown to be an effective tool in determining the material layout for manipulation of acoustic or electromagnetic waves. In this work topology optimization is applied to design wave manipulation devices for field minimization, wave coupling and energy focusing. The first problem concerns minimization of the scattered field in all directions or a specified angular range leading to cloak designs for electromagnetic or acoustic waves. Efficient in and out-coupling of electromagnetic surface waves propagating at a metal-dielectric interface is considered in the second class of problems. Finally, planar Fresnel zone plate lenses are optimized for energy focusing. The different physics for the problems treated in this thesis are all be governed by an equivalent state equation, as already described in the preceding chapter. However, the design parametrization for the different optimization problems vary which will be discussed in further details below.

3.2 Design parametrization

The concept of topology optimization for a wave manipulation problem is sketched in figure 3.1. The material layout in the design domain Ω_{des} is varied continuously in order to optimized a given objective in Ω_{out} . Common objectives for wave manipulation problems are field or power flow minimization/maximization. The design parametrization provide the foundation of how the material layout is varied in the design domain. In this thesis we have employed two different design parametrizations; the standard density approach[49] and the material mask overlay strategy[50, 51].

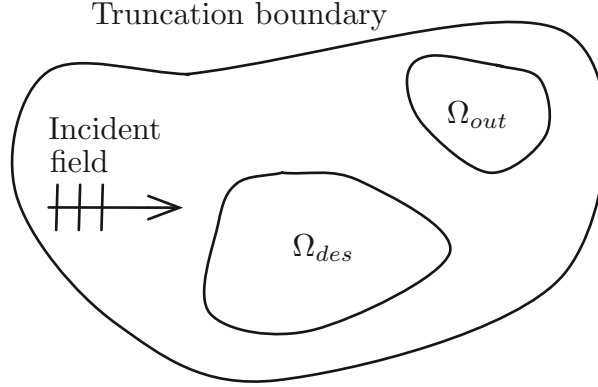


Figure 3.1 The concept of topology optimization for a wave manipulation problem. The material layout in the design domain Ω_{des} is varied continuously in order to optimized a given objective in Ω_{out} .

The former method is used for the majority of the problems, whereas the latter is only employed for cloaking problems, where cylindrical features constitute the design.

3.2.1 Density method

In the density approach a continuous design variable $0 \leq \gamma_e \leq 1$ is introduced for each element in the design domain and controls the material properties in its element. The design variables are relative element material densities, where $\gamma_e = 0$ corresponds to material 1 and $\gamma_e = 1$ corresponds to material 2. The following linear interpolation models the relation between element densities and element material

$$A(\gamma_e) = A_1 + \gamma_e(A_2 - A_1) \quad (3.1)$$

$$B(\gamma_e) = B_1 + \gamma_e(B_2 - B_1) \quad (3.2)$$

where (A_1, B_1) and (A_2, B_2) are the (complex) material properties for material 1 and 2, respectively. The interpolation function allows intermediate values of the material properties in the final design. For some problems this is both physically sound and realizable, but for other problems intermediate densities are difficult to interpret in practical realizations and should be avoided. One path to obtaining discrete designs is to make intermediate densities "expensive" for the optimizer using penalization schemes. A popular choice for mechanical problems is the SIMP-method[49] and for certain electromagnetic problems the "pamping" method[31]. The latter method works by introducing artificial damping and thereby artificial energy loss for intermediate densities by adding an imaginary part to the permittivity $j4(\gamma_e^2 - \gamma_e)$ in the interpolation scheme. The "pamping"-method usually works well when maximizing transmission (e.g. excitation of surface plasmons) but fails to work for field-minimization problems (e.g. cloaking). Heaviside projection based

filtering techniques is another approach for achieving discrete designs and this will be explained in further details below.

3.2.2 Material mask overlay strategy

The Material Mask Overlay Strategy (MMOS) employs a continuous approximation of the Heaviside function to interpret a fixed set of cylinders as element densities in an underlying finite element mesh. The solution to the physical problem and gradients are found based on the element densities as in the standard topology optimization approach. However, the cylinders are parametrized by their positions and radii and these parameters are used as design variables in the optimization process.

Positions and radii of M cylinders are initialized as the first step in MMOS. Based on the cylinder layout the element density γ_e for element e can be derived as

$$\gamma_e = \prod_{i=1}^M \frac{1}{1 + \exp[-\beta(d_{ei} - r_i)]} \quad (3.3)$$

where d_{ei} is the distance from element e to the center of cylinder i and r_i is the radius of cylinder i . A high β -value is chosen for a close approximation of the Heaviside function. If the centroid of element e lies within the space occupied by one of the M cylinders, γ_e will go towards zero, due to the denominator in equation 3.3 going to infinity, otherwise γ_e will be one.

It should be remarked that there exists an alternative method[52] for achieving cylinder features in the final design using a β -continuation scheme. The method relies heavily on penalizing intermediate densities in order to achieve the fixed feature shape. However, it is not clear how intermediate densities can be penalized effectively in cloaking problems and for this reason the method is not used here.

3.3 Formulating the optimization problem

A generic formulation of the topology optimization problem for either of the two design parametrizations takes the form

$$\min_{\mathbf{x}} \quad \Phi(\mathbf{u}(\mathbf{x}), \mathbf{x}) \quad \text{objective function} \quad (3.4)$$

$$\text{subjected to} \quad g_i(\mathbf{u}(\mathbf{x}), \mathbf{x}) \leq 0, \quad i = 1, \dots, m \quad \text{constraint functions} \quad (3.5)$$

$$\mathbf{S}(\mathbf{x})\mathbf{u} - \mathbf{f}(\mathbf{x}) = 0 \quad \text{state problem} \quad (3.6)$$

$$x_j^{\min} \leq x_j \leq x_j^{\max}, \quad j = 1, \dots, n \quad \text{design variable bounds} \quad (3.7)$$

where \mathbf{x} is a vector of design variables. For the standard density method \mathbf{x} defines the element densities which can be varied continuously between 0 and 1, whereas for MMOS \mathbf{x} represents positions and radii for all cylinders.

The objective function Φ measures the performance of the design given by the design variables. As briefly mentioned in the previous chapter we have overall used two performance measures in this work, energy or power flow of a wave. The former objective function does not distinguish between standing or traveling waves whereas the latter objective only measures traveling waves in a specified direction. The energy of a wave can be evaluated as given in equation (2.8). However, in all problems treated here the material property B is constant in the domain where the objective function is evaluated. Thus in effect the material property B together with $1/4$ only act as a scaling factor for the objective and for this reason are omitted. Instead of the energy we minimize/maximize the field norm $|u|^2$. The power flow of a wave can be calculated as stated in equation (2.9), however, we evaluate the power flow in a domain instead of at a boundary. It should be noted that in the MMOS design parametrization there is no inherited protection against two cylinders merging together. We are only interested in designs with isolated cylinders therefore we add an additional distance measure between all cylinders to the objective function. The distance measure is included in the objective function to penalize overlapping cylinders explicitly. If the boundaries of two cylinders are close to overlapping the penalization term will increase exponentially and otherwise go towards zero. Cylinders in close proximity thereby repel each other leading to isolated shapes. Furthermore a volume constraint is introduced for all topology optimization problems to avoid excess usage of material and in some cases such a constraint has been observed to speed up convergence.

For some optimization problems it is desirable to optimize the material distribution for two or more responses (e.g. frequencies) simultaneously. This is effectively performed by a min/max-formulation, i.e. the response that gives the highest objective is minimized, stated in generic form

$$\min_{\mathbf{x}} \max_{k=1,\dots,N} \{\Phi_k(\mathbf{u}_k(\mathbf{x}), \mathbf{x})\} \quad (3.8)$$

where k refers to the index of the N responses. However the min/max-formulation leads to a non-smooth optimization problem that cannot be solved using a gradient-based optimizer. In stead an extra design variable ξ and an extra constraint for each response are introduced in the equivalent smooth formulation

$$\min_{\mathbf{x}, \xi} \xi \quad (3.9)$$

$$\text{subjected to } \Phi_k(\mathbf{u}_k(\mathbf{x}), \mathbf{x}) - \xi \leq 0, \quad k = 1, \dots, N \quad (3.10)$$

The non-linear and non-convex optimization problem either in a standard or min/max-formulation is solved efficiently by the gradient-based optimization routine Method of Moving Asymptotes (MMA) [53] in an iterative approach. The overall optimization algorithm is described in a simplified pseudo code at the end of this chapter.

3.4 Filtering

Filtering techniques are adopted in the density approach to mitigate mesh-dependency and to introduce a minimum length scale in order to avoid small details. Here we briefly describe the standard density filter[54, 55] and the deterministic robust formulation[56], both of which have been used in this thesis. A thorough overview of various filters employed in topology optimization is provided in [57]. Recent types of filters include the PDE filter[58, 59] introduced for parallel implementations of topology optimization and stochastic robust formulations[60, 43].

The standard density filter modifies the element density to be a function of the densities in a specified neighborhood of an element. The neighborhood N_e of each element e is defined as the elements that lie within the filter radius R

$$N_e = \{j \mid \|\mathbf{r}_e - \mathbf{r}_j\| < R\} \quad (3.11)$$

The filtered variable $\tilde{\gamma}_e$ for element e is then calculated as

$$\tilde{\gamma}_e = \frac{\sum_{j \in N_e} w(\mathbf{r}_j) V_j \gamma_j}{\sum_{j \in N_e} w(\mathbf{r}_j) V_j} \quad (3.12)$$

where $w(\mathbf{r}_j) = R - \|\mathbf{r}_e - \mathbf{r}_j\|$ is the linearly decaying weight function and V_j is the volume of element j . The standard density filter does not prevent grayscale (i.e. intermediate densities). Even with penalization schemes grayscale are introduced in a transition region between the different materials. The standard density filter acts as a base upon which other filters are build (e.g. projection filters).

Several filters based on Heaviside projections[61] have been proposed in the literature in order to achieve discrete designs and minimum length scales on one or all materials. In the study of surface plasmon we use a multiphase projection filter[62], which ensure minimum length scales on both material 1 and 2 simultaneously. Whereas for the cloaking problems and Fresnel zone plate lenses we use the deterministic robust formulation[56], which makes the design robust for equally distributed manufacturing errors as well as giving discrete designs for problems where penalization fails to work. The backbone of the deterministic robust formulation is threshold projection[63], which project the filtered densities below the threshold $\eta \in [0, 1]$ towards 0, and above the threshold towards 1. Three equivalent state problems[56], but with different projections (i.e. dilated, intermediate and eroded) are formulated and optimized as a min/max problem. The threshold projection from [63] is given as

$$\tilde{\tilde{\gamma}}_e = \begin{cases} \eta [e^{-\beta(1-\tilde{\gamma}_e/\eta)} - (1 - \tilde{\gamma}_e/\eta)e^{-\beta}] & 0 \leq \tilde{\gamma}_e \leq \eta \\ (1 - \eta) [1 - e^{-\beta(1-\tilde{\gamma}_e/\eta)/(1-\eta)} + (\tilde{\gamma}_e - \eta)/(1 - \eta)e^{-\beta}] + \eta & \eta < \tilde{\gamma}_e \leq 1 \end{cases} \quad (3.13)$$

where β is the projection parameter, which controls how well the Heaviside function is approximated. For $\beta \rightarrow \infty$ equation (3.13) approaches the Heaviside function with threshold η .

3.5 Sensitivity analysis

The design is updated based on the sensitivities of the objective and constraints with respect to the physical element densities. The sensitivities indicate how much the objective and constraints will change for an infinitesimal variation in a certain design variable. Here the adjoint method[31] is employed to find the sensitivities for a discretized problem on the form of equation (2.11). Following the adjoint analysis we add the scalar product of the residual $\mathbf{R} = \mathbf{S}\mathbf{u} - \mathbf{f} = \mathbf{0}$ and a vector of Lagrangian multipliers to the objective function. Due to the complex problem both the residual and its complex transpose are added to form the augmented Lagrangian

$$\mathcal{L} = \Phi + \boldsymbol{\lambda}_1^T (\mathbf{S}\mathbf{u} - \mathbf{f}) + \boldsymbol{\lambda}_2^T (\bar{\mathbf{S}}\bar{\mathbf{u}} - \bar{\mathbf{f}}) \quad (3.14)$$

where $(\cdot)^T$ refers to the real transpose and $\boldsymbol{\lambda}_1$ and $\boldsymbol{\lambda}_2$ are Lagrangian multipliers. Next the derivative of the Lagrangian with respect to γ^e needs to be derived. The input to the objective function $\Phi(\mathbf{u}_R(\gamma), \mathbf{u}_I(\gamma), \gamma)$ is formulated in terms of real and imaginary parts of the complex field vector $\mathbf{u} = \mathbf{u}_R - j\mathbf{u}_I$. Furthermore, the complex field vector is an implicit function of the design variables, thus the chain-rule is needed in the evaluation of $d\mathcal{L}/d\gamma^e$. The further derivations is omitted here, however the idea is to eliminate the unknown derivatives $\partial\mathbf{u}_R/\partial\gamma^e$ and $\partial\mathbf{u}_I/\partial\gamma^e$ at the cost of solving an adjoint problem. By clever manipulations it can be shown that $\boldsymbol{\lambda}_1 = \bar{\boldsymbol{\lambda}}_2 = \boldsymbol{\lambda}$ and finally the sensitivities are derived to

$$\frac{d\mathcal{L}}{d\gamma^e} = \frac{d\Phi}{d\gamma^e} = \frac{\partial\Phi}{\partial\gamma^e} + 2\text{Re} \left[\boldsymbol{\lambda}^T \left(\frac{\partial\mathbf{S}}{\partial\gamma^e} \mathbf{u} - \frac{\partial\mathbf{f}}{\partial\gamma^e} \right) \right] \quad (3.15)$$

where $\boldsymbol{\lambda}$ is obtained from the solution of the adjoint problem

$$\mathbf{S}^T \boldsymbol{\lambda} = -\frac{1}{2} \left(\frac{\partial\Phi}{\partial\mathbf{u}_R} - j \frac{\partial\Phi}{\partial\mathbf{u}_I} \right)^T \quad (3.16)$$

The term $\partial\Phi/\partial\gamma^e$ in equation (3.15) is for the specific problems treated in this thesis zero due to the design domain not being a part of the output domain in any of the problems. The terms $\partial\mathbf{S}/\partial\gamma^e$ and $\partial\mathbf{f}/\partial\gamma^e$ are known as part of the direct solution of equation (2.11). For the present finite element problem the system matrix, \mathbf{S} , is symmetric and hence the solution of the adjoint problem in equation (3.16) can be performed very efficiently by reuse of the factorization of \mathbf{S} computed for the direct analysis stated in equation (2.11). To summarize, this means that the computational costs associated with obtaining the sensitivities is ignorable compared to the solution of the original problem in equation (2.11). In order to compute the sensitivities for the objective function Φ only the right-hand side of equation (3.16) needs to be derived. Omitting B and $1/4$ in equation (2.8), the right-hand side of equation (3.16) with the field norm being the objective can be derived to

$$\frac{1}{2} \left(\frac{\partial\Phi}{\partial\mathbf{u}_R} - j \frac{\partial\Phi}{\partial\mathbf{u}_I} \right) = \int_{\Omega_{out}} \bar{\mathbf{u}} \, d\mathbf{r} \quad (3.17)$$

In case the objective function is stated as the power flow given by equation (2.9) the right-hand side of equation (3.16) is found by the chain rule to

$$\frac{1}{2} \left(\frac{\partial \Phi}{\partial \mathbf{u}_R} - j \frac{\partial \Phi}{\partial \mathbf{u}_I} \right) = \int_{\Omega_{out}} \left(\frac{\partial p}{\partial \mathbf{u}} + \frac{\partial p}{\partial \nabla \mathbf{u}} \cdot \nabla \right) d\mathbf{r} \quad (3.18)$$

where $p = 1/(2\omega) \text{Re}[jA\bar{\mathbf{u}}\nabla\mathbf{u}] \cdot \mathbf{n}$ and hence

$$\frac{\partial p}{\partial \mathbf{u}} = -\frac{1}{4\omega} jA\bar{\nabla}\bar{\mathbf{u}} \cdot \mathbf{n} \quad (3.19)$$

$$\frac{\partial p}{\partial \nabla \mathbf{u}} = \frac{1}{4\omega} jA\bar{\mathbf{u}}\mathbf{n} \quad (3.20)$$

3.5.1 Sensitivity-corrections for filters

The gradients obtained by the adjoint sensitivity analysis given in equation (3.15) are based on the physical element densities. With a filter applied to the problem we find the gradients of the objective function with respect to the design variables from the chain rule. Thus for the standard density filter we get

$$\frac{\partial \Phi}{\partial \gamma_e} = \sum_{i=N_e} \frac{\partial \Phi}{\partial \tilde{\gamma}_i} \frac{\partial \tilde{\gamma}_i}{\partial \gamma_e} \quad (3.21)$$

and for filter types based on Heaviside projection the sensitivities are found by

$$\frac{\partial \Phi}{\partial \gamma_e} = \sum_{i=N_e} \frac{\partial \Phi}{\partial \tilde{\gamma}_i} \frac{\partial \tilde{\gamma}_i}{\partial \gamma_e} \quad (3.22)$$

3.5.2 Sensitivities for the MMOS parametrization

The gradients for the objective with respect to position and radius are derived using the chain rule

$$\frac{\partial \Phi}{\partial \zeta_i} = \sum_{e=1}^N \left(\frac{\partial \Phi}{\partial \gamma_e} \frac{\partial \gamma_e}{\partial \zeta_i} \right) \quad (3.23)$$

where ζ_i represent one of the three design variables (x_i, y_i, r_i) for cylinder i and N is the number of elements in the design domain. The sensitivities $\partial \Phi / \partial \gamma_e$ can be obtained from equation (3.15) and the sensitivities $\partial \gamma_e / \partial \zeta_i$ for the element density of element e with respect to a change in the position (x_i, y_i) or radius r_i for cylinder i are derived from equation (3.3)

$$\frac{\partial \gamma_e}{\partial x_i} = \gamma_e \left(\frac{\beta \exp(-\beta(d_{ei} - r_i))}{1 + \exp[-\beta(d_{ei} - r_i)]} \right) \left(\frac{x_i - x_e}{d_{ei} + \epsilon} \right) \quad (3.24)$$

$$\frac{\partial \gamma_e}{\partial y_i} = \gamma_e \left(\frac{\beta \exp(-\beta(d_{ei} - r_i))}{1 + \exp[-\beta(d_{ei} - r_i)]} \right) \left(\frac{y_i - y_e}{d_{ei} + \epsilon} \right) \quad (3.25)$$

$$\frac{\partial \gamma_e}{\partial r_i} = -\gamma_e \left(\frac{\beta \exp(-\beta(d_{ei} - r_i))}{1 + \exp[-\beta(d_{ei} - r_i)]} \right) \quad (3.26)$$

where ϵ is a small number added to avoid a singularity in the denominator if the positions of element e and cylinder j are coincident.

3.6 Optimization algorithm

The overall optimization algorithm is described in a simplified pseudo code below where the numbers in parentheses correspond to equation numbers above.

1. Build neighborhood (3.11) if filtering
2. Initialize the design variable vector \mathbf{x}^1 , $k = 0$ and change = 1
3. while change ≥ 0.01 and $k \leq 1000$
 - (a) Compute physical design field from filtering (3.12), (3.13) or MMOS (3.3) based on the design variables \mathbf{x}^k
 - (b) Solve FEM problem(s) (2.11) based on the physical design field
 - (c) Calculated objective function (2.8), (2.9) and constraints based on the physical design field
 - (d) Solve adjoint problem (3.16) and compute sensitivities (3.15) based on the physical design field
 - (e) Correct sensitivities for the design variables \mathbf{x} for filtering (3.21), (3.22) or MMOS (3.23)
 - (f) Update design variables \mathbf{x}^{k+1} using MMA
 - (g) Calculate change = $\|\mathbf{x}^{k+1} - \mathbf{x}^k\|_\infty$
4. end
5. Postprocess

If a projection filter is employed in the optimization process the projection parameter β is updated in a continuation scheme where the value of β is gradually increased from 1 to 512. A too close approximation of the Heaviside function initially may cause big oscillation in the convergence of the objective. Thus with a projection filter the pseudo code should be extended with

- (h) if $\text{mod}(k,50) = 1$ or change ≥ 0.01 and $\beta \leq \beta_{\max}$
 - i. $\beta = 2\beta$
 - ii. change = 0.2

Chapter 4

Topology optimized electromagnetic and acoustic cloaks

Rendering objects invisible to the human eye is a popular topic in science-fiction novels and movies, but it has been considered impossible by most people to achieve in the physical world. However, in 2006 two independent papers laid out the path of designing real-world cloaking devices for ray optics[64] and electromagnetic waves[65]. Roughly speaking an invisibility cloak is a device, which when wrapped around or placed nearby an object, renders the object and cloak invisible to an outside observer. An incident electromagnetic or acoustic wave is manipulated by the material of the cloak, such that the incident wave effectively is undisturbed outside the cloak and object. This way no scattering from the object (or cloak) are to be detected by the outside observer. Design of electromagnetic and acoustic cloaks by topology optimization constitute the first wave manipulation problem in this thesis. The chapter is a summary of publications [P1], [P2] and [P3].

4.1 Transformations Optics

The material layout of the aforementioned initial cloaks are determined by transformation optics[64, 65]. Transformation optics exploits that Maxwells' equations and thereby also the Helmholtz' equation are invariant under any coordinate transformation, as long as the material parameters (μ and ϵ) are changed appropriately by the transformation[66]. General coordinate transformations can be derived which compress, expand, bend or twist space. Such transformation can be utilized in wide range of electromagnetic problems. One approach to cloaking is to expand an infinitely small hole into the shape of the object, which should be made invisible. As the system is transformed it carries with it all the associated fields and electromagnetic waves are thereby excluded in a region of same size as the object. To give a flavor of how the transformation optic method works we demonstrate by an example adopted from [67]. In a cylindrical coordinate system (ρ, θ, z) we expand an infinitely small hole into a cylinder with the radius R_1 by compressing the ring-shape space between R_1 and an outer cylinder with radius R_2 , and get the following transformation

$$\rho' = (R_2 - R_1)\rho/R_2 + R_1, \quad \theta' = \theta, \quad z' = z \quad (4.1)$$

where $'$ denotes the transformed coordinates. With an appropriate change of the material properties Maxwell's equations are invariant to the coordinate transform. The appropriate change leads the transformed material parameters ϵ' and μ' to

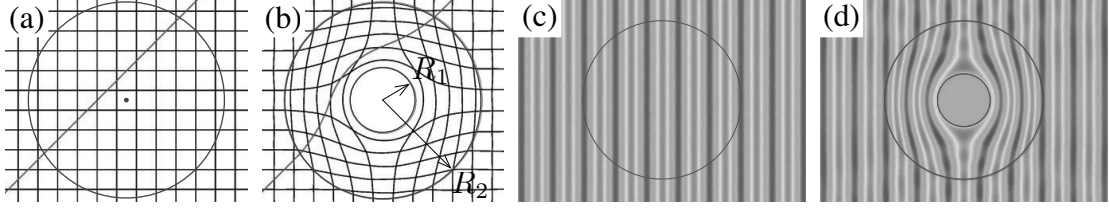


Figure 4.1 As a system is transformed it carries with it all the associated fields. A ray of light in an undistorted coordinate system (a) forms a straight line[16]. The space between R_1 and R_2 are compressed to exclude the cloaked region (b) by a the transformation given in equation (4.1). The ray is "glued" to the coordinates and is undistorted outside the compressed region. Wave propagation in a medium without (c) and with (d) transformed anisotropic material properties mimicking the coordinate transformation.

be anisotropic even though the original properties are isotropic. The transformed permittivity tensor is derived by $\epsilon' = \Lambda \epsilon \Lambda / \det(\Lambda)$ and equivalently for the permeability tensor by $\mu' = \Lambda \mu \Lambda / \det(\Lambda)$ where Λ is the Jacobian matrix given by $\Lambda_{i,j} = \partial r'_i / \partial r_j$. If free space constitute the material properties in the non-transformed space then the material properties undergoing a transformation given by equation (4.1) are inside the cloak region changed to

$$\epsilon'_{\rho'} = \mu'_{\rho'} = \frac{\rho - R_1}{\rho} \quad (4.2)$$

$$\epsilon'_{\theta'} = \mu'_{\theta'} = \frac{\rho}{\rho - R_1} \quad (4.3)$$

$$\epsilon'_{z'} = \mu'_{z'} = \left(\frac{R_2}{R_2 - R_1} \right) \frac{\rho - R_1}{\rho} \quad (4.4)$$

A uniform plane wave propagating in a medium with the above transformed anisotropic material properties will be manipulated to flow around the cylinder without scattering, c.f. figure 4.1. However, at the inner boundary of the cloak ($\rho = R_1$) some parameter components become singular ($\epsilon'_{\rho'} = \mu'_{\rho'} = \epsilon'_{z'} = \mu'_{z'} = 0$) while others ($\epsilon'_{\theta'}$ and $\mu'_{\theta'}$) goes to infinity. Another inherited problem of cloaking is that the part of the wave inside the cloak has to travel a greater distance than the part of the wave outside the cloak. This implies that the phase velocity inside the cloak needs to be greater than the velocity of light in vacuum. The group velocity cannot at the same time be faster than light, which means that the material parameters must be dispersive. In effect the cloak can only be operated in a narrow-band frequency range.

Furthermore, the presented object will not only be hidden from the outside world with the above approach, the outside world will likewise be hidden from the object. Complementary media remedies this by using media with negative refractive index to design cloaks that are not encircling the object[68, 69]. An even more exotic application of complementary media is illusion optics[70]. In illusion optics an object (e.g.

a spoon) is manipulated to generate a scattering pattern of a completely different object (e.g. a cup) and thereby give the illusion of being that object. Unfortunately no materials in nature possess extreme properties (zero or negative), which makes realizations challenging. A possible remedy to achieve extreme material properties is to use metamaterials.

4.1.1 Metamaterials

The concept of metamaterials is to tailor micro structures with a periodicity much smaller than the wavelength of the incoming wave. The incoming wave does not "see" the inhomogeneity of the individual micro structure due to the structure being sub-wavelength. Instead the wave reacts as if the material is homogeneous with effective material parameters given by the micro structure. This way it is possible to mix naturally occurring materials in a clever way to obtain certain properties which were otherwise not possible. The idea of metamaterials originates from Veselago who theoretically studied the effect of both permittivity and permeability being negative simultaneously[71]. Many years later Pendry proposed the designs of artificial structured materials which would have effectively negative permittivity and permeability[72, 73] and not long after the first metamaterial with negative index of refraction was demonstrated[74]. Shortly after the initial papers on transformation optics a cloak with approximated extreme anisotropic material properties was realized in the micro-wave regime using a structured metamaterial[75]. However, realizations at optical frequencies of the extreme properties even with metamaterials still remain challenging due to bandwidth-limitations, material absorption and not to mention fabrication difficulties of sub-wavelength artificial structures.

At a first glance the problem of systematic designing metamaterials using topology optimization to mitigate some of the challenges seems equivalent to designing materials with negative Poisson's ratio[76] and negative thermal expansion[20]. However, obtaining the effective parameters in a systematic and automated way, which is needed for the topology optimization method to be effective, has proven to be very challenging. The problem arises from branch ambiguities and that the parameters vary in a non-trivial way with the angle of incidence[77]. Several methods for extracting the effective parameters have been reported in the literature[78, 79, 80, 81] and based on such extraction methods metamaterials with negative permeability have been designed using topology optimization[82]. However, based on the study in [82] we do not find it worthwhile at the moment to proceed with double negative materials. Instead, we take a different path by designing the entire cloaking structure and thereby bypassing homogenization issues.

4.1.2 All-dielectric cloaking

Several alternative approaches to cloaking have emerged due to all the challenging problems that arise from extreme material parameters. The most prominent is the

”carpet cloak” approach developed by Li and Pendry in 2008[83]. The idea is to conceal a bump on a reflective surface. The reflective surface will effectively appear smooth when the ”carpet cloak” is placed on top of the bump. The material properties needed for the ”carpet cloak” can again be obtained by the transformation optics method and as it turns out the material properties for this class of cloaks are not extreme and can be realized with dielectric materials. Furthermore, the wave does not need to travel faster inside the cloak than outside and thereby circumventing the dispersion issue. These findings sparked a lot of interesting realizations in which both 2D and recently 3D macroscopic all-dielectric carpet cloaks in the optical regime have been demonstrated, c.f. [84, 85, 86, 87]. Other exciting studies on the use of naturally occurring materials in cloaking include hiding a particle[88]. In that study topology optimization is used to minimize the extinction efficiency of a particle by distributing ethanol and air.

In this thesis we return to the challenging problem of designing fully enclosing, all-dielectric cloaks and systematically address the intriguing question: ”How efficiently can we cloak when using conventional simple isotropic dielectric media readily available in nature?”. Permittivity values used in this study are all achievable with a broad range of naturally occurring transparent dielectric materials.

4.2 Method

We employ the standard density-based topology optimization method to minimize scattering from a strongly scattering cylindrical object illuminated by a uniform monochromatic propagating wave. Our investigations are restricted to non-magnetic materials ($\mu_r = 1$) and the background material is isotropic and defined by the permittivity, ϵ_r^{BG} . The in-plane wave propagation is perpendicular to the cylinder axis with either the E or H field being out of plane. Due to the invariance of the electromagnetic properties along the cylinder axis, the problem can be described by the Helmholtz’ equation for the E_z or H_z -polarized wave, c.f. equation (2.6). A first order absorbing boundary condition (ABS)[8] is used as an approximation to the Sommerfeld radiation condition in order to truncate the infinite domain. We mimic the strongly scattering cylindrical object by imposing a PEC boundary condition, $\mathbf{n} \times \mathbf{E} = 0$, at Γ_{PEC} . The general setup is illustrated by 3 concentric circles in figure 4.2. The inner, middle and outer domains represent the PEC cylinder, the cloak, and the surroundings, respectively.

The cloak domain wrapped around the cylinder is defined as the design domain, Ω_{des} , in which the relative permittivity can be varied continuously in the design process in order to minimize the norm of the scattered field. We interpolate linearly between a lower, ϵ_r^{min} , and an upper bound on the permittivity, ϵ_r^{max} . In contrast to most topology optimization problems intermediate values of the permittivity in the final design are in this problem both physically sound and realizable as graded index materials.

The incident field and the total field from the non-cloaked scattering object illu-

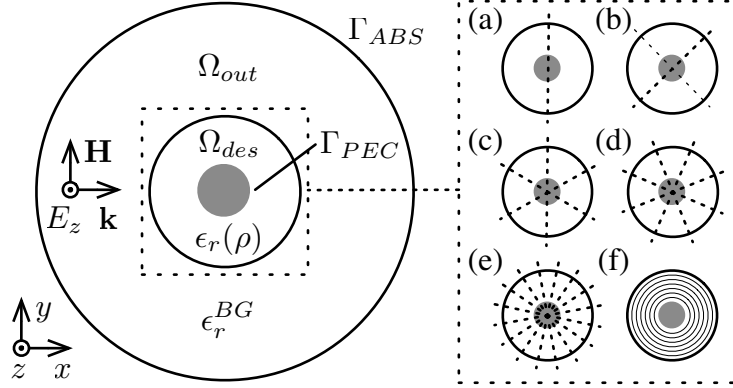


Figure 4.2 Computational Domain. The subfigures (a)-(e) show the design domains equipped with 1, 2, 3, 4 and 8 symmetry lines, respectively (PEC shown in red). The design domain with rotational symmetry is given in subfigure (f).

minated by an E_z polarized plane wave are shown in figure 4.3(a) and (b), respectively. The difference between the incident field and the total field is the scattered field generated by the scattering object. The interference pattern from the scattered field is very notable for the non-cloaked object especially as a shadow region behind the cylinder. The objective for the cloaking problem is to achieve zero scattering from the cloaked object in the surrounding space, Ω_{out} . Hence, the figure of merit in this thesis for evaluating the cloaking performance is given by the norm of the scattered field. The formulation of the optimization problem thus takes the form

$$\min_{\gamma} \quad \Phi_E = \frac{1}{W_E} \int_{\Omega_{out}} |E_z^s|^2 d\mathbf{r} \quad \text{objective function} \quad (4.5)$$

$$\text{subjected to} \quad \frac{1}{\int_{\Omega_{des}} d\mathbf{r}} \int_{\Omega_{des}} \gamma(\mathbf{r}) d\mathbf{r} - V_{max} \leq 0 \quad \text{volume constraint} \quad (4.6)$$

$$0 \leq \gamma(\mathbf{r}) \leq 1 \quad \forall \mathbf{r} \in \Omega_{des} \quad \text{design variable bounds} \quad (4.7)$$

where V_{max} is the maximum allowed volume fraction of material 2 and the subscript, E , reflect the polarization and W is the norm of the scattered field in the outer domain when no cloak is present. The reference value, W , is included in order to make the objective dimensionless as well as easy to interpret. By definition Φ is zero for the incident field (cf. figure 4.3(a)) and unity for the non-cloaked object (cf. figure 4.3(b)). Thus, if Φ is less than unity in the design process the object with a cloak wrapped around generate less scattering than the non-cloaked object.

4.3 Topology optimized all-dielectric cloaks[P1]

In the first study [P1] the evolution of the optimized designs along with the corresponding cloaking properties are investigated for increasing number of incident

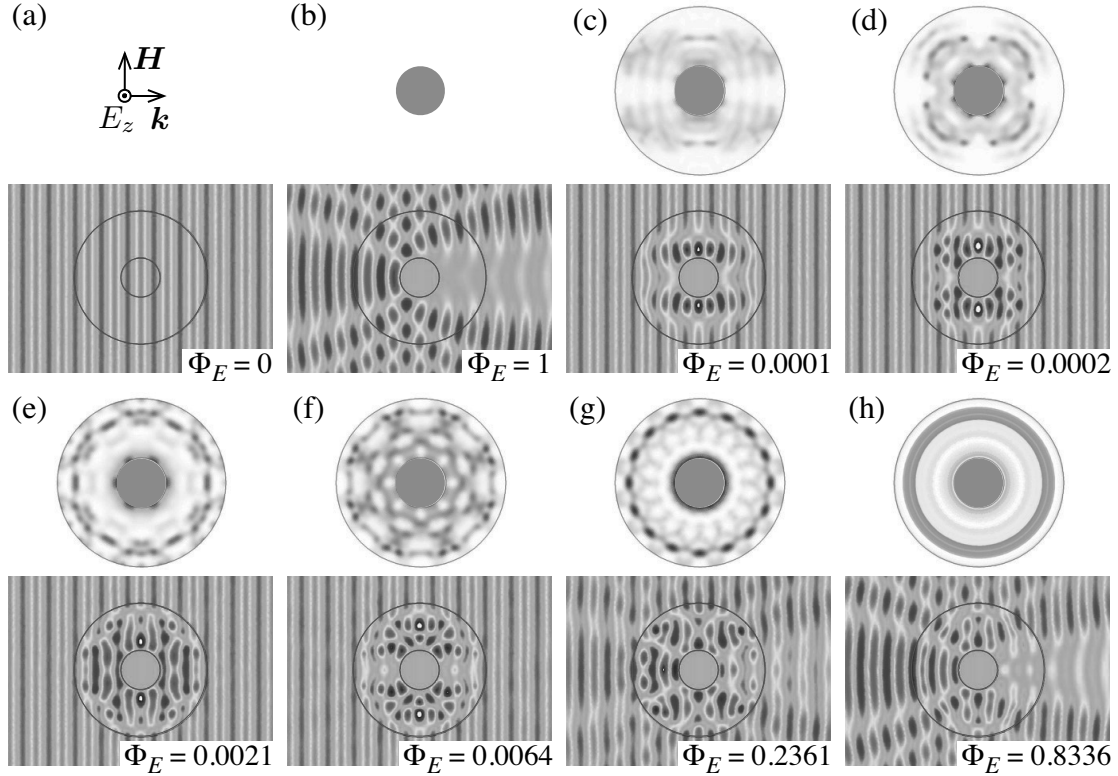


Figure 4.3 An E_z polarized plane wave (a) incident on a PEC cylinder (b) generate significant amount of scattering especially as a shadow region behind the cylinder. The optimized dielectric layout of the cloaks (c)-(h) for 1, 2, 3, 4, 8 and infinitely many symmetry lines manipulate the wave to flow around the cylinder such that scattering is minimized. The grey scale indicates the optimized relative permittivity distribution that ranges between 1 and 6.

angles, i.e. increased symmetry. Efficient optimization for multiple incident angles can be performed by introducing symmetry constraints on the design. Symmetry lines divide the original design domain into equally sized sub-domains in a number corresponding to the number of incident waves. As the number of angles goes to infinity the design becomes rotationally symmetric as sketched in figure 4.2(h). In this first study the background material is set to free space, $\epsilon_r^{\text{BG}} = 1$, and we interpolate between $\epsilon_r^{\text{min}} = 1$ and $\epsilon_r^{\text{max}} = 6$. We allow graded index to constitute the design profile.

Using the method outlined we have optimized for 1, 2, 3, 4, 8 and infinitely many symmetry lines (c.f. figure 4.3). When using 1 and up to 4 symmetry lines the optimized designs cloak the metallic cylinder nearly perfectly ($\Phi_E < 0.01$) for the considered angles of incidence. The optimized designs for 1-4 symmetry lines are basically waveguides, which guide and delay the waves inside the cloak and subsequently phase match them to the waves outside. However, the cloaking effect is highly localized to the considered angles of incidence for these 4 designs. In order to

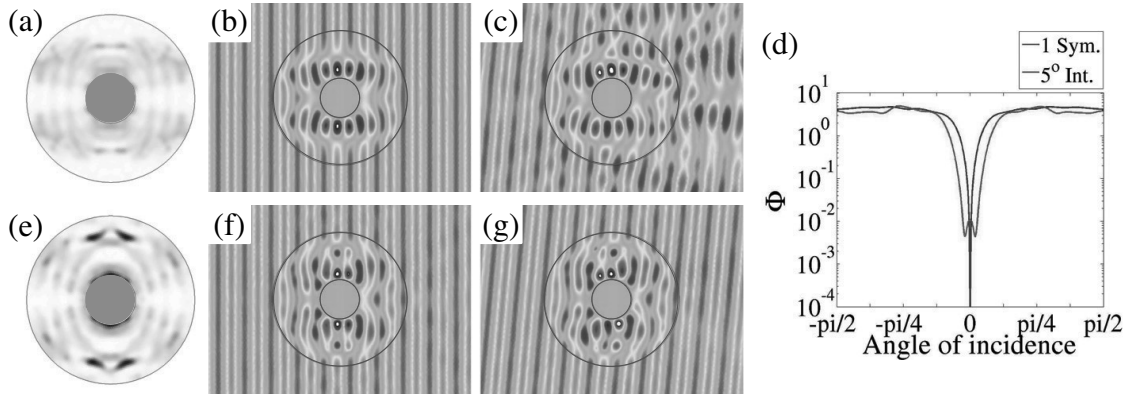


Figure 4.4 The cloak (a) for 1 symmetry line is near perfect at 0° (b) whereas significant scattering is generated at 5° (c) The dielectric layout (e) for the cloak optimized to operate in an interval from -5° to 5° are effective both for incident angles of 0° (f) and 5° (g). The robust design for small variation in the angle of incidence comes at the cost of increased scattering (d).

make the cloak more versatile to various angles of incidence, more symmetry lines are added to the design domain at the cost of increased objective value.

As mentioned above a slight variation in the incident angle results in a deteriorated cloaking performance. The cloak for 1 symmetry line is near perfect at 0° whereas significant scattering is generated at 5° as shown in figures 4.4(b) and (c). A robust design for small perturbations in the angle of incidence is obtained by illuminating with uniform waves incident in an interval from -5° to 5° on the design domain and cylinder. The optimization is formulated as a min/max problem, i.e. the load case, which yields the highest scattering in each iteration step is minimized. The angle sweep in figure 4.4(d) and the fields patterns in figures 4.4(f) and (g) clearly shows that the cloak from figure 4.4(e) can be operated in a broader incident angle interval at the cost of increased scattering.

4.4 Effect of polarization and background material[P2]

Finishing the initial study we wanted to pursue a realization of an all-dielectric fully enclosing optical cloak designed by topology optimization. In a possible future experimental setup it may be easier to confine the polarized propagating wave in a material with higher index than free space and let spatial distributed areas of free space constitute the optimized design profile of the cloak. This is the "inverse" case of the previous study, which was based on distributing material with a higher permittivity than the background material (free space). Intuitively, distributing dielectric material having a lower permittivity than the background material would result in cloaking performance on the same level or better, however, this is not the

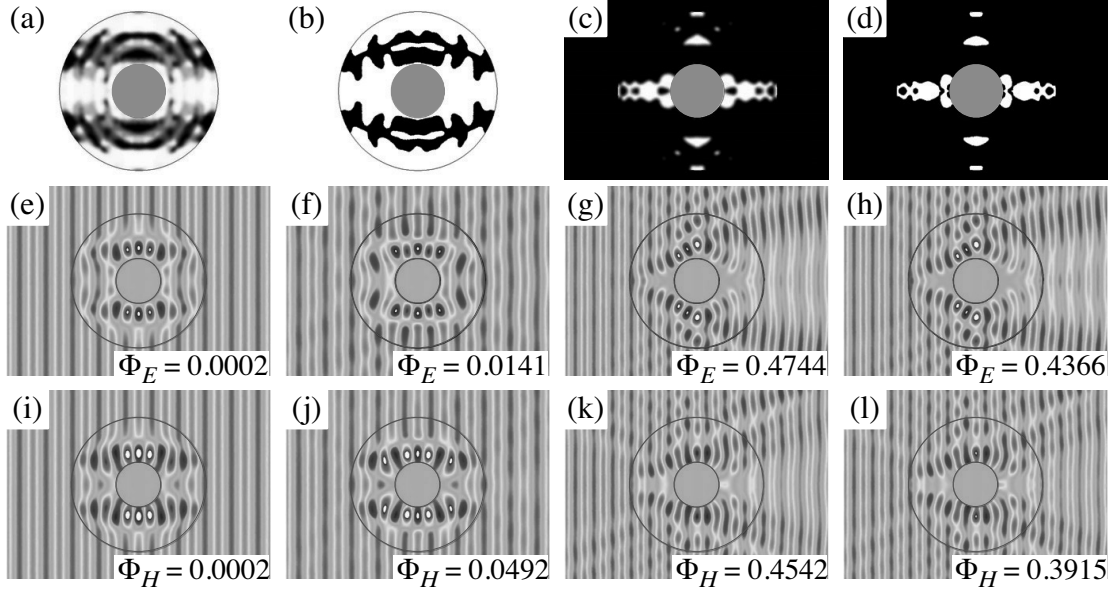


Figure 4.5 Polarization-independent cloak designs and the associated objective values $\Phi_{E,H}$ for E_z and H_z -polarized waves. The optimized material layouts is shown in the top panels as linear gray-scale plots, where white and black color correspond to $\epsilon_r = 1$ and $\epsilon_r = 2$. The middle and bottom panels show the total fields for E_z and H_z polarization, respectively. Both the graded (a) and discrete design (b) with $\epsilon_r^{\text{BG}} = 1$ reduce scattering significantly whereas the graded (c) and discrete (d) counterparts with $\epsilon_r^{\text{BG}} = 2$ generate notable scattering.

case as we will show.

Contrary to the previous study we also test the cloaking performance of discrete material designs, which do not permit intermediate values of the permittivity. Discrete designs are preferred compared to gradient index designs due to the more advanced fabrication technique needed for the gradient-index designs. Furthermore, in our initial study we only consider an E_z -polarized wave, but we are also interested to investigate how well a cloak optimized for an H_z -polarized wave perform or if it is even possible to find a cloak that works for both polarizations simultaneously? Especially the latter case of a design profile that minimize scattering from both E_z and H_z polarization simultaneously is interesting to study in order to go towards polarization-independent cloaks. Due to the limited cloaking performance when distributing material with lower permittivity than the background material, we switched the focus of the second cloaking problem to cloaks effective for both E_z and H_z polarization simultaneously. However, by doing so we could at the same time report our study on the effect of background material.

Discrete designs of the dielectric material are obtained by the deterministic robust formulation mentioned earlier. However, the robust formulation is here used in order to get simple designs and not as such to get designs that are robust to

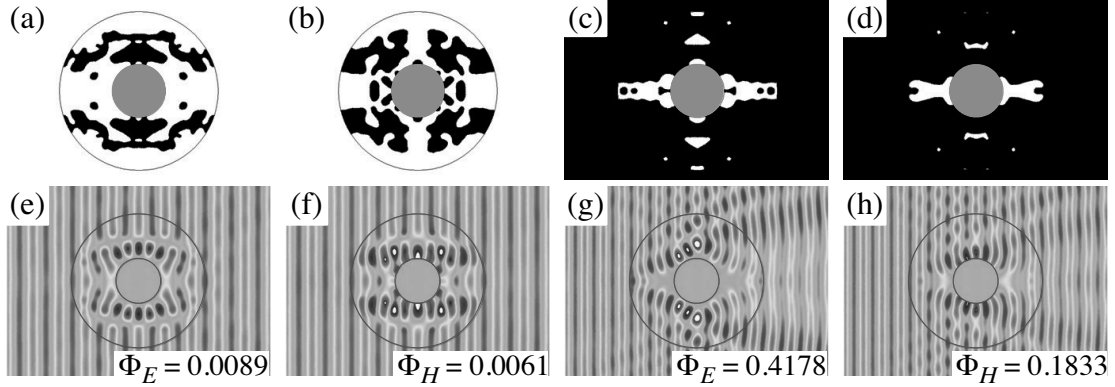


Figure 4.6 Polarization-dependent discrete cloak designs and the associated objective values. The bottom panels depict the total fields while the top panels show the optimized material layouts as linear gray-scale plots, where white and black color correspond to $\epsilon_r = 1$ and $\epsilon_r = 2$. The designs in panels (a) and (c) are optimized for E_z -polarization only whereas the designs in panels (b) and (d) are optimized for H_z -polarization. Even though the cloaks (c) and (d) with $\epsilon_r^{\text{BG}} = 2$ only is required to operate for one polarization, significant scattering is generated.

manufacturing defects. In this second study we vary the relative permittivity between $\epsilon_r^{\text{min}} = 1$ and $\epsilon_r^{\text{max}} = 2$ in the cloak domain wrapped around the cylinder. The permittivity of the background material, ϵ_r^{BG} , (cf. figure 4.1) is either set to 1 or 2, depending on whether we are distributing dielectric material having a higher or lower permittivity than the background material, respectively. A symmetry constraint is imposed on the design with two symmetry lines around which the 4 equally sized sub-domains can be mirrored. That is, the optimized cloaks only work for two incoming wave angles. A min/max formulation for Φ_E and Φ_H is employed to make the cloak equally effective for both E_z and H_z polarization.

Graded and discrete designs that minimize the scattering from both E_z and H_z polarization simultaneously are presented in figure 4.5 (top panels). The total fields for E_z and H_z polarization are shown in the middle and bottom panels, respectively. In case of $\epsilon_r^{\text{BG}} = 1$ the graded design result in scattering less than 1% of the non-cloaked cylinder and even for the more restrictive case with a discrete design scattering is reduced to less than 5% for both polarizations. The H_z polarization for the discrete design yielding less scattering than the E_z polarization, due to the less restrictive boundary condition for the H_z polarization. Contrary to simple intuition, considerable scattering is produced by all designs with $\epsilon_r^{\text{BG}} = 2$ and graded designs with $\epsilon_r^{\text{BG}} = 2$ produce more scattering than the discrete counter-parts. To analyze the cause for the degeneration in cloaking performance for designs with $\epsilon_r^{\text{BG}} = 2$ we relax the problem and investigate whether or not effective cloaks with $\epsilon_r^{\text{BG}} = 2$ can be designed individually for either the E_z or H_z polarization.

Discrete design profiles optimized individually for either E_z or H_z polarization and the corresponding total fields are shown in figure 4.6. Even though we relax

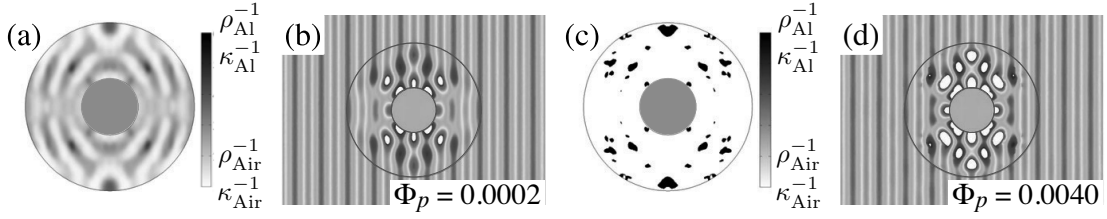


Figure 4.7 Acoustic cloak design and the associated objective values. A graded design of air and aluminum is included as a reference design in panel (a) and (b). A discrete design of air and aluminum with complex features is depicted in panel (c) and (d). The combined scattering pattern from the optimized complex sub-wavelength structures cancels the scattering from the big cylinder by a resonance effect

the problem and optimize individually for either one or the other polarization designs with $\epsilon_r^{\text{BG}} = 2$ result in poor cloaking performance. We thereby see that the limited cloaking performance for designs with $\epsilon_r^{\text{BG}} = 2$ is not caused by the requirement on the cloaks to be effective for both polarizations simultaneously. In stead we conclude that it is a consequence of optical modes tending to concentrate their electric or magnetic-field energy in regions of high dielectric values.[89] For the designs with $\epsilon_r^{\text{BG}} = 1$ the field energy is concentrated in regions of higher permittivity, wherein the wave is delayed and subsequently phase matched to the waves outside the cloak. For the designs with $\epsilon_r^{\text{BG}} = 2$ we can only design regions, which the field avoids. Hence it is possible to split the waves in front of the object with very limited backscattering. However, the waves cannot be collected on the backside of the object without scattering. The scattering is reduced by a factor of two for H_z polarization with $\epsilon_r^{\text{BG}} = 2$ compared with E_z polarization by coupling the wave into the surface mode, which makes it easier for the wave to flow around the object.

4.5 Topology optimized acoustic cloaks [P3]

Cloaking devices are mainly associated with electromagnetic waves as studied above. However, objects can also be cloaked for other types of waves such as elastic waves in thin-elastic plates[90, 91], plasmonic surface waves[92], matter waves [93], surface waves in a fluid[94] and acoustic waves[95]. Following our success of designing electromagnetic cloaks it is natural to extend our numerical setup and attack similar physical problems with the outlined method. Especially realizing acoustic cloaks have shown to be very challenging in practice.

In contrast to Maxwell's equations, the elasticity equations are not invariant under coordinate transformations[96]. However, in Refs. [95, 97] it is shown that the material layout in cloaks for acoustic waves in a fluid-like materials can be found with the same technique of transformation optics (by some referred to as transformation acoustics). Unfortunately, transformation acoustics results in an inhomoge-

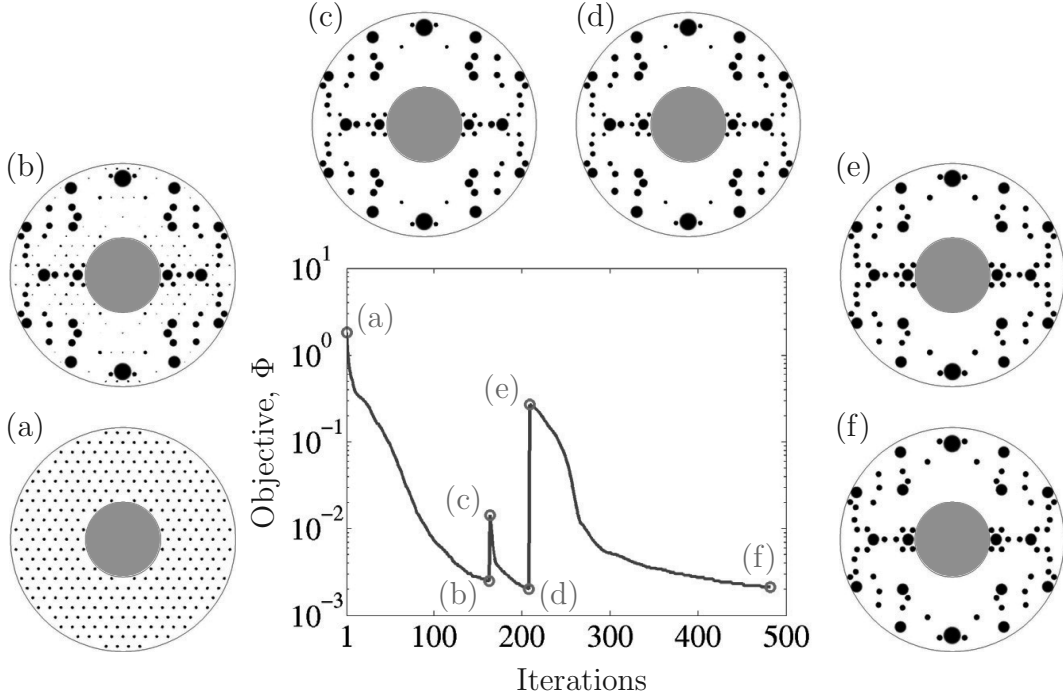


Figure 4.8 A three-step MMOS based optimization approach for acoustic cloak design with cylindrical aluminum inclusions in air. (a): The design is initialized using 306 aluminum cylinders. (b): Optimized design where the cylinders can change in size and position. (c): Cylinders with a radius smaller than 0.25 cm are discarded. (d): Optimized design with a lower bound on the radii. (e) Radii of all cylinders are rounded off to 0.5 cm, 1.0 cm or 1.5 cm. (f): Final design after reoptimizing the positions of the cylinders.

neous and anisotropic mass density, which is not common in naturally occurring fluids, thus making realizations very challenging. Equivalent to the electromagnetic carpet cloak approach the acoustic problem can also be relaxed to that of hiding objects on a reflecting surface[98] and a recent realization for airborne sound has been reported[99]. A fully enclosing acoustic cloak for underwater ultrasound has also been realized [100] based on an acoustic transmission line approach. As such most of the reported work are concentrated on realizing the anisotropic material parameters with engineered acoustic metamaterials[101, 102, 103]. However, our goal in this problem is with a limited reformulation to use the initial methodology of designing optical cloaks to design an acoustic cloak with isotropic material properties to circumvent the problems of the anisotropic mass density.

For the acoustic case air and solid material (aluminum) are redistributed in the cloak domain in order to minimize the norm of the scattered pressure field ($p^s \leftrightarrow E_z^s$ in equation (6.2)) in the surrounding domain, Ω_{out} . In the electromagnetic cloak only one of the material properties (ϵ_r) is varied, whereas in the acoustic case both density, ρ , and bulk modulus, κ are redistributed in the design process. Here the inverse material properties are interpolated linearly.

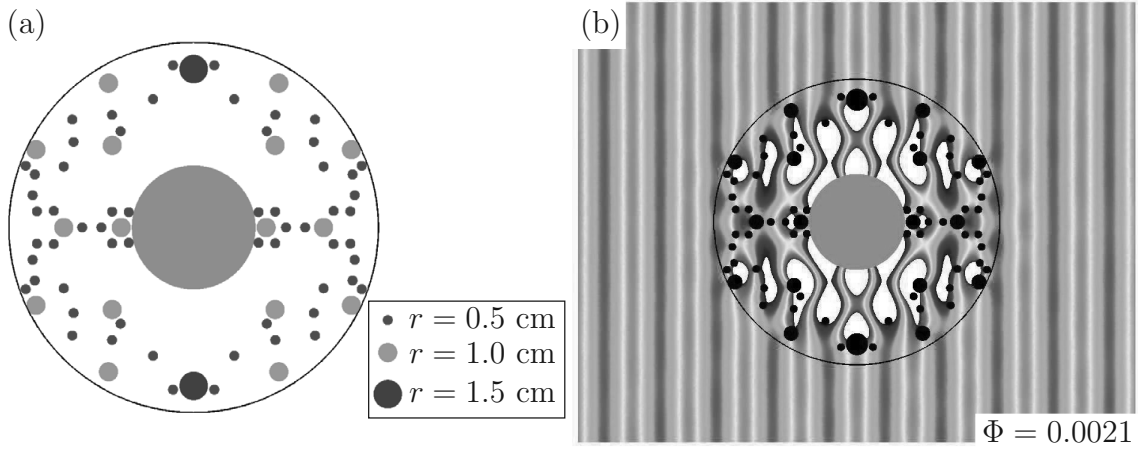


Figure 4.9 The final optimized design of an acoustic cloak with cylindrical aluminum inclusions in air is shown in panel (a). The radii of all cylinders are constrained to take discrete values of either 0.5 cm, 1.0 cm or 1.5 cm to aid realizations. Near perfect cloaking is obtained with the optimized cylinder placement as seen from panel (b). The combined scattering pattern from the optimized sub-wavelength structures cancels the scattering from the big cylinder by a resonance effect.

In the numerical setup a pressure field with a driving frequency of 4367 Hz is incident on an aluminum cylinder with a radius of 6.7 cm. A cloak with a radius of 20 cm is wrapped around the aluminum cylinder. Discrete designs are ensured because graded designs with a linear interpolation between air and solid material is difficult to interpret in practical realizations. Nevertheless, an optimized design profile with intermediate material properties is included here as a reference (c.f. figure 4.7(a)). The discrete profile (figure 4.7(c)) clearly shows that also acoustic cloaks can be designed using the outlined optimization method. Contrary to the electromagnetic cloaks the working principle for the acoustic cloaks is not to change the speed of the wave. Instead the acoustic cloaks rely on a resonance effect such that the combined scattering pattern from the optimized sub-wavelength structures cancels the scattering from the big cylinder. However, the optimized discrete profile is very challenging (next to impossible) to manufacture, because of the complex structure. An attainable realization should rather be based on scatters with very simple and identical feature shapes; preferably small aluminum cylinders. Thus we apply the MMOS design parametrization described in the preceding chapter such that cylindrical aluminum inclusions in air constitutes the design.

The optimization is performed in three step. First the design is initialized (c.f. figure 4.8(a)) using 306 aluminum cylinders, which are allowed to move both in position and change in size during the optimization. The radii are initially not restricted by lower or upper bounds, which means that cylinders effectively can disappear as their radius becomes infinitely small. After the first convergence shown in figure 4.8(b) cylinders with a radius smaller than 0.25 cm are discarded. With a lower

bound on the radii of 0.25 cm no cylinders can disappear and a second optimization finds an optimized design with cylinders of varying radius (cf. figure 4.8(d)). Finally all the radius of all cylinders are rounded off to either 0.5 cm, 1.0 cm or 1.5 cm as shown in figure 4.8(e) and a reoptimization with fixed radii gives the final design, figure 4.8(f). The first step ensures that the topology can change (i.e. cylinders disappear) and the last step makes the design easy to manufacture.

The final optimized design of an acoustic cloak with cylindrical aluminum inclusions in air is shown in figure 4.9(a). Aluminum cylinders with discrete radii constitutes the design resulting in near perfect cloaking, c.f. figure 4.9(a). The graded and discrete design from figure 4.7 poses some of the same features, e.g. a big aluminum inclusion above the cloak. As it turned out a Spanish group[104] had pursued an idea almost identical to ours. They published their results with an experimental verification, while we gathered information on how to realize our acoustic cloak. However, it was thereby demonstrated that acoustic cloaks can be designed by placing sub-wavelength scatters around the object.

Chapter 5

Backscattering cloak

Encouraged by the results from the topology optimized cloaks reported in the previous chapter we looked for further ways to extend the cloak analysis. Here we relax the full cloaking problem by only requiring elimination of backscattering in a limited angular range. The less restricted case of cloaking enables us to concentrate our study to omnidirectional designs, based on concentric rings of isotropic, low-contrast, all-dielectric materials readily available in nature. Optimized annular cloaks have previously been proposed in the literature (cf. Ref. [105]), however the optimized anisotropic material properties are not easily realizable. Although relaxed compared to the full cloaking problem, backscattering cloaks are highly relevant in e.g. radar-setups where source and detector are coincident. The results presented here are examples of the findings given in [P4].

With very little reformulation the optimization approach reported in the last chapter can easily be extended to the backscattering problem. However, the symmetry of omnidirectional ring design allows us to compute the electromagnetic field analytically[106, 107, 108]. Derivations of e.g. the far-field on an arc line is much faster using an analytic expression compared to a FEM solution and ring positions are not restricted to an underlying mesh. On the other hand the analytic expression can only be implemented in a sizing optimization of e.g. ring position and thickness thereby loosing some of the design freedom provided by topology optimization. For the above reasons we choose a two step approach in order to benefit from the advantages of each method. First we use topology optimization to provide us with basic understanding of the optimized topology. Next a parametrization of the topology optimized designs is used in the optimization approach based on the analytic expression.

5.1 Topology optimized backscattering designs

The setup for the topology optimization problem is almost identical to the one outlined in the previous chapter. Here we minimize the norm of the E_z polarized scattered field in a circular trapezoidal domain enclosed at $\pm 10^\circ$ from the backscattering direction and with inner and outer radii given as 1.75 and 5 free space wavelengths from the obstacle, respectively (see Ω_{out} in Fig. 5.1(a)). The permittivity is allowed to vary between $\epsilon_r^{\min} = 1$ and $\epsilon_r^{\max} = 2$ with free space being the background material.

The results of the optimization process are surprisingly simple annular Bragg-like grating structures with layer dimensions that depend on the obstacle radius

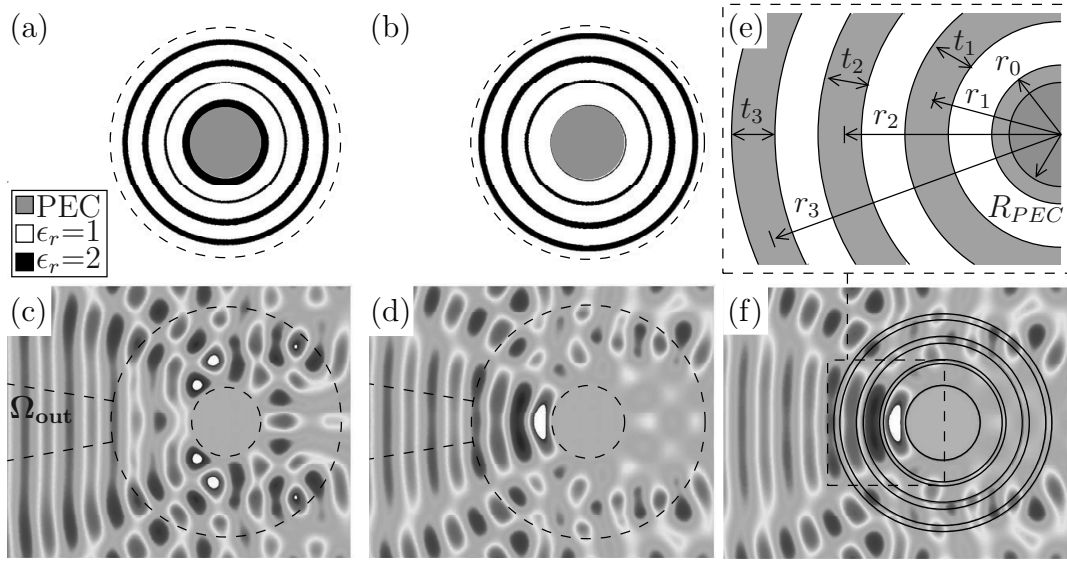


Figure 5.1 (a), (b): Topology optimized designs for R_{PEC}/λ ratios of 0.8 and 0.83, respectively, and total fields (c), (d) calculated by finite element analysis. (e): The positions of layers with $\epsilon_r = 2$ are represented by 7 parameters for a 3 layer structure. (f) Total field for $R_{PEC}/\lambda = 0.82$ obtained by the analytic solution.

R_{PEC} . An optimized design (Fig. 5.1(a)) with a thin coating of the obstacle surrounded by three concentric rings is obtained for a radius to free space wavelength ratio of $R_{PEC}/\lambda = 0.8$. A slightly increased cylinder radius ($R_{PEC}/\lambda = 0.83$) almost eliminates the inner coating layer. Extensive numerical analysis show similar layered patterns with varying thickness of the inner coating layer for other R_{PEC}/λ ratios. The amplification of the total field in the layered region indicates that the optimized structure acts as an annular Bragg grating with a defect introduced by the PEC cylinder[109]. For a flat obstacle the incoming wave would simply be reflected, however, due to the curvature of the grating, the incoming wave couples to circumferentially propagating and confined ring modes that lead the energy around the obstacle, resulting in scattering in all but the backscattering direction.

5.2 Analytic solution of the Helmholtz' equation

The simple geometry of an omnidirectional discrete ring design makes it possible to solve the Helmholtz' equation analytically in a cylindrical coordinate system (ρ, θ) when the material in each ring is homogeneous. A E_z polarized plane wave propagating in the positive x -axis in a standard cartesian coordinate system can be described in a cylindrical coordinate system using cylindrical wave transformation[2]

$$E_z^i = E_0 e^{-jk_0 x} = E_0 \sum_{n=-\infty}^{\infty} (j)^n J_n(k_0 \rho) e^{jn\theta} \quad (5.1)$$

where $j = \sqrt{-1}$, $E_0 = 1$ is the normalized amplitude of the incident plane wave, n is the summation order, J_n is the n 'th bessel function and k_0 is the wave number in the outer region. The scattered field, E_z^{sc} , in the outer region is given as

$$E_z^s = E_0 \sum_{n=-\infty}^{\infty} (j)^n A_n H_n^{(1)}(k_0 \rho) e^{jn\theta} \quad (5.2)$$

where $H_n^{(1)}$ are the Hankel functions of the first kind (outward propagating cylindrical wave) and A_n are the unknown coefficients, which can be determined from the boundary conditions. The total field, E_z^t , in the outer region can be found as the sum of the incident, E_z^i , and scattered field, E_z^s , whereas in ring m the total field is given as a superposition of an in- and outgoing cylindrical wave

$$E_z^t = E_0 \sum_{n=-\infty}^{\infty} (j)^n [B_n H_n^{(2)}(k_m \rho) + C_n H_n^{(1)}(k_m \rho)] e^{jn\theta} \quad (5.3)$$

where $H_n^{(2)}$ is the Hankel function of the second kind (inward propagating cylindrical wave), B_n and C_n are unknown sets of coefficients to be determined by the boundary conditions.

Apart from the PEC boundary condition at the innermost boundary, two independent continuous boundary conditions and two sets of unknown coefficients are introduced for each boundary yielding a linear equation system to be solved. The total field (c.f. figure 5.1(f)) obtained from the analytic solution with the extracted positions of the layers from the topology optimized design for $R_{PEC}/\lambda = 0.83$ shows almost perfect agreement with the finite element solution.

5.3 Method

From the topology optimized designs we see that the layered design should start with a high index ($\epsilon_r = 2$) layer as the innermost ring (coating) and alternate between free-space and high index material. Based on this interpretation, the topology of the rings can be parameterized as shown in Fig. 5.1(e). The outer radius of the coating layer is given by r_0 and ring n is parameterized by its center radius r_n and its thickness t_n . Together with the analytical solution from equation (5.2), these parameters are used as inputs to a simpler optimization procedure based on the `fmincon` function in Matlab. Here we minimize the norm of the scattered field on a $\pm 10^\circ$ arc line Γ_{out} , in the far-field (e.g. $\rho = 60\lambda$) of the backscattering direction. This allows some scattering to occur in the near-field of the cloak, but minimizes scattering in the far-field. Furthermore, simple geometric constraints on the design are included to prevent overlapping boundaries, which would corrupt the analytic solution. Given the analytic solution to the scattered field from equation (5.2) the

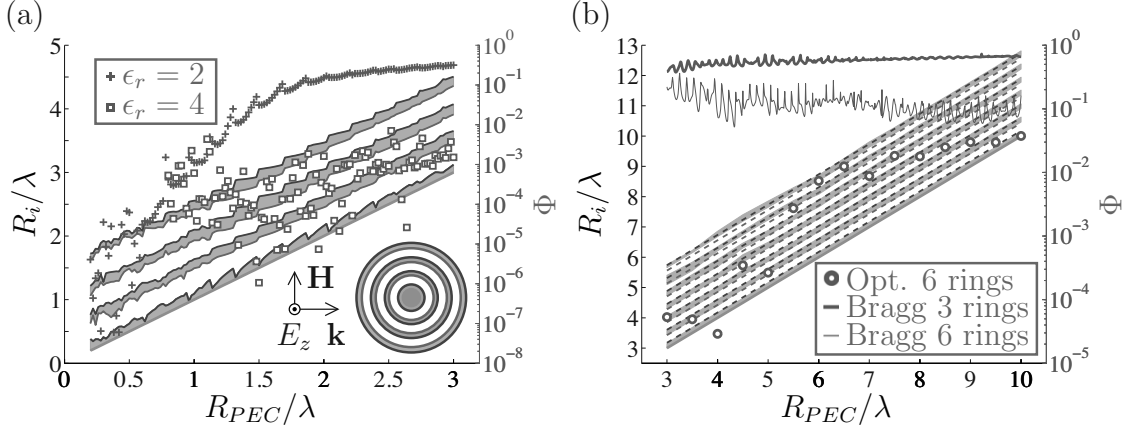


Figure 5.2 (a): Optimized positions of 3 rings (a) illuminated by an E_z -polarized plane wave and the cloaking performance for $0.2 \leq R_{PEC}/\lambda \leq 3.0$. Left axis represents the optimized positions of the inner (red) and outer (blue) boundaries for the $\epsilon_r = 2$ layers. Cloaking performance for $\epsilon_r = 2$ (crosses) and $\epsilon_r = 4$ (squares) are given by the right axis. (b): Optimized positions, represented by the gray-shaded areas, of a 6-ring ($\epsilon_r = 2$) cloak and the cloaking performance (squares) for $3.0 \leq R_{PEC}/\lambda \leq 10.0$. Dashed red and blue lines represent the positions of conventional quarter-wavelength annular Bragg grating with corresponding cloaking performance given by the solid green lines.

optimization problem is formulated as

$$\min_{r_n, t_n} \quad \Phi = \frac{1}{W} \int_{-10^\circ}^{10^\circ} |E_z^s(\rho = 60\lambda, \theta)|^2 d\theta \quad \text{objective function} \quad (5.4)$$

$$\text{subjected to} \quad r_0 - R_{PEC} > 0 \quad \text{design variable bound} \quad (5.5)$$

$$(r_1 - t_1) - r_0 > 0 \quad \text{design variable bound} \quad (5.6)$$

$$(r_n - t_n) - (r_{n-1} - t_{n-1}) > 0 \quad \text{design variable bounds} \quad (5.7)$$

$$t_n > 0 \quad \text{design variable bounds} \quad (5.8)$$

where W is the norm of the scattered field on Γ_{out} for the non-cloaked PEC cylinder.

5.4 Results

Good cloaking performance is achieved for 3 position and thickness optimized high index ($\epsilon_r = 2$) layers when $R_{PEC}/\lambda < 1.3$, however for larger ratios the cloaking performance deteriorates. The cloaking performance can be improved significantly in several ways. Increasing the permittivity in the high index rings and reoptimizing the positions and thicknesses of the rings enables higher amplification and a higher confinement of the ring modes, such that backscattering can be reduced more efficiently. Increasing the number of high index rings and thereby giving the optimizer more freedom is another intuitive way of improving the cloaking performance as seen

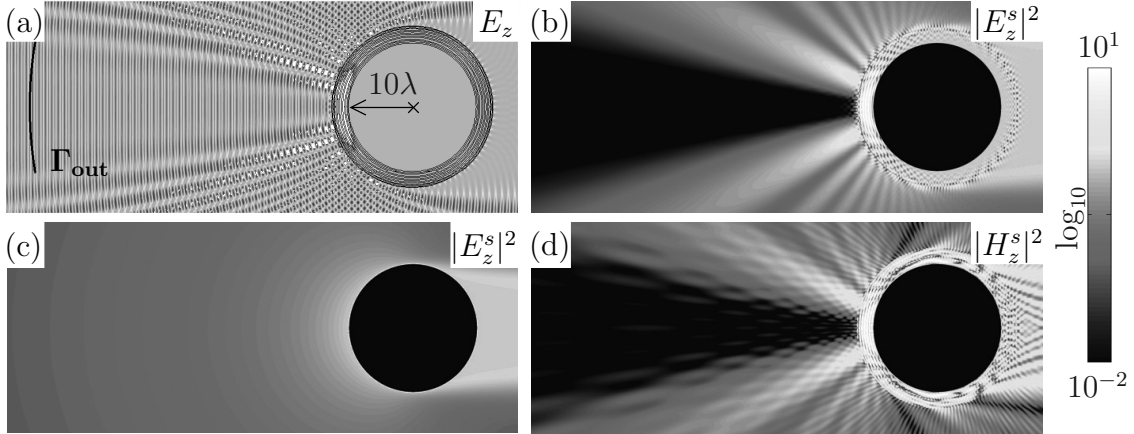


Figure 5.3 Total field (a) for an optimized 6-ring cloak ($\epsilon_r = 4$, $R_{PEC}/\lambda = 10$) illuminated by an E_z -polarized wave. Norms of the scattered field are given in a \log_{10} -scale for the non-cloaked (b) and the cloaked PEC cylinder (c). Even if illuminated by an H_z -polarized plane wave (d) the E_z -optimized cloak shows good backscattering performance.

in figure 5.2(b). Furthermore, if the requirement to the size of the angle interval is relaxed, we can get significantly stronger reduction of the backscattering in the reduced angular range as one would expect.

We have tried to identify a simple rule for the optimal dimensions of the cloak. However, the problem is more complicated than for simple annular Bragg resonators[110] due to the coupling of the incoming wave to the circumferential waves. The semi-periodic variation of the radius of the inner coating is attributed to the optimized structure adapting itself to new ringmodes that enable the confinement. Since the effective circumferential index is hard to define we do not believe that it is possible to determine a closed-form rule for the optimal dimensions of the cloak. Nevertheless, we compare our optimized results with a simple quarter-wavelength annular Bragg cloak with high index material starting in the innermost layer (coating) and find fairly good behavior - especially for larger obstacle radii. Furthermore the layout and the cloaking performance for the optimized 6-ring structure converge to those of the corresponding simple annular Bragg grating, when the radius of the PEC cylinder becomes much larger than the wavelength.

By combining the above findings an optimized 6-ring structure ($\epsilon_r = 4$) illuminated by an E_z -polarized wave obtain good cloaking performance even for a large cylinder radii ($R_{PEC} = 10\lambda$), c.f. figure. 5.3. Even though the radius of the PEC cylinder is 10 times the wavelength the norm of the scattered field in the backscattering direction is less than 2% of the norm of the scattered field from the non-cloaked cylinder. The outlined optimization procedure can equivalently be used in the H_z -polarized case. However, a simple quarter-wavelength Bragg grating is polarization independent and as expected the E_z -optimized cloak also shows good backscattering performance when illuminated by an H_z -polarized plane wave, c.f. figure 5.3(d).

Chapter 6

Efficiently coupling into the surface plasmon mode

In the previous problems we have seen how topology optimized designs can manipulate waves such that scattering from an obstacle have been eliminated almost perfectly in all directions or in a specified angular range. For other types of wave problems it might be of interest to manipulate waves to propagate in a specified direction. The wave manipulation problem studied in this chapter is about the efficient excitation of surface plasmon polaritons propagating along a dielectric-metal interface. Topology optimization is employed to find topologies for grating couplers, such that the in and out-coupling efficiency of the plasmonic surface waves are maximized. The chapter is a summary of publication [P5].

6.1 Surface plasmon polaritons

The effects of Surface Plasmons (SPs) were first reported in the literature in the beginning of the 20th century by Wood[111], however localized surface plasmon resonance have been used to give color in stained glass for thousands of years[112]. 50 years later Ritchie predicted in 1957 the existence of surface plasmons at metal surfaces. Within the last 15 years many novel discoveries (e.g. enhanced light transmission[113]) have sparked an increased interest for surface plasmons to be utilized in optical devices, e.g. photonic circuits[114], subwavelength waveguides[115] and solar cells[116].

Overall, surface plasmon can be divided into two categories[117], surface plasmon polaritons (SPP) propagating on plane surfaces and localized (non-propagating) surface plasmons in small subwavelength nano-particles. In this work we will concentrate our focus on the former. SPPs are collective charge oscillations of a conductor's free electron gas (cf. figure 6.1) creating regions of high charge density (+) and low charge density (-). This motion effectively creates a traveling longitudinal electron wave equivalent to the longitudinal acoustic pressure wave. The longitudinal electron wave is coupled to an external electromagnetic field that propagate along an interface between a metal with negative real part and a dielectric with positive real part of the permittivity[118]. The electric field oscillates in the (x, y) -plane making the SPPs transverse magnetic on a plane perpendicular to the interface, hence the magnetic field is polarized in the z -direction as shown in figure 6.1. The SPPs are confined at the interface due to a momentum (energy) mismatch between the SPPs and the incident wave. Simply shining light on a plane surface will not excite the SPPs, cf. figure 6.1(c). Coupling to the SPP mode can be performed by grating couplers[119], prism couplers[120, 121], near-field excitation[122], end-fire

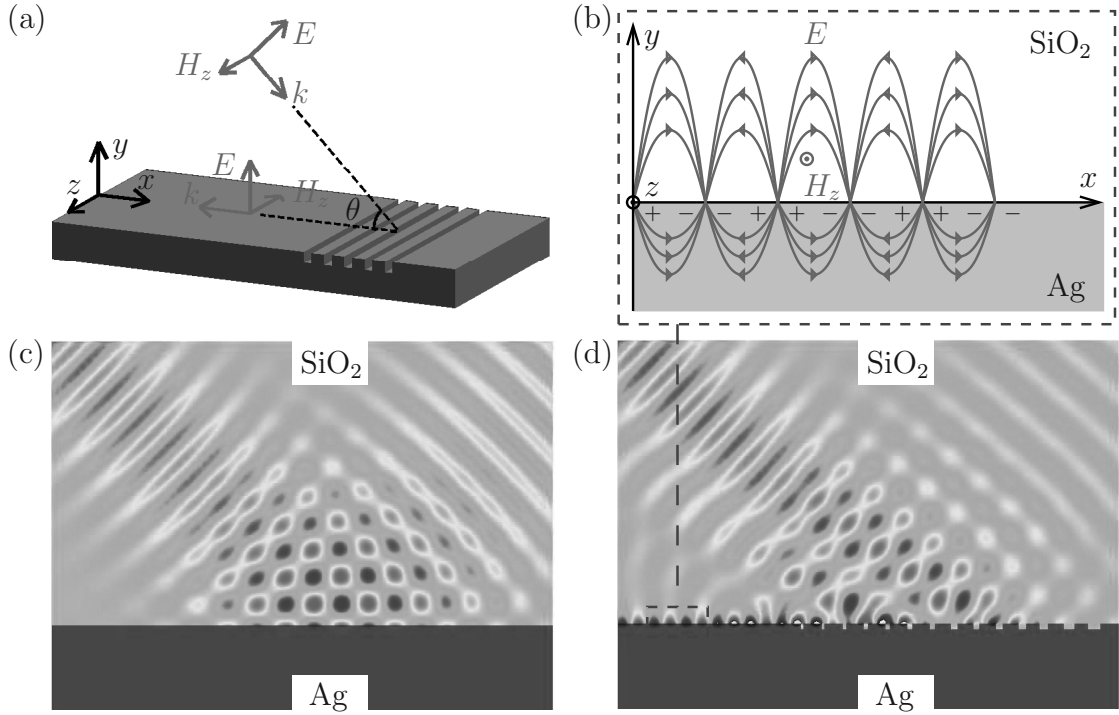


Figure 6.1 Utilizing a grating coupler (a) a SPP (b) is excited at the interface between a metal and a dielectric. The collective charge oscillations (b) results in regions with low(-) and high(+) surface charge densities. An electric field, E , can couple to the charge oscillations in the (x, y) -plane and thereby forcing a magnetic field to be polarized in the z -direction. Without any coupling mechanism the incident wave will be reflected (c), however a grating coupler (d) phase-match the parallel wave-vector component of the incident field to that of the SPP mode.

couplers[123] and broad-side couplers[124]. We will in this work concentrate our attention to grating couplers. The working principle of grating couplers is to match the parallel wave vector component of an incident field to that of the SPP using topological defects at the surface, e.g. grooves. An excited SPP are likewise bound to propagate along the metal-dielectric interface until energy is lost via absorption in the metal or the SPP encounters a grating coupler and are coupled out again.

Design of grating couplers consist of determining the spatial distribution of metal and dielectric material that enables an efficient excitation of SPPs, thus making it a good candidate problem for the topology optimization approach. Several studies [125, 126, 127, 128, 129] on the effect of different groove designs in regards to coupling efficiency have been reported in literature. However, most of the studies are limited to geometric parameter studies combined with heuristic search schemes. Lately, in [130] a systematic optimization of coupling into a SPP mode was performed. Using a hierarchal search optimization algorithm, varying the width and position of 14 grooves the authors achieved an impressive excitation efficiency of

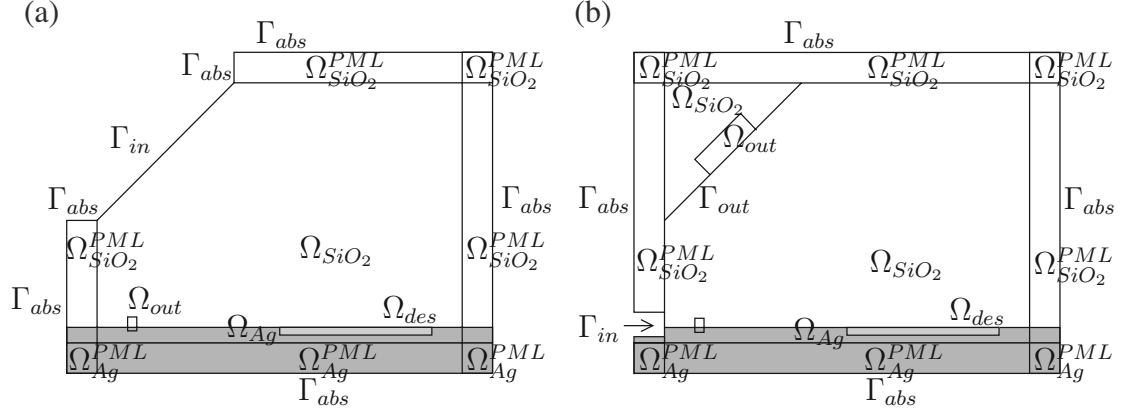


Figure 6.2 Computational models for the input and output couplers containing a dielectric (Ω_{SiO_2}), a metal (Ω_{Ag}), and a design domain (Ω_{des}). A plane wave is excited at Γ_{in} . A SPP will be induced at the interface between the two media and the power flow is measured in the domain Ω_{out} . To avoid reflections from the boundaries, PML domains Ω_{PML} and absorbing boundary condition Γ_{abs} have been introduced.

50%. The optimized grating coupler from [130] is employed in figure 6.1(d) to visualize the excitation of a SPP. In contrast to heuristic search approaches the topology optimization method do not limit the grooves to a certain shape, e.g. rectangular, but allow free shapes and topologies. In this study we employ the topology optimization method to determine efficient topologies for both in and output grating couplers.

6.2 Method

Material and geometry settings from [130] are here reused. The computational models for the input and output couplers are sketched in figures 6.1 (a) and (b), respectively. Both models consist of a SiO_2 -domain, Ω_{SiO_2} , an Ag -domain, Ω_{Ag} , and a design domain, Ω_{des} , where SiO_2 and Ag shall be distributed freely. Reflections from the boundaries are eliminated using perfectly matched layers (PML)[9]. Furthermore, first order absorbing boundary conditions, Γ_{abs} , have been introduced on all outer boundaries[8]. The design domain, Ω_{des} , has a width and height of $2.5 \mu m$ and 50 nm , respectively. Following the standard density approach from topology optimization, the material distribution in the design domain, Ω_{des} , can be changed by varying the permittivity of individual finite elements continuously between the material values for SiO_2 and Ag . The following interpolation models the relation between element densities and element permittivities

$$\epsilon_r(\gamma_e) = \epsilon'_{Ag} + \gamma_e(\epsilon'_{SiO_2} - \epsilon'_{Ag}) - j[\epsilon''_{Ag} + \gamma_e(\epsilon''_{SiO_2} - \epsilon''_{Ag})] + j4d(\gamma_e^2 - \gamma_e) \quad (6.1)$$

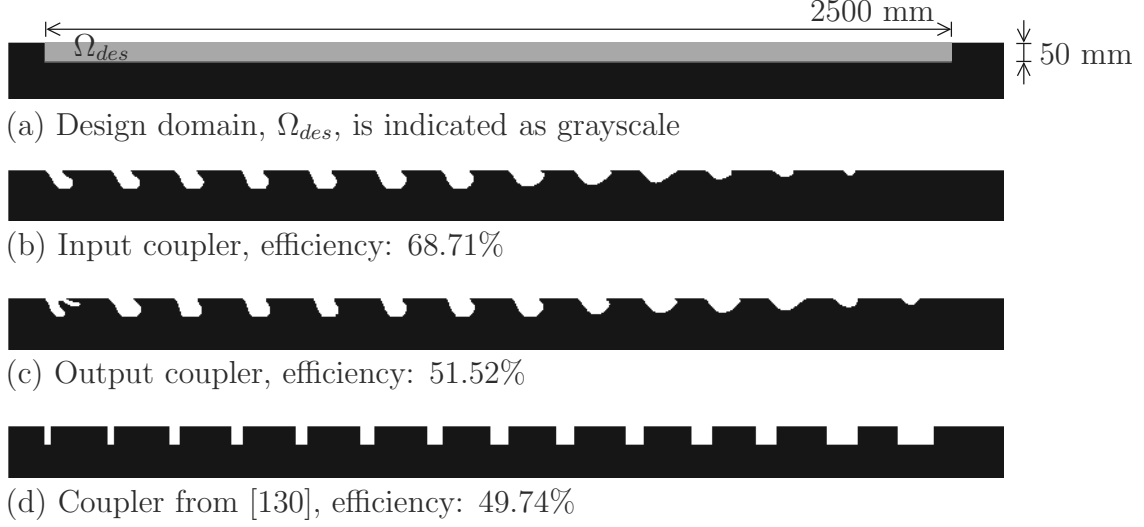


Figure 6.3 Optimized designs of an in and output grating coupler.

where ' and ', respectively, denote the real and the imaginary parts of the permittivity for the given material and d is a factor introducing artificial damping. This damping induces an energy loss for intermediate values of γ and disfavors non-discrete values in the final design [31].

The objective of this optimization problem is to maximize the power flow (averaged Poynting vector), in the domain Ω_{out} in the negative direction of the x -axes, $\mathbf{n} = (-1, 0)$, for the input coupler and in the beam direction, $\mathbf{n} = (-\sqrt{2}/2, \sqrt{2}/2)$, for the output coupler. Thus the optimization problem is formulated as

$$\max_{\gamma} \Phi(H_z(\gamma)) = \int_{\Omega_{out}} \frac{1}{2\omega} \text{Re} \left[i\epsilon_r^{-1} H_z^* \nabla H_z \right] \cdot \mathbf{n} \, d\mathbf{r} \quad \text{objective function} \quad (6.2)$$

$$\text{s.t.} \quad \frac{1}{\int_{\Omega_{des}} d\mathbf{r}} \int_{\Omega_{des}} \gamma(\mathbf{r}) \, d\mathbf{r} - V_{\max} \leq 0 \quad \text{volume constraint} \quad (6.3)$$

$$0 \leq \gamma(\mathbf{r}) \leq 1 \quad \forall \mathbf{r} \in \Omega_{des} \quad \text{design variable bounds} \quad (6.4)$$

where \mathbf{n} gives the direction of the power flux. The decay length of the surface plasmon, its skin-depth in the two materials and the generated power flow are used to evaluate the efficiency of the coupling in the post-processing step.

6.3 Results

For the input coupler a time-harmonic wave is excited at Γ_{in} with a free-space wavelength of 476 nm. The wave is Gaussian shaped with full width half maximum = $1\mu\text{m}$ and has an incident angle of 45° . For the output grating coupler the surface

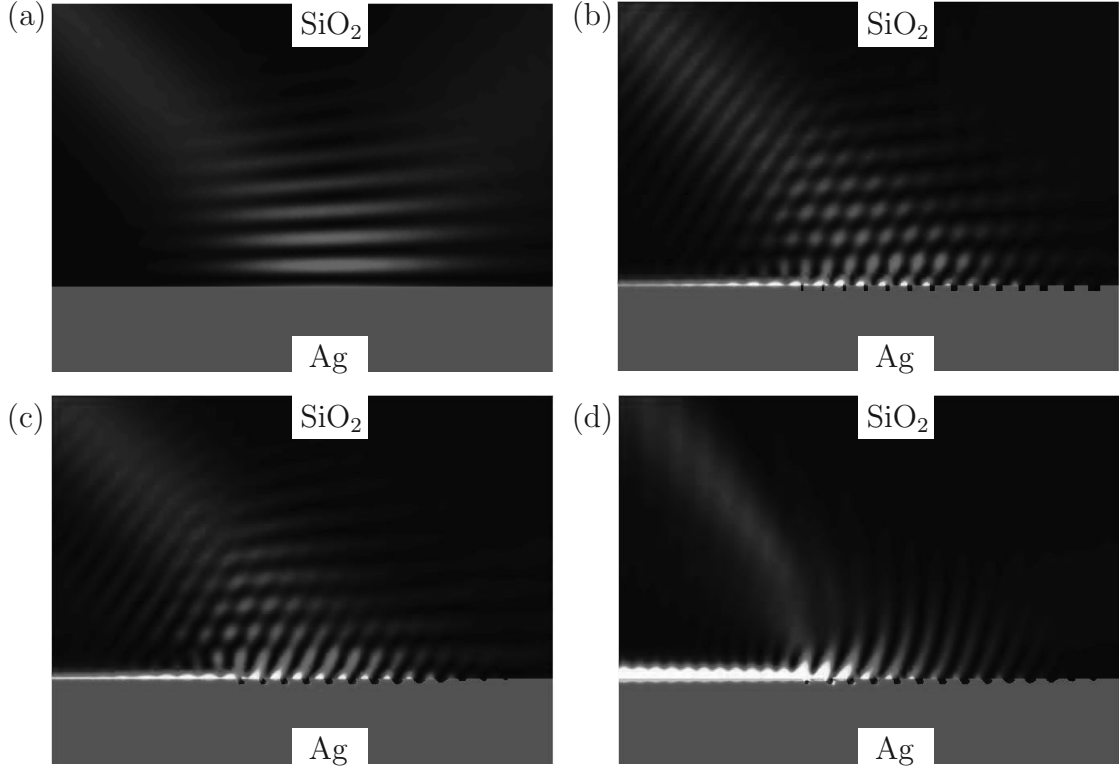


Figure 6.4 Norms of the magnetic field generated by the optimized input (c) and output coupler (d). The surface plasmon polariton mode cannot be excited without any coupling mechanism(a). The grating coupler from Ref. [130] is shown in (b) as a reference design.

plasmon is excited at Γ_{in} with an exponentially shaped electromagnetic wave matching the skin depth. For both cases, the permittivities of SiO₂ and Ag corresponding to the given wavelength are $\epsilon_r = 2.25$ and $\epsilon_r = -7.06 - j0.27$, respectively, and the permeability is assumed to be $\mu_r = 1$ for both materials. We use an initial guess of pure silver in the design domain Ω_{des} , which is shown in figure 6.3(a) with length scales. The optimized designs for the input and output couplers obtained using the described methodology are presented in figures 6.3(b) and (c), respectively. For the purpose of comparison we have presented the grating coupler from [130] in figure 6.3(d).

The optimized design for the input coupler consists of 13 slanted grooves of increasing width and decreasing depth. The optimized design represents an efficiency of 68.7% which is approximately a factor of 0.4 higher than the efficiency of the grating coupler from [130]. The optimized design of the output coupler is very similar to the optimized design of the input coupler, but with an extra groove at the right side of the design domain. Figure 6.4 shows the magnetic field norm for a setup with smooth surface (a), the grating coupler from [130] (b), the optimized input coupler (c) and the optimized output coupler (d). A notable standing wave pattern

is seen for the smooth surface generated by the incident and the reflected wave. In contrast, for the input coupler a significant field enhancements are obtained at the metal-dielectric interface due to the SPPs being very localized to the surface of the metal. At the end we note that the optimized output coupler is indeed better than the reversed input coupler. Equal topologies for the two cases are not expected due to different loss mechanisms in the incoming and outgoing wave cases.

Chapter 7

Fresnel zone plate lens

The optimized output grating coupler presented in the preceding chapter manipulated a optical wave to propagate in a direction of 45° to the surface. The final design problem of this thesis concerns not only directing but also focusing of a propagating wave into a single focus or multiple foci. A device for focusing of electromagnetic energy works by means of either diffraction, refraction, reflection or any combinations of the three. Quite many devices can focus electromagnetic waves and in the problem covered here the spatial layout of half opaque Fresnel zone plate lenses is optimized such that the wave energy in one point or multiple points is maximized. The results presented here are examples of the findings given in [P6].

7.1 Fresnel zone plate lenses

Fresnel zone plates (FZP) lenses work by means of diffraction and constructive interference instead of refraction and reflection and can be divided into two types, half-opaque FZPs (also called Soret zone plate) and phase-correcting FZPs. The former type is built of alternating transparent and opaque concentric rings to block out alternating Fresnel zones, c.f. figure 7.2, whereas the latter type is constructed to correct phases in various zones by varying the dielectric constant or the depth of the profile. Here we focus our attention to the half opaque FZP.

Refractive optics cease to be effective (and thereby conventional lenses) for wavelengths shorter than the visible spectrum until the hard X-ray region[131], because solids in this spectrum are strongly absorbing. Half opaque FZPs on the other hand work well in this spectrum[132]. Further, FZPs are in general desirable as focusing devices due to their simplicity of design, easy fabrication and low cost. However, a disadvantage of the half-opaque FZP lens type is that approximately half the energy of the incident wave is lost, due to the opaque zones, resulting in low aperture efficiency. This shortcoming can to some extent be remedied by combining several zone plate structures as a layered FZP[133] or by using a reflector based FZP[18]. A simple closed form design rule for FZPs when the incident wave is normal to the aperture can be derived for ray optics[134]. Constructive interference at the focus are obtained when the zones switch from opaque to transparent at radii where

$$r_n = \sqrt{\frac{2nF\lambda}{P} + \left(\frac{n\lambda}{P}\right)^2} \quad (7.1)$$

where r_n is the radius from the focal axis to the outer edge of the n 'th zone, n is the zone number, F is the focal length, λ is the wavelength of the incident wave and P is

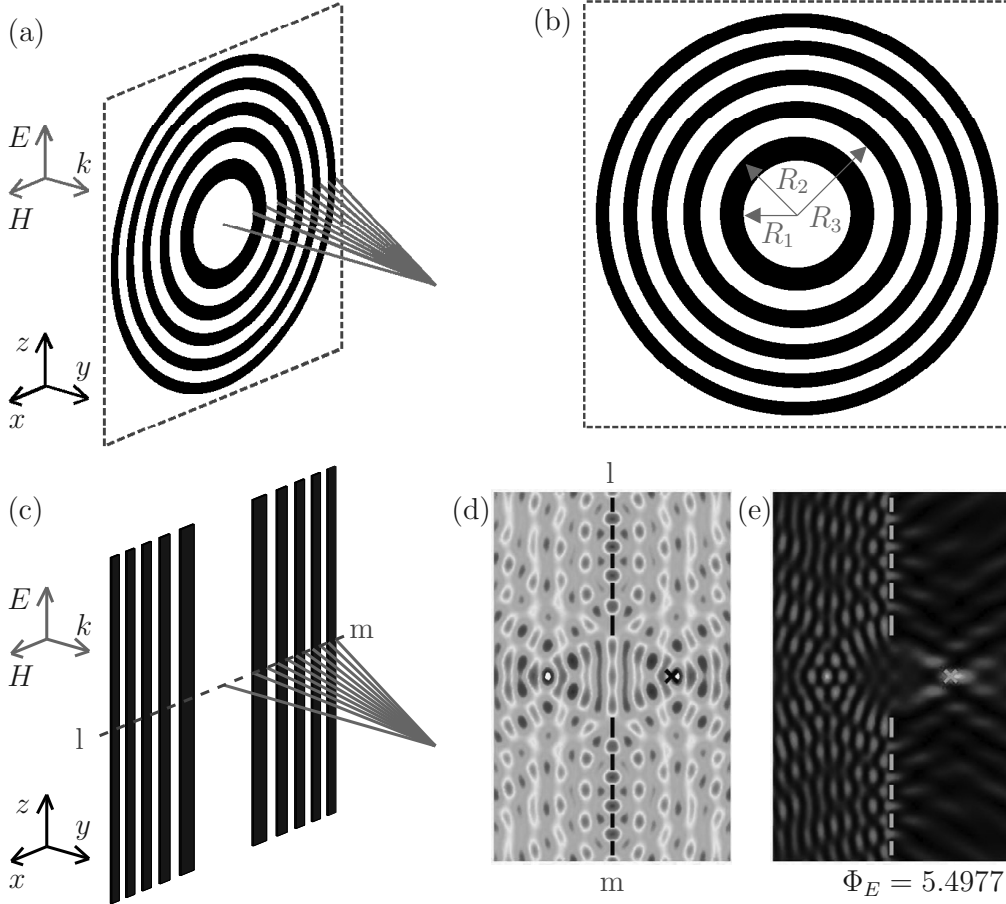


Figure 7.1 Half opaque Fresnel zone plate lens (a) focus an incident plane wave in a single point. The black regions corresponds to opaque rings and their placement (b) can be derived using ray optics, c.f. equation (7.1). The geometry of a planar zone plate (c) is invariant in one dimension. The total field and field norm for a planar zone plate with dimensions derived by equation (7.1) are shown in panels (d) and (e), respectively.

the number of phase corrections ($P = 2$ for a half-opaque FZP). However, equation (7.1) is known not to be optimal. A simple correction such as compressing the zone plate radially using a scalar coefficient k less than unity $r_n^{new} = k r_n$ results in a more efficient design[18]. Furthermore, several design methodologies have been developed to give the FZP special features such as dual-band FZPs[135], bifocal FZPs[136] and non-planar shaped FZPs[18]. Furthermore, the spatial distribution of either opaque material (for half-opaque FZPs) or dielectric material (for phase-correcting FZPs) calls for an optimization technique and several optimization methodologies have been reported[137, 138, 139] using search algorithms in the two first cited references and a genetic algorithm in the latter. In this study we employ the topology optimization method to find the spatial placement of opaque material for planar Fresnel zone plates.

7.2 Method

The geometry of a planar zone plate is invariant in one dimension as shown in figure 7.2(c). The computational domain can thereby be formulated in a plane perpendicular to the zone plate for efficient computation of the out-of-plane mode for either an E_z or H_z polarized plane wave. The infinite domain is truncated by perfectly matched layers backed up by a first order absorbing boundary condition[8]. We employ topology optimization in the standard density based approach. In the previous studies material is redistributed in a domain. In contrast, here the idea is to continuously vary, between full transmission and opacity in each boundary element at a specified design boundary. To do so, the design boundary Γ_{des} is modeled by a transition boundary condition[140] for an E_z or H_z polarized wave, which respectively can be formulated as

$$\eta \mathbf{n} \times (\mathbf{H}_1 - \mathbf{H}_2) + E_z = 0 \quad E_z\text{-polarization} \quad (7.2)$$

$$\eta \mathbf{n} \times (\mathbf{E}_1 - \mathbf{E}_2) + \mathbf{n} \times \mathbf{E}_1 = 0 \quad H_z\text{-polarization} \quad (7.3)$$

where η is the surface impedance. The transition boundary condition models a thin layer of conducting, non-magnetic material. When $\eta \rightarrow \infty$ equation 7.2 and 7.3 mimic full transmission and when $\eta = 0$ equation 7.2 and 7.3 is equivalent to the PEC condition (opaque). This property of the transition boundary condition can be exploited in the topology optimization approach using the surface impedance in the material interpolation. A design variable, $\gamma_e \in [0; 1]$, for each boundary element is introduced in order to interpolate between opacity and full transmission mimicked by $\eta^{\min} = 10^{-2}$ and $\eta^{\max} = 10^6$, respectively. A power interpolation function[33] is used, due to the big difference in orders of magnitude.

$$\eta_e(\gamma_e) = \eta^{\max} \left(\frac{\eta^{\min}}{\eta^{\max}} \right)^{\gamma_e} \quad (7.4)$$

In order to focus electromagnetic radiation, the objective is to maximize the norm of the total field at the specified foci points. The resulting optimization problem is formulated as

$$\max_{\gamma} \quad \Phi = \sum_{k=1}^n \frac{1}{W_k} |E_z(\mathbf{r}_k)|^2 \quad \text{objective function} \quad (7.5)$$

$$\text{subjected to} \quad \frac{1}{\int_{\Gamma_{\text{des}}} d\mathbf{r}} \int_{\Gamma_{\text{des}}} \gamma(\mathbf{r}) d\mathbf{r} - V_{\text{max}} \leq 0 \quad \text{volume constraint} \quad (7.6)$$

$$0 \leq \gamma(\mathbf{r}) \leq 1 \quad \forall \mathbf{r} \in \Gamma_{\text{des}} \quad \text{design variable bounds} \quad (7.7)$$

where n is the number of foci points and W_k is the field norm at the k 'th focal point when no FZP is present.

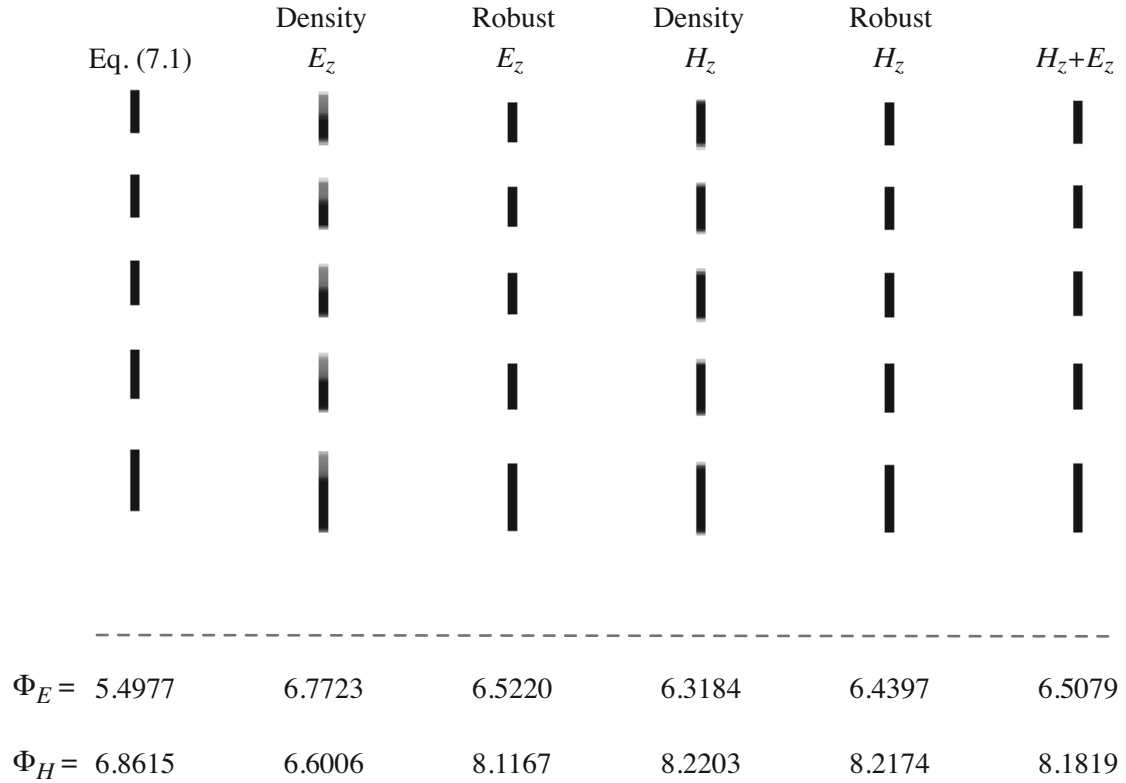


Figure 7.2 Half opaque Fresnel zone plate designs at 2.75 GHz with a focal length $F = 0.25$ m. The dashed red line shows the position of the optical axis around which the zone plates are symmetric; hence only the upper parts of the zone plates are shown. The filter technique and target polarization are written above the designs. The optimized Fresnel zone plates performance significantly better than the analytic design derived from equation (7.1).

7.3 Results

Initially, a one layered half opaque zone plate is studied, and optimized designs as well as their performance are compared to a design derived by the analytic expression in equation (7.1). The target frequency is chosen to be 2.75 GHz and the focal length to $F = 0.25$ m. The height of the design boundary is set to 1.5 m, i.e. 0.75 m on each side of the optical axis. The optimized designs along with the analytic reference zone plate are presented in figure 7.2. Two different filtering techniques are used, the density filter and the deterministic robust formulation. The former allow grayscale to occur whereas discrete designs can be obtained by the latter. The zone plates obtained with the density filter have a higher ability to focus the wave with the polarization for which they are optimized than their discrete counter-parts. However, especially in the case of the density filtered zone plate for E_z -polarization significant gray-scale appear on the side of plates pointing away from the optical axis. The intermediate densities may at first be interpreted as imperfect conducting

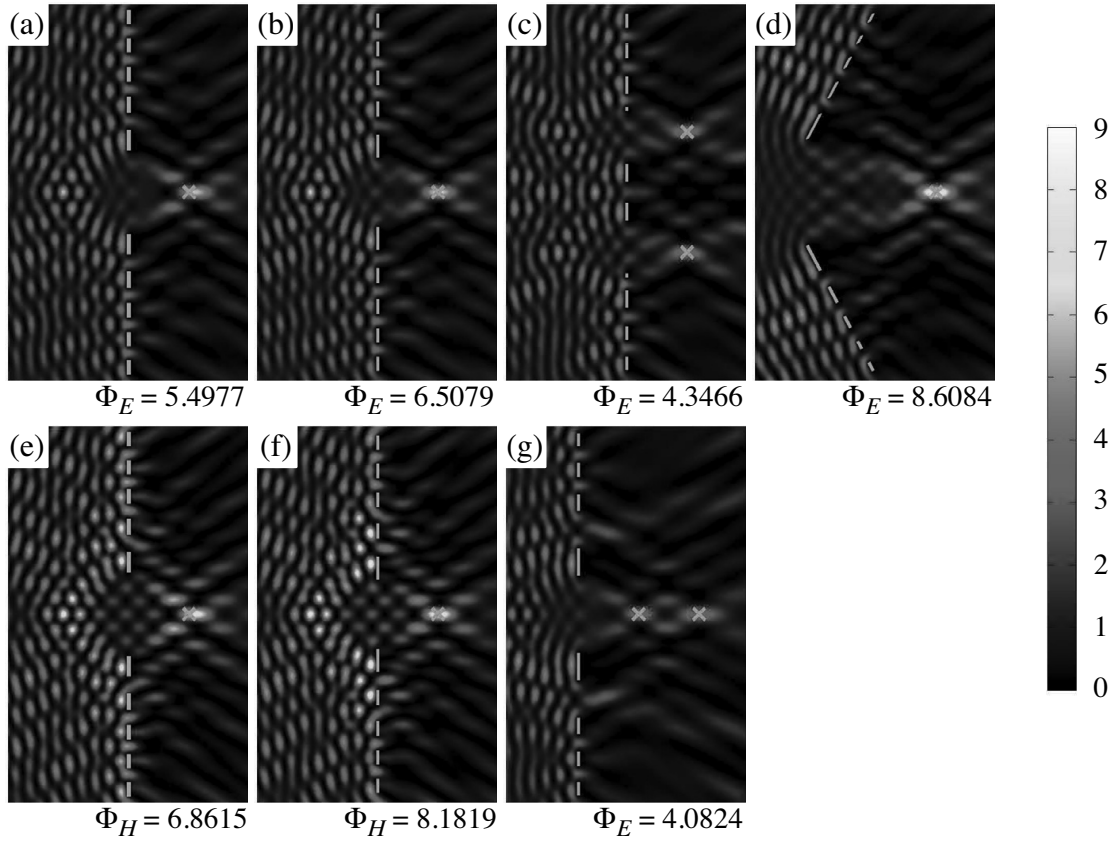


Figure 7.3 Field norms, zone plate designs (represented by the green lines) and the associated objective values. The topology optimized, polarization independent, zone plate (panels (b) and (f)) yield higher focusing performance compared to zone plates (panels (a) and (e)) designed by the traditional simple design rule for both E_z and H_z polarization. Bifocal design with foci on a vertical (c) and horizontal axis (g) can be obtained on the cost of the focusing intensity. A convex-shaped zone plate (d) performs better than the planar.

material. However, in [141] a similar study in 3D shows that the optimized design of circular Fresnel zone plates have "shark teeth" which points away from the optical axis for the E_z polarization. The intermediate densities in the planar case effectively mimic this "shark teeth" topology of the optimized 3D zone plates. It is worth to note that the discrete designs perform well for both polarizations even though they are only optimized for one polarization. A natural extension is to optimize for both polarizations simultaneously and the resulting design does not differ significantly from the two other discrete designs. It is worth to mention that all zone plates are compressed radially compared to the analytic design. This is in accordance with the findings from [18].

The field norms for the analytic reference design and the topology optimized zone plate that is optimized for both E_z and H_z polarization, are shown in figure

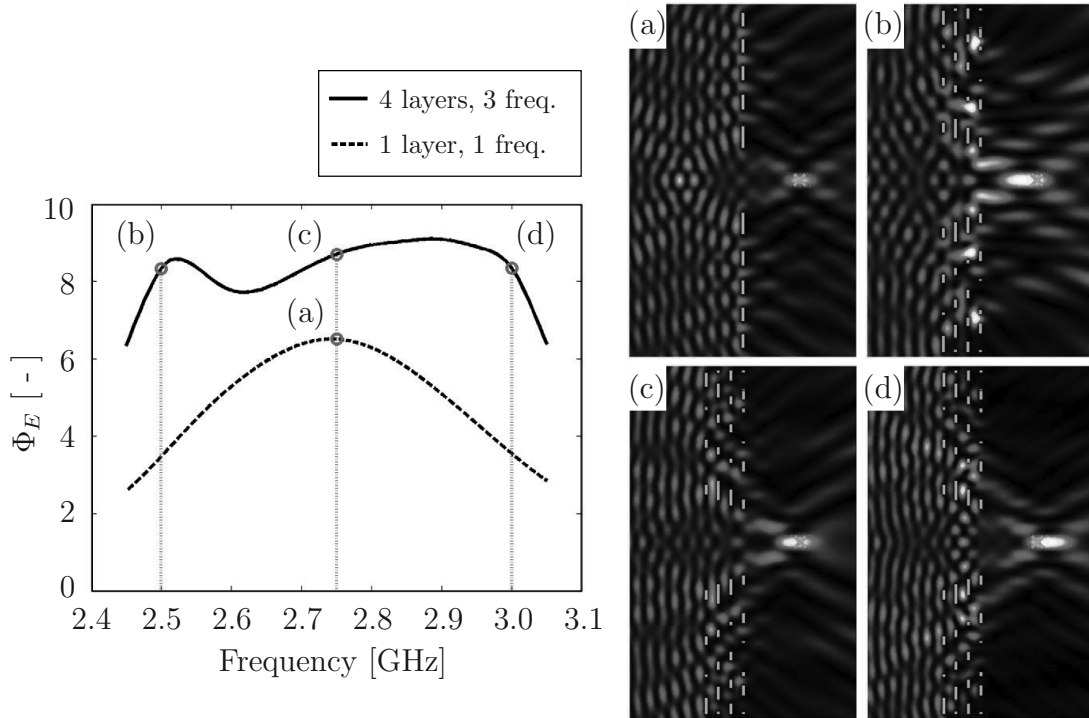


Figure 7.4 Frequency sweep for a single layered (dashed line) and 4 layered zone plate (solid line) illuminated by an E_z polarized plane wave. The focusing performance are improved significantly using a min/max formulation for three target frequencies at 2.5 GHz (b), 2.75 GHz (c) and 3.0 GHz (d) compared to the single layered zone plate (a), which is optimized for a single frequency.

7.3. The polarization independent zone plate ($E_z + H_z$ in figure 7.2) designed by topology optimization yields higher focusing performance compared to the analytic reference zone plate designed by the design rule from equation (7.1).

The outlined design methodology can handle a broad spectrum of design features. As examples two bifocal zone plates with foci on a vertical or horizontal axis are likewise shown in figures 7.3(c) and (g), respectively. However, the bifocal properties are obtained at the cost of focusing intensity. The methodology can also handle complex shaped design boundaries, e.g. a convex-shaped design (figure 7.3(d)).

A frequency sweep, c.f. figure 7.4, reveals that the focusing performance of the one layered zone plate illuminated by an E_z polarized wave somewhat deteriorates for other frequencies than the target frequencies. A broad banded effect is obtained for 4 layered zone plate with a min/max formulation for three target frequencies (2.5 GHz, 2.75 GHz and 3.0 GHz). A distance of half the wavelength separates each layer in the zone plate. The focusing performances are on the same level for the three target frequencies and approximately 2.5 times higher than the single layered zone plate at 2.5 GHz and 3.0 GHz.

Chapter 8

Concluding remarks

This thesis presents the study of wave manipulation of acoustic and electromagnetic waves by topology optimization. A method of designing acoustic or electromagnetic cloaks that can be realized with readily available materials is outlined. The material layout of the cloaks is determined by topology optimization such that the scattered field is minimized in all directions or a specified angular range. The evolution of topology optimized electromagnetic cloaks operating at various degrees of symmetry is presented. The analysis reveals that near perfect cloaking can be achieved in a limited frequency range when the cloaks are operating at up to 4 symmetric angles of incidence. The working principle for the cloak is to delay the waves in regions of higher permittivity than the background and subsequently phase match them to the waves outside. For an H_z -polarized wave, the optimized designs can take advantage of the surface mode at the PEC boundary, and achieve less scattering than the optimized designs for the E_z -polarized wave. Even a directional all-dielectric low-contrast cloaks that achieve good cloaking performance for both E_z and H_z polarization can be designed with this method. Further findings indicate, perhaps contrary to simple intuition, that fully enclosed, all-dielectric cloaks can not be designed effectively when distributing a material with lower permittivity than the background material. Directional acoustic cloaks can also be designed using the topology optimization method. Aluminum cylinders constitute the design and their placement and size is optimized such that their combined scattering pattern cancel the scattering from a big cylinder.

It is also shown that the backscattering from a PEC cylinder illuminated by a plane wave can be minimized by wrapping the cylinder in a cloak composed of annular rings made of non-absorbing, low-contrast, dielectric material readily available in nature. The layered Bragg-like structure amplifies and couples the field into confined ring-modes, which lead the wave around the cylinder hence reducing backscattering. Cloaking performance can be improved by increasing the number of rings wrapped around the PEC cylinder, increasing the permittivity of the high index material and/or relaxing the requirement to the size of the angle interval defining backscattering.

The topology optimization method is further employed in optimizing grating couplers for efficient in and out-coupling of electromagnetic surface waves at a metal-dielectric interface. Results indicate that efficiencies beyond 68% are possible for slanted groove-based gratings. The designs presented here are shown as specific solutions; however, the general concept of the improved efficiency by slanted grooves may inspire future realizations of efficient grating couplers.

Finally, a topology optimization based design methodology for improved energy

focusing from planar half opaque Fresnel zone plate lenses is outlined in this thesis. The transition boundary condition can model full transmission or opacity at a specified design boundary depending on the surface impedance. This property is exploited by varying the surface impedance in each boundary element for improved energy focusing. The topology optimized zone plates yield higher focusing performance compared to zone plates designed by the traditional simple design rule derived for ray optics. Furthermore, the outlined design methodology can handle a broad spectrum of design features such as multiple layers, bifocal properties, broad banded designs etc. in one combined approach.

8.1 Future work

The work summarized in this thesis can be extended in several ways in future studies. The list below contains the most important directions in which future research should be directed towards

- Realize the optimized cloak designs. Specially a realization of the annular ring design constituting the backscattering cloak seems attainable.
- Examine the possibilities for a near omnidirectional acoustic cloak based on aluminum cylinders.
- Extend all implementations to include Padé approximation such that the different devices can be optimized over larger frequency ranges.
- An equivalent study for minimizing backscattering can be performed for a sphere instead of a cylinder.
- Extend the idea of using the transition boundary condition to 3D designs. Optimized microstrip patch antennas could perhaps be designed using this idea.

References

- [1] F. Fahy, *Foundations of engineering acoustics*. Academic, 2001.
- [2] C. Balanis, *Advanced engineering electromagnetics*. Wiley, 1989.
- [3] L. Kelders, J. F. Allard, and W. Lauriks, “Ultrasonic surface waves above rectangular-groove gratings,” *The Journal of the Acoustical Society of America*, vol. 103, no. 5, pp. 2730–2733, 1998.
- [4] J. C. Maxwell, *A treatise on Electricity and Magnetism*. Oxford, Clarendon Press, 1873.
- [5] D. Cheng, *Field and wave electromagnetics*. Addison-Wesley, 1989.
- [6] M. B. Dühring, J. S. Jensen, and O. Sigmund, “Acoustic design by topology optimization,” *Journal of Sound and Vibration*, vol. 317, no. 35, pp. 557 – 575, 2008.
- [7] O. Sigmund and J. S. Jensen, “Systematic design of phononic bandgap materials and structures by topology optimization,” *Philosophical Transactions of the Royal Society of London. Series A: Mathematical, Physical and Engineering Sciences*, vol. 361, no. 1806, pp. 1001–1019, 2003.
- [8] J. Jin, *The finite element method in electromagnetics*. A Wiley-Interscience publication, Wiley, 2002.
- [9] M. Koshihara, Y. Tsuji, and S. Sasaki, “High-performance absorbing boundary conditions for photonic crystal waveguide simulations,” *Microwave and Wireless Components Letters, IEEE*, vol. 11, pp. 152 –154, apr 2001.
- [10] A. Taflov and S. Hagness, *Computational electrodynamics: the finite-difference time-domain method*. Artech House antennas and propagation library, Artech House, 2005.
- [11] J. Hesthaven and T. Warburton, *Nodal discontinuous Galerkin methods: algorithms, analysis, and applications*. Texts in applied mathematics, Springer, 2008.
- [12] J. Jin and D. Riley, *Finite element analysis of antennas and arrays*. John Wiley & Sons, 2009.
- [13] Comsol Multiphysics, COMSOL AB, Stockholm, www.comsol.se.

- [14] L. H. Olesen, F. Okkels, and H. Bruus, “A high-level programming-language implementation of topology optimization applied to steady-state navierstokes flow,” *International Journal for Numerical Methods in Engineering*, vol. 65, no. 7, pp. 975–1001, 2006.
- [15] B. Saleh and M. Teich, *Fundamentals of photonics*. Wiley series in pure and applied optics, Wiley-Interscience, 2007.
- [16] J. Pendry, “Taking the wraps off cloaking,” *Physics*, vol. 2, p. 95, Nov 2009.
- [17] H. Hristov, *Fresnel zones in wireless links, zone plate lenses and antennas*. Artech House antennas and propagation library, Artech House, 2000.
- [18] O. Minin and I. Minin, *Diffractional optics of millimetre waves*. IOP, London, 2004.
- [19] M. P. Bendsøe and N. Kikuchi, “Generating optimal topologies in structural design using a homogenization method,” *Computer Methods in Applied Mechanics and Engineering*, vol. 71, no. 2, pp. 197 – 224, 1988.
- [20] O. Sigmund and S. Torquato, “Composites with extremal thermal expansion coefficients,” *Applied Physics Letters*, vol. 69, no. 21, pp. 3203–3205, 1996.
- [21] T. Borrvall and J. Petersson, “Topology optimization of fluids in stokes flow,” *International Journal for Numerical Methods in Fluids*, vol. 41, no. 1, pp. 77–107, 2003.
- [22] O. Sigmund, “Design of multiphysics actuators using topology optimization - part i: One-material structures,” *Computer Methods in Applied Mechanics and Engineering*, vol. 190, no. 4950, pp. 6577 – 6604, 2001.
- [23] O. Sigmund, “Design of multiphysics actuators using topology optimization - part ii: Two-material structures,” *Computer Methods in Applied Mechanics and Engineering*, vol. 190, no. 4950, pp. 6605 – 6627, 2001.
- [24] J. S. Jensen and O. Sigmund, “Systematic design of photonic crystal structures using topology optimization: Low-loss waveguide bends,” *Appl. Phys. Lett.*, vol. 84, no. 12, pp. 2022–2024, 2004.
- [25] P. Borel, A. Harpøth, L. Frandsen, M. Kristensen, P. Shi, J. Jensen, and O. Sigmund, “Topology optimization and fabrication of photonic crystal structures,” *Opt. Express*, vol. 12, pp. 1996–2001, May 2004.
- [26] O. Sigmund, “A 99 line topology optimization code written in matlab,” *Structural and Multidisciplinary Optimization*, vol. 21, pp. 120–127, 2001. 10.1007/s001580050176.

- [27] E. Andreassen, A. Clausen, M. Schevenels, B. Lazarov, and O. Sigmund, “Efficient topology optimization in matlab using 88 lines of code,” *Structural and Multidisciplinary Optimization*, vol. 43, pp. 1–16, 2011. 10.1007/s00158-010-0594-7.
- [28] M. P. Bendsøe and O. Sigmund, *Topology optimization, theory, methods and applications*. Berlin: Springer, 2003.
- [29] S. J. Cox and D. C. Dobson, “Maximizing band gaps in two-dimensional photonic crystals,” *SIAM Journal on Applied Mathematics*, vol. 59, pp. 2108–2120, Aug. 1999.
- [30] S. J. Cox and D. C. Dobson, “Band structure optimization of two-dimensional photonic crystals in h-polarization,” *Journal of Computational Physics*, vol. 158, no. 2, pp. 214 – 224, 2000.
- [31] J. S. Jensen and O. Sigmund, “Topology optimization of photonic crystal structures: a high-bandwidth low-loss t-junction waveguide,” *J. Opt. Soc. Am. B*, vol. 22, pp. 1191–1198, Jun 2005.
- [32] P. Borel, L. Frandsen, A. Harpoth, M. Kristensen, J. Jensen, and O. Sigmund, “Topology optimised broadband photonic crystal y-splitter,” *Electronics Letters DOI - 10.1049/el:20057717*, vol. 41, no. 2, pp. 69–71, 2005.
- [33] G. Kiziltas, D. Psychoudakis, J. Volakis, and N. Kikuchi, “Topology design optimization of dielectric substrates for bandwidth improvement of a patch antenna,” *Antennas and Propagation, IEEE Transactions on DOI - 10.1109/TAP.2003.817539*, vol. 51, no. 10, pp. 2732–2743, 2003.
- [34] G. Kiziltas, N. Kikuchi, J. Volakis, and J. Halloran, “Topology optimization of dielectric substrates for filters and antennas using simp,” *Archives of Computational Methods in Engineering*, vol. 11, pp. 355–388, 2004. 10.1007/BF02736229.
- [35] T. Nomura, K. Sato, K. Taguchi, T. Kashiwa, and S. Nishiwaki, “Structural topology optimization for the design of broadband dielectric resonator antennas using the finite difference time domain technique,” *International Journal for Numerical Methods in Engineering*, vol. 71, no. 11, pp. 1261–1296, 2007.
- [36] A. Erentok and O. Sigmund, “Topology optimization of sub-wavelength antennas,” *Antennas and Propagation, IEEE Transactions on DOI - 10.1109/TAP.2010.2090451*, vol. 59, no. 1, pp. 58–69, 2011.
- [37] N. Aage, N. A. Mortensen, and O. Sigmund, “Topology optimization of metallic devices for microwave applications,” *International Journal for Numerical Methods in Engineering*, vol. 83, no. 2, pp. 228–248, 2010.

- [38] L. Yang, A. Lavrinenko, L. Frandsen, P. Borel, A. Tetu, and J. Fage-Pedersen, “Topology optimisation of slow light coupling to photonic crystal waveguides,” *Electronics Letters*, vol. 43, pp. 923–924, 16 2007.
- [39] R. Matzen, J. Jensen, and O. Sigmund, “Transient topology optimization of two-dimensional elastic wave propagation,” in *Ninth International Conference on Computational Structures Technology*, 2008.
- [40] R. Matzen, J. S. Jensen, and O. Sigmund, “Topology optimization for transient response of photonic crystal structures,” *J. Opt. Soc. Am. B*, vol. 27, pp. 2040–2050, Oct 2010.
- [41] J. Dahl, J. Jensen, and O. Sigmund, “Topology optimization for transient wave propagation problems in one dimension,” *Structural and Multidisciplinary Optimization*, vol. 36, pp. 585–595, 2008. 10.1007/s00158-007-0192-5.
- [42] L. Yang, A. V. Lavrinenko, J. M. Hvam, and O. Sigmund, “Design of one-dimensional optical pulse-shaping filters by time-domain topology optimization,” *Applied Physics Letters*, vol. 95, no. 26, p. 261101, 2009.
- [43] Y. Elesin, B. Lazarov, J. Jensen, and O. Sigmund, “Design of robust and efficient photonic switches using topology optimization,” *Photonics and Nanostructures - Fundamentals and Applications*, no. 0, 2011.
- [44] B. Lazarov, R. Matzen, and Y. Elesin, “Topology optimization of pulse shaping filters using the hilbert transform envelope extraction,” *Structural and Multidisciplinary Optimization*, vol. 44, pp. 409–419, 2011. 10.1007/s00158-011-0642-y.
- [45] J. Jensen and O. Sigmund, “Topology optimization for nano-photonics,” *Laser & Photonics Reviews*, vol. 5, no. 2, pp. 308–321, 2011.
- [46] O. Sigmund and J. Jensen, “Design of acoustic devices by topology optimization,” in *5th World Congress on Structural and Multidisciplinary Optimization WCSMO5*, pp. 267–268., 2003.
- [47] E. Wadbro and M. Berggren, “Topology optimization of an acoustic horn,” *Computer Methods in Applied Mechanics and Engineering*, vol. 196, no. 13, pp. 420 – 436, 2006.
- [48] G. H. Yoon, J. S. Jensen, and O. Sigmund, “Topology optimization of acoustic structure interaction problems using a mixed finite element formulation,” *International Journal for Numerical Methods in Engineering*, vol. 70, no. 9, pp. 1049–1075, 2007.

- [49] M. P. Bendsøe, “Optimal shape design as a material distribution problem,” *Structural and Multidisciplinary Optimization*, vol. 1, pp. 193–202, 1989. 10.1007/BF01650949.
- [50] A. Saxena, “A material-mask overlay strategy for continuum topology optimization of compliant mechanisms using honeycomb discretization,” *Journal of Mechanical Design*, vol. 130, no. 8, p. 082304, 2008.
- [51] C. Jain and A. Saxena, “An improved material-mask overlay strategy for topology optimization of structures and compliant mechanisms,” *Journal of Mechanical Design*, vol. 132, no. 6, p. 061006, 2010.
- [52] J. K. Guest, “A projection-based topology optimization approach to distributing discrete features in structures and materials,” in *9th World Congress on Structural and Multidisciplinary Optimization*, 2011.
- [53] K. Svanberg, “The method of moving asymptotes—a new method for structural optimization,” *International Journal for Numerical Methods in Engineering*, vol. 24, no. 2, pp. 359–373, 1987.
- [54] T. E. Bruns and D. A. Tortorelli, “Topology optimization of non-linear elastic structures and compliant mechanisms,” *Computer Methods in Applied Mechanics and Engineering*, vol. 190, no. 26–27, pp. 3443 – 3459, 2001.
- [55] B. Bourdin, “Filters in topology optimization,” *International Journal for Numerical Methods in Engineering*, vol. 50, no. 9, pp. 2143–2158, 2001.
- [56] F. Wang, B. Lazarov, and O. Sigmund, “On projection methods, convergence and robust formulations in topology optimization,” *Structural and Multidisciplinary Optimization*, vol. 43, pp. 767–784, 2011. 10.1007/s00158-010-0602-y.
- [57] O. Sigmund, “Morphology-based black and white filters for topology optimization,” *Structural and Multidisciplinary Optimization*, vol. 33, pp. 401–424, 2007. 10.1007/s00158-006-0087-x.
- [58] B. S. Lazarov and O. Sigmund, “Filters in topology optimization based on helmholtz-type differential equations,” *International Journal for Numerical Methods in Engineering*, vol. 86, no. 6, pp. 765–781, 2011.
- [59] A. Kawamoto, T. Matsumori, S. Yamasaki, T. Nomura, T. Kondoh, and S. Nishiwaki, “Heaviside projection based topology optimization by a pde-filtered scalar function,” *Structural and Multidisciplinary Optimization*, vol. 44, pp. 19–24, 2011. 10.1007/s00158-010-0562-2.
- [60] B. S. Lazarov, M. Schevenels, and O. Sigmund, “Robust design of large-displacement compliant mechanisms,” *Mechanical Sciences*, vol. 2, pp. 175–182, 2011.

- [61] J. K. Guest, J. H. Prvost, and T. Belytschko, "Achieving minimum length scale in topology optimization using nodal design variables and projection functions," *International Journal for Numerical Methods in Engineering*, vol. 61, no. 2, pp. 238–254, 2004.
- [62] J. K. Guest, "Topology optimization with multiple phase projection," *Computer Methods in Applied Mechanics and Engineering*, vol. 199, no. 1-4, pp. 123 – 135, 2009.
- [63] S. Xu, Y. Cai, and G. Cheng, "Volume preserving nonlinear density filter based on heaviside functions," *Structural and Multidisciplinary Optimization*, vol. 41, pp. 495–505, 2010. 10.1007/s00158-009-0452-7.
- [64] U. Leonhardt, "Optical conformal mapping," *Science*, vol. 312, no. 5781, pp. 1777–1780, 2006.
- [65] J. B. Pendry, D. Schurig, and D. R. Smith, "Controlling electromagnetic fields," *Science*, vol. 312, no. 5781, pp. 1780–1782, 2006.
- [66] M. Lax and D. F. Nelson, "Maxwell equations in material form," *Phys. Rev. B*, vol. 13, pp. 1777–1784, Feb 1976.
- [67] S. A. Cummer, B.-I. Popa, D. Schurig, D. R. Smith, and J. Pendry, "Full-wave simulations of electromagnetic cloaking structures," *Phys. Rev. E*, vol. 74, p. 036621, Sep 2006.
- [68] Y. Lai, H. Chen, Z.-Q. Zhang, and C. T. Chan, "Complementary media invisibility cloak that cloaks objects at a distance outside the cloaking shell," *Phys. Rev. Lett.*, vol. 102, p. 093901, Mar 2009.
- [69] T. Philbin, "Cloaking at a distance," *Physics*, vol. 2, p. 17, Mar 2009.
- [70] Y. Lai, J. Ng, H. Chen, D. Han, J. Xiao, Z.-Q. Zhang, and C. T. Chan, "Illusion optics: The optical transformation of an object into another object," *Phys. Rev. Lett.*, vol. 102, p. 253902, Jun 2009.
- [71] V. G. Veselago, "The electrodynamics of substances with simultaneously negative values of ϵ and μ ," *Physics-Uspokhi*, vol. 10, no. 4, pp. 509–514, 1968.
- [72] J. B. Pendry, A. J. Holden, W. J. Stewart, and I. Youngs, "Extremely low frequency plasmons in metallic mesostructures," *Phys. Rev. Lett.*, vol. 76, pp. 4773–4776, Jun 1996.
- [73] J. Pendry, A. Holden, D. Robbins, and W. Stewart, "Magnetism from conductors and enhanced nonlinear phenomena," *Microwave Theory and Techniques, IEEE Transactions on*, vol. 47, pp. 2075 –2084, nov 1999.

- [74] R. A. Shelby, D. R. Smith, and S. Schultz, “Experimental verification of a negative index of refraction,” *Science*, vol. 292, no. 5514, pp. 77–79, 2001.
- [75] D. Schurig, J. J. Mock, B. J. Justice, S. A. Cummer, J. B. Pendry, A. F. Starr, and D. R. Smith, “Metamaterial electromagnetic cloak at microwave frequencies,” *Science*, vol. 314, no. 5801, pp. 977–980, 2006.
- [76] U. Larsen, O. Signund, and S. Bouwsta, “Design and fabrication of compliant micromechanisms and structures with negative poisson’s ratio,” *Microelectromechanical Systems, Journal of*, vol. 6, pp. 99–106, jun 1997.
- [77] N. A. Mortensen, M. Yan, O. Sigmund, and O. Breinbjerg, “On the unambiguous determination of effective optical properties of periodic metamaterials: a one-dimensional case study,” *J. Europ. Opt. Soc. Rap. Public.*, vol. 5, p. 10010, 2010.
- [78] D. R. Smith, D. C. Vier, T. Koschny, and C. M. Soukoulis, “Electromagnetic parameter retrieval from inhomogeneous metamaterials,” *Phys. Rev. E*, vol. 71, p. 036617, Mar 2005.
- [79] C. Rockstuhl, T. Paul, F. Lederer, T. Pertsch, T. Zentgraf, T. P. Meyrath, and H. Giessen, “Transition from thin-film to bulk properties of metamaterials,” *Phys. Rev. B*, vol. 77, pp. 035126–, Jan. 2008.
- [80] A. Andryieuski, R. Malureanu, and A. Lavrinenko, “Wave propagation retrieval method for metamaterials: Unambiguous restoration of effective parameters,” *Phys. Rev. B*, vol. 80, p. 193101, 2009.
- [81] A. Pors, I. Tsukerman, and S. I. Bozhevolnyi, “Effective constitutive parameters of plasmonic metamaterials: Homogenization by dual field interpolation,” *Phys. Rev. E*, vol. 84, p. 016609, July 2011.
- [82] A. Diaz and O. Sigmund, “A topology optimization method for design of negative permeability metamaterials,” *Structural and Multidisciplinary Optimization*, vol. 41, pp. 163–177, 2010. 10.1007/s00158-009-0416-y.
- [83] J. Li and J. B. Pendry, “Hiding under the carpet: A new strategy for cloaking,” *Phys. Rev. Lett.*, vol. 101, p. 203901, Nov 2008.
- [84] J. Valentine, J. Li, T. Zentgraf, G. Bartal, and X. Zhang, “An optical cloak made of dielectrics,” *Nat Mater*, vol. 8, pp. 568–571, 07 2009.
- [85] T. Ergin, N. Stenger, P. Brenner, J. B. Pendry, and M. Wegener, “Three-dimensional invisibility cloak at optical wavelengths,” *Science*, vol. 328, no. 5976, pp. 337–339, 2010.

- [86] X. Chen, Y. Luo, J. Zhang, K. Jiang, J. B. Pendry, and S. Zhang, “Macroscopic invisibility cloaking of visible light,” *Nat Commun*, vol. 2, p. 176, 02 2011.
- [87] J. Zhang, L. Liu, Y. Luo, S. Zhang, and N. A. Mortensen, “Homogeneous optical cloak constructed with uniform layered structures,” *Opt. Express*, vol. 19, pp. 8625–8631, Apr 2011.
- [88] R. K. Taylor, F. Seifrt, O. Zhuromskyy, U. Peschel, G. Leugering, and W. Peukert, “Painting by numbers: Nanoparticle-based colorants in the post-empirical age,” *Advanced Materials*, vol. 23, no. 22-23, pp. 2554–2570, 2011.
- [89] J. D. Joannopoulos, S. G. Johnson, J. N. Winn, and R. D. Meade, *Photonic Crystals: Molding the Flow of Light*. Princeton University Press, second ed., February 2008.
- [90] M. Farhat, S. Guenneau, and S. Enoch, “Ultrabroadband elastic cloaking in thin plates,” *Phys. Rev. Lett.*, vol. 103, p. 024301, Jul 2009.
- [91] N. Stenger, M. Wilhelm, and M. Wegener, “Experiments on elastic cloaking in thin plates,” *Phys. Rev. Lett.*, vol. 108, p. 014301, Jan 2012.
- [92] J. Renger, M. Kadic, G. Dupont, S. S. Aćimović, S. Guenneau, R. Quidant, and S. Enoch, “Hidden progress: broadband plasmonic invisibility,” *Opt. Express*, vol. 18, pp. 15757–15768, Jul 2010.
- [93] S. Zhang, D. A. Genov, C. Sun, and X. Zhang, “Cloaking of matter waves,” *Phys. Rev. Lett.*, vol. 100, p. 123002, Mar 2008.
- [94] M. Farhat, S. Enoch, S. Guenneau, and A. B. Movchan, “Broadband cylindrical acoustic cloak for linear surface waves in a fluid,” *Phys. Rev. Lett.*, vol. 101, p. 134501, Sep 2008.
- [95] S. A. Cummer and D. Schurig, “One path to acoustic cloaking,” *New Journal of Physics*, vol. 9, no. 3, p. 45, 2007.
- [96] G. W. Milton, M. Briane, and J. R. Willis, “On cloaking for elasticity and physical equations with a transformation invariant form,” *New Journal of Physics*, vol. 8, no. 10, p. 248, 2006.
- [97] H. Chen and C. T. Chan, “Acoustic cloaking in three dimensions using acoustic metamaterials,” *Applied Physics Letters*, vol. 91, no. 18, p. 183518, 2007.
- [98] B.-I. Popa and S. A. Cummer, “Homogeneous and compact acoustic ground cloaks,” *Phys. Rev. B*, vol. 83, p. 224304, Jun 2011.
- [99] B.-I. Popa, L. Zigoneanu, and S. A. Cummer, “Experimental acoustic ground cloak in air,” *Phys. Rev. Lett.*, vol. 106, p. 253901, Jun 2011.

- [100] S. Zhang, C. Xia, and N. Fang, “Broadband acoustic cloak for ultrasound waves,” *Phys. Rev. Lett.*, vol. 106, p. 024301, Jan 2011.
- [101] J. B. Pendry and J. Li, “An acoustic metafluid: realizing a broadband acoustic cloak,” *New Journal of Physics*, vol. 10, no. 11, p. 115032, 2008.
- [102] B.-I. Popa and S. A. Cummer, “Design and characterization of broadband acoustic composite metamaterials,” *Phys. Rev. B*, vol. 80, p. 174303, Nov 2009.
- [103] D. Torrent and J. Sánchez-Dehesa, “Anisotropic mass density by radially periodic fluid structures,” *Phys. Rev. Lett.*, vol. 105, p. 174301, Oct 2010.
- [104] V. M. Garca-Chocano, L. Sanchis, A. Daz-Rubio, J. Martinez-Pastor, F. Cervera, R. Llopis-Pontiveros, and J. Snchez-Dehesa, “Acoustic cloak for airborne sound by inverse design,” *Appl. Phys. Lett.*, vol. 99, no. 7, p. 074102, 2011.
- [105] B.-I. Popa and S. A. Cummer, “Cloaking with optimized homogeneous anisotropic layers,” *Phys. Rev. A*, vol. 79, p. 023806, Feb 2009.
- [106] A. W. Adey, “Scattering of electromagnetic waves by coaxial cylinders,” *Can. J. Phys.*, vol. 34, pp. 510–520, May 1956.
- [107] C. C. H. Tang, “Backscattering from dielectric-coated infinite cylindrical obstacles,” *J. Appl. Phys.*, vol. 28, no. 5, pp. 628–633, 1957.
- [108] M. KERKER and E. MATIJEVIĆ, “Scattering of electromagnetic waves from concentric infinite cylinders,” *J. Opt. Soc. Am.*, vol. 51, pp. 506–508, May 1961.
- [109] J. Scheuer and A. Yariv, “Annular bragg defect mode resonators,” *J. Opt. Soc. Am. B*, vol. 20, pp. 2285–2291, Nov 2003.
- [110] M. A. Kaliteevski, R. A. Abram, V. V. Nikolaev, and G. S. Sokolovski, “Bragg reflectors for cylindrical waves,” *Journal of Modern Optics*, vol. 46, pp. 875–890, Apr. 1999.
- [111] R. Wood, “Xlii. on a remarkable case of uneven distribution of light in a diffraction grating spectrum,” *Philosophical Magazine Series 6*, vol. 4, pp. 396–402, Sept. 1902.
- [112] H. A. Atwater, “The promise of plasmonics,” *Sci. Am.*, vol. 296, pp. 56–63, Apr 2007.
- [113] T. W. Ebbesen, H. J. Lezec, H. F. Ghaemi, T. Thio, and P. A. Wolff, “Extraordinary optical transmission through sub-wavelength hole arrays,” *Nature*, vol. 391, pp. 667–669, Feb. 1998.

- [114] W. L. Barnes, A. Dereux, and T. W. Ebbesen, “Surface plasmon subwavelength optics,” *Nature*, vol. 424, pp. 824–830, Aug. 2003.
- [115] S. Bozhevolnyi, *Plasmonic Nanoguides and Circuits*. Pan Stanford Publishing, 2008.
- [116] V. E. Ferry, L. A. Sweatlock, D. Pacifici, and H. A. Atwater, “Plasmonic nanostructure design for efficient light coupling into solar cells,” *Nano Lett.*, vol. 8, pp. 4391–4397, Nov. 2008.
- [117] S. Maier, *Plasmonics: Fundamentals and Applications*. Springer, May 2007.
- [118] H. Raether, *Surface Plasmons on Smooth and Rough Surfaces and on Gratings*. Springer, 1988.
- [119] Y.-Y. Teng and E. A. Stern, “Plasma radiation from metal grating surfaces,” *Phys. Rev. Lett.*, vol. 19, pp. 511–514, Aug 1967.
- [120] A. Otto, “Excitation of nonradiative surface plasma waves in silver by the method of frustrated total reflection,” *Zeitschrift fr Physik A Hadrons and Nuclei*, vol. 216, pp. 398–410, 1968. 10.1007/BF01391532.
- [121] E. Kretschmann and H. Raether, “Radiative decay of non radiative surface plasmons excited by light,” *Z. Naturforsch.*, vol. 23a, pp. 2135–2136, 1968.
- [122] B. Hecht, H. Bielefeldt, L. Novotny, Y. Inouye, and D. W. Pohl, “Local excitation, scattering, and interference of surface plasmons,” *Phys. Rev. Lett.*, vol. 77, pp. 1889–1892, Aug 1996.
- [123] G. I. Stegeman, R. F. Wallis, and A. A. Maradudin, “Excitation of surface polaritons by end-fire coupling,” *Opt. Lett.*, vol. 8, pp. 386–388, July 1983.
- [124] R. Charbonneau, E. Lisicka-Shrzek, and P. Berini, “Broadside coupling to long-range surface plasmons using an angle-cleaved optical fiber,” *Applied Physics Letters*, vol. 92, no. 10, p. 101102, 2008.
- [125] T. Tamir and S. Peng, “Analysis and design of grating couplers,” *Applied Physics A: Materials Science & Processing*, vol. 14, pp. 235–254, 1977. 10.1007/BF00882729.
- [126] E. Moreno, D. Erni, C. Hafner, R. Kunz, and R. Vahldieck, “Modeling and optimization of non-periodic grating couplers,” *Optical and Quantum Electronics*, vol. 34, pp. 1051–1069, 2002. 10.1023/A:1021172003924.
- [127] D. P. Ceperley and A. R. Neureuther, “Engineering surface plasmon grating couplers through computer simulation,” in *J. Vac. Sci. Technol. B*, 2008.

- [128] C. Peng and W. Challener, "Input-grating couplers for narrow gaussian beam: influence of groove depth," *Opt. Express*, vol. 12, pp. 6481–6490, Dec 2004.
- [129] G. Leveque and O. J. F. Martin, "Optimization of finite diffraction gratings for the excitation of surface plasmons," *Journal of Applied Physics*, vol. 100, no. 12, p. 124301, 2006.
- [130] J. Lu, C. Petre, E. Yablonovitch, and J. Conway, "Numerical optimization of a grating coupler for the efficient excitation of surface plasmons at an ag-sio2 interface," *J. Opt. Soc. Am. B*, vol. 24, pp. 2268–2272, Sep 2007.
- [131] B. Lengeler, C. G. Schroer, M. Kuhlmann, B. Benner, T. F. Gnzler, O. Kurapova, F. Zontone, A. Snigirev, and I. Snigireva, "Refractive x-ray lenses," *Journal of Physics D: Applied Physics*, vol. 38, no. 10A, p. A218, 2005.
- [132] A. V. Baez, "A self-supporting metal fresnel zone-plate to focus extreme ultra-violet and soft x-rays," *Nature*, vol. 186, pp. 958–958, June 1960.
- [133] G. Z. Jiang and W. X. Zhang, "Theoretical and experimental studies of the fresnel zone plate lens antenna," *Electromagnetics*, vol. 19, pp. 385–399, July 1999.
- [134] J. C. Wiltse, "Zone plate designs for terahertz frequencies (invited paper)," vol. 5790, pp. 167–179, SPIE, 2005.
- [135] J. C. Wiltse, "Dual-band fresnel zone plate antennas," vol. 3062, pp. 181–185, SPIE, 1997.
- [136] W. D. Furlan, J. A. Monsoriu, and G. Saavedra, "Focusing properties of aperiodic zone plates," vol. 6317, p. 63171B, SPIE, 2006.
- [137] L. Baggen and M. Herben, "Design procedure for a fresnel-zone plate antenna," *International Journal of Infrared and Millimeter Waves*, vol. 14, pp. 1341–1352, June 1993.
- [138] P. Srisungsitthisunti, O. K. Ersoy, and X. Xu, "Laser direct writing of volume modified fresnel zone plates," *J. Opt. Soc. Am. B*, vol. 24, pp. 2090–2096, Sept. 2007.
- [139] D. Reid and G. Smith, "A full electromagnetic analysis for the soret and folded zone plate antennas," *Antennas and Propagation, IEEE Transactions*, vol. 54, no. 12, pp. 3638–3646, 2006.
- [140] T. Senior, J. Volakis, and I. of Electrical Engineers, *Approximate boundary conditions in electromagnetics*. IEE electromagnetic waves series, Institution of Electrical Engineers, 1995.

- [141] Aage, *Topology optimization of radio frequency and microwave structure*. PhD thesis, Technical University of Denmark, 2011.

Publication [P1]

Topology optimized low-contrast
all-dielectric optical cloak

Topology optimized low-contrast all-dielectric optical cloak

Jacob Andkjær^{a)} and Ole Sigmund

Department of Mechanical Engineering, Technical University of Denmark, 2800 Kgs. Lyngby, Denmark

(Received 13 August 2010; accepted 22 December 2010; published online 13 January 2011)

A systematic methodology for designing low-contrast all-dielectric cloaks operating in the optical range is presented. Topology optimization is used to find the layout of standard dielectric material that minimizes the norm of the scattered field in the surroundings of the cloak. Rotational symmetries are exploited to optimize for multiple angles based on the solution for a single angle of incidence. For a few discrete angles of incidences (1–4) the cloaking is shown to be nearly perfect in a limited frequency range, and even for a rotational symmetric design, cloak and object appear smaller than the noncloaked object. © 2011 American Institute of Physics. [doi:10.1063/1.3540687]

With the development of transformation optics,^{1,2} the old dream of a device which when wrapped around an object will render the object invisible to the human eye seems within reach. In order to hide a given object for a specific frequency range in the electromagnetic spectrum, it is necessary to obtain the electromagnetic properties of this so-called cloak and be able to realize these properties. The electromagnetic properties, permittivity and permeability, for a cloak can be derived by the aforementioned transformation optics.^{1,2} However, no materials readily available in nature possess the required extreme properties, and hence this calls for a method to artificially engineer materials that do so. So far microwave and near-optical frequency realizations have been achieved based on the use of metamaterials.^{3,4} The tailored microstructure of such metamaterials has to be much smaller than the wavelength, and this makes it very challenging to realize the desired magnetic properties for optical frequencies. Even though several studies have made approximations to ideal cloaking^{5–8} and all-dielectric carpet cloaking has been demonstrated,⁹ nobody has systematically addressed the intriguing question: “How efficiently can we cloak when using conventional simple isotropic dielectric media readily available in nature?”

In this work we apply gradient-based topology optimization¹⁰ to find the permittivity distribution for a non-magnetic cloak that hides an ideal metallic cylinder. Furthermore, the evolution of the optimized designs along with the corresponding cloaking properties is investigated for increasing number of incident angles, i.e., increased symmetry. The presented methodology does not only apply for electromagnetic waves, but can also be used for acoustic cloaks.

An infinitely long and ideal metallic cylinder is illuminated by a uniform monochromatic wave propagating in free space. Due to the invariance of the electromagnetic properties along the cylinder axis, the problem can be formulated in a plane perpendicular to the cylinder axis. A first order absorbing boundary condition¹¹ is used as an approximation to the Sommerfeld radiation condition in order to truncate the infinite domain. The ideal metallic cylinder can be described as having a perfect electrically conducting (PEC) condition at the interface to free space. Thus, the computational domain is given in two dimensions using three concentric circles, as shown in Fig. 1. The inner, middle, and outer

domains represent the PEC cylinder, the cloak, and the surroundings, respectively. The problem is governed by Maxwell’s equation in time-harmonic form, and the wave is propagating in simple media. Hence, the presented problem can be reformulated into a scalar Helmholtz equation for the E_z -polarized wave. We choose to solve the problem using the finite element method.^{11,12} A scattered-field formulation is used in order to reduce the dispersion error. The uniform incident field E_z^i is formulated as

$$E_z^i = E_0 e^{-jk_0 \mathbf{k} \cdot \mathbf{r}}, \quad (1)$$

where E_0 is the amplitude of the wave, $j = \sqrt{-1}$, k_0 is the free space wave number, $\mathbf{k} = \{k_x, k_y\}^T$ is the normalized directional wave vector, and $\mathbf{r} = \{x, y\}^T$ is the spatial position vector. In a scattered-field formulation the inhomogeneous Helmholtz equation, the first order absorbing boundary condition¹¹ in free space, and the PEC boundary condition are, respectively, formulated as

$$\nabla \cdot (\mu_r^{-1} \nabla E_z^s) + k_0^2 \epsilon_r E_z^s = -k_0^2 (\epsilon_r - \mu_r^{-1}) E_z^i, \quad (2)$$

$$\mathbf{n} \cdot \nabla E_z^s + jk_0 E_z^s = 0, \quad (3)$$

$$E_z^s = -E_z^i, \quad (4)$$

where E_z^s is the scattered field; ϵ_r and μ_r are the relative permittivity and permeability, respectively; and $\mathbf{n} = \{n_x, n_y\}^T$

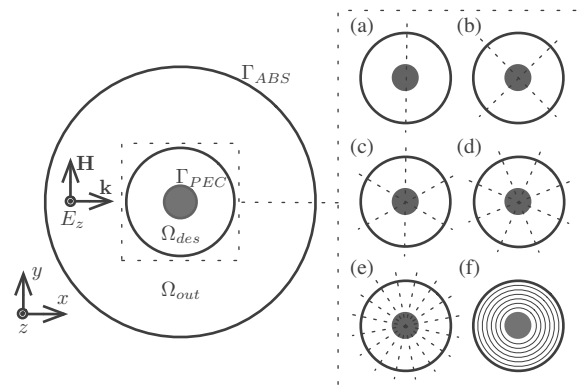


FIG. 1. Computational domain. (a)–(e) show the design domains equipped with one, two, three, four, and eight symmetry lines, respectively. The design domain with rotational symmetry is given in (f).

^{a)}Electronic mail: jban@mek.dtu.dk.

is the outward-pointing normal vector of the boundary. The boundary between free space and the cloak is formulated by a continuity condition. In the cloaking literature the boundary between free space and the cloak is usually impedance matched; however, recent studies¹³ have shown that a non-magnetic cloak whose boundary to free space is not impedance matched also may perform well.

The standard topology optimization approach using a density method is implemented.¹⁰ The relative permeability is set to 1 in order to mimic a nonmagnetic material; hence, only the spatial distribution of the relative permittivity is varied in the design process. The cloak domain wrapped around the cylinder is defined as the design domain, in which the relative permittivity can be varied continuously on an element basis between 1 and 6. A design variable, $\rho \in [0; 1]$, for each element is introduced as a relative element material density in order to interpolate between free space permittivity $\epsilon_r^{\min}=1$ and the upper bound on the permittivity $\epsilon_r^{\max}=6$. Thus, the interpolation function is given as

$$\epsilon_r = \epsilon_r^{\min} + \rho(\epsilon_r^{\max} - \epsilon_r^{\min}). \quad (5)$$

In contrast to most topology optimization problems intermediate values of the permittivity in the final design are in this problem both physically sound and realizable as graded index materials, which can be obtained based on varying doping profiles or by nanoporation.⁹ A density filter^{14–16} is introduced to aid realizations of the optimized designs by enforcing a minimum length scale on the design. Additionally a volume constraint is imposed.

In order to cloak the cylinder the objective is to minimize the norm of the scattered field in the surroundings,

$$\Phi = \frac{1}{\Phi_0} \int_{\Omega_{\text{out}}} E_z^s \overline{E_z^s} d\mathbf{r},$$

where the overbar denotes the complex conjugate and Φ_0 is the norm of the scattered field in the outer domain when no cloak is present. The reference value Φ_0 is included in order to make the objective dimensionless as well as easy to interpret. When $\Phi < 1$, cloak and cylinder appear smaller than the noncloaked cylinder. The gradient-based optimization routine, method of moving asymptotes,¹⁷ is applied to update the design in an iterative approach. The sensitivities are obtained using the adjoint method.¹⁸

Efficient optimization for multiple incident angles can be performed by introducing symmetry constraints on the design. Symmetry lines divide the original design domain into equally sized subdomains in a number corresponding to the number of incident waves. As the number of angles goes to infinity the design becomes rotationally symmetric as sketched in Fig. 1.

Using the method outlined we have optimized for one, two, three, four, eight, and infinitely many symmetry lines. The results are shown in Fig. 2. When using one and up to four symmetry lines the optimized designs cloak the metallic cylinder nearly perfectly for the considered angles of incidence. The optimized designs for one to four symmetry lines are basically waveguides which guide and delay the waves inside the cloak and phase match them to the waves outside. The angle sweeps shown in Fig. 3 reveal that the cloaking effect is highly localized to the considered angles of incidence for these four designs. In order to make the cloak more

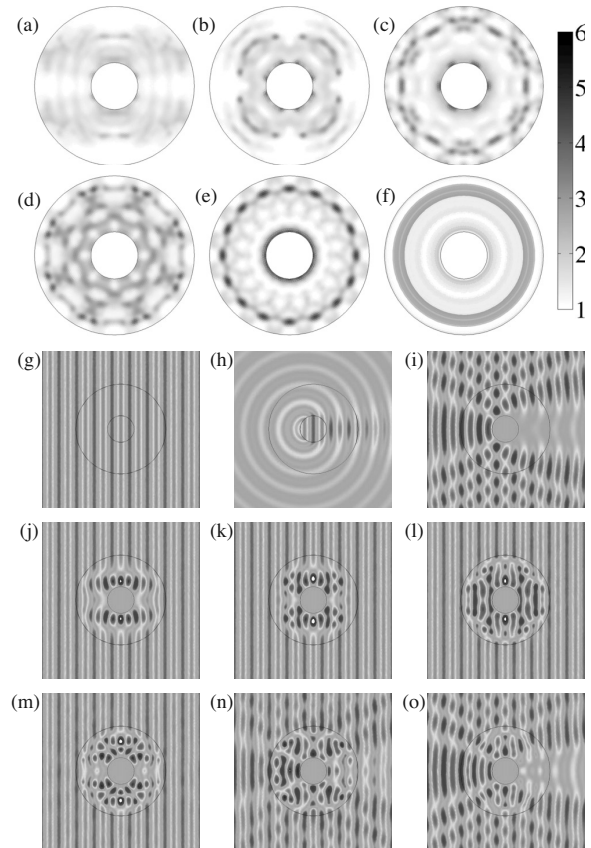


FIG. 2. (Color online) The cloak designs and FE simulations. (a)–(e) The dielectric layout of the cloaks for one, two, three, four, and eight symmetry lines, respectively. (f) The rotational symmetric design. The gray scale indicates the optimized relative permittivity distribution that ranges between 1 and 6. (j)–(o) The corresponding total electric fields. (g)–(i) The incident, scattered, and total electric fields without any cloak wrapped around the PEC cylinder.

versatile to various angles of incidence, more symmetry lines are added to the design domain at the cost of increased objective value as shown in Fig. 4.

A robust design for small perturbations in the angle of incidence is obtained by illuminating with uniform waves incident in an interval from -5° to 5° on the design domain and cylinder. The optimization is formulated as a *minimum-*

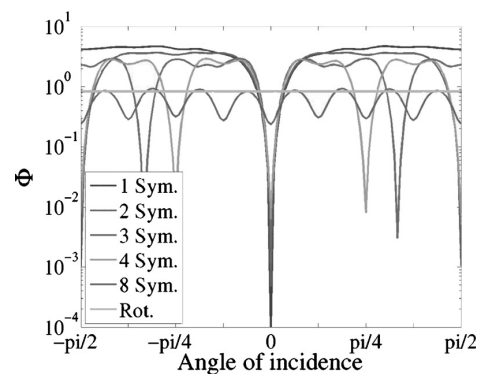


FIG. 3. (Color online) Sweep over the angle of incidence from $-\pi/2$ to $\pi/2$.

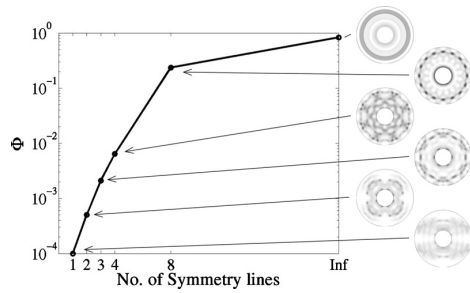


FIG. 4. The evolution of the cloak designs for increasing number of symmetry lines up to a rotational symmetric design. Remark that all designs result in $\Phi < 1$, i.e., cloak and cylinder appear smaller than the noncloaked cylinder.

maximum problem, i.e., the load case which yields the highest scattering in each iteration step is minimized. The resulting cloak is shown in Fig. 5(b), and the angle sweep in Fig. 5(a) clearly shows that the cloak can be operated in a broader

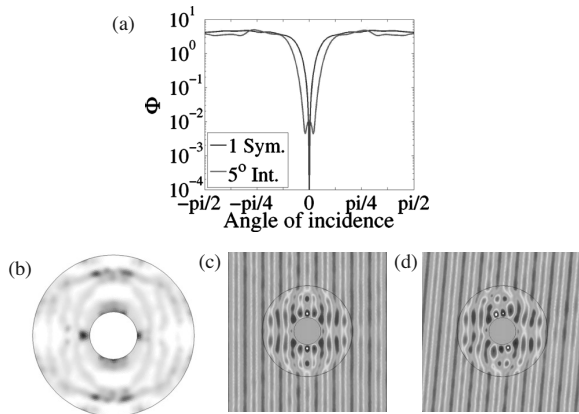


FIG. 5. (Color online) Design, sweep, and finite element simulations of wave incident in an interval from -5° to 5° . (a) Sweep through angle of incidence for design optimized at 0° and in the interval, respectively. (b) The dielectric layout for the cloak operating in the interval. [(c) and (d)] The total electric fields for a wave at 0° and -5° incidence on the cloak from (b), respectively.

incident angle interval at the cost of increased scattering.

In conclusion we have outlined a method of designing cloaks that can be realized with readily available dielectric materials. The evolution of topology optimized cloaks operating at various degrees of symmetry is presented. The analysis reveals that near perfect cloaking can be achieved when the cloaks are operating at up to four symmetric angles of incidence. Even for the isotropic design, cloak and cylinder appear smaller than the noncloaked cylinder. However, all presented designs have a narrowband performance, where a deviation in the frequency of less than 10% will result in $\Phi > 1$. The method of designing cloaks can further be extended in several ways, e.g., by optimizing for wider frequency ranges, radar cross sections, or directive properties.

This work was supported by the Eurohorcs/ESF European Young Investigator Award (EURYI) and by the Danish Research Council for Technology and Production (Grant No. 274-06-0507).

¹J. B. Pendry, D. Schurig, and D. R. Smith, *Science* **312**, 1780 (2006).

²U. Leonhardt, *Science* **312**, 1777 (2006).

³D. Schurig, J. J. Mock, B. J. Justice, S. A. Cummer, J. B. Pendry, A. F. Starr, and D. R. Smith, *Science* **314**, 977 (2006).

⁴V. M. Shalaev, W. Cai, U. K. Chettiar, H.-K. Yuan, A. K. Sarychev, V. P. Drachev, and A. V. Kildishev, *Opt. Lett.* **30**, 3356 (2005).

⁵B.-I. Popa and S. A. Cummer, *Phys. Rev. A* **79**, 023806 (2009).

⁶W. Cai, U. K. Chettiar, A. V. Kildishev, and V. M. Shalaev, *Appl. Phys. Lett.* **91**, 111105 (2007).

⁷Y. Huang, Y. Feng, and T. Jiang, *Opt. Express* **15**, 11133 (2007).

⁸H. Ma, S. Qu, Z. Xu, and J. Wang, *Opt. Express* **16**, 15449 (2008).

⁹J. Valentine, J. Li, T. Zentgraf, G. Bartal, and X. Zhang, *Nature Mater.* **8**, 568 (2009).

¹⁰M. P. Bendsøe and O. Sigmund, *Topology Optimization: Theory, Methods and Applications* (Springer, Berlin, 2003).

¹¹J. Jin, *The Finite Element Method in Electromagnetics* (Wiley, New York, 2002).

¹²COMSOL MULTIPHYSICS, COMSOL AB, Stockholm, www.comsol.se.

¹³J. Zhang, Y. Lou, and N. A. Mortensen, *Appl. Phys. Lett.* **96**, 113511 (2010).

¹⁴B. Bourdin, *Int. J. Numer. Methods Eng.* **50**, 2143 (2001).

¹⁵T. E. Bruns and D. A. Tortorelli, *Comput. Methods Appl. Mech. Eng.* **190**, 3443 (2001).

¹⁶O. Sigmund, *Struct. Multidiscip. Optim.* **33**, 401 (2007).

¹⁷K. Svanberg, *Int. J. Numer. Methods Eng.* **24**, 359 (1987).

¹⁸J. S. Jensen and O. Sigmund, *J. Opt. Soc. Am. B* **22**, 1191 (2005).

Publication [P2]

Towards all-dielectric,
polarization-independent optical cloaks

Towards all-dielectric, polarization-independent optical cloaks

Jacob Andkjær,^{1,a)} N. Asger Mortensen,² and Ole Sigmund¹

¹Department of Mechanical Engineering, Technical University of Denmark, 2800 Kongens Lyngby, Denmark

²Department of Photonics Engineering, Technical University of Denmark, 2800 Kongens Lyngby, Denmark

(Received 16 September 2011; accepted 12 February 2012; published online 6 March 2012)

Fully enclosing, all-dielectric cloaks working for both E_z and H_z polarizations simultaneously are presented in this letter. The cloaks are effective for two antiparallel angles of incidence, and the layout of standard dielectric material in the cloak is determined by topology optimization. Scattering from cylinder and cloak is reduced for an H_z -polarized wave compared to an E_z -polarized wave by taking advantage of the surface mode at the perfectly electric conducting boundary. Perhaps contrary to simple intuition, fully enclosed, all-dielectric, low-contrast cloaks cannot be designed effectively when distributing a material with lower permittivity than the background material. © 2012 American Institute of Physics. [http://dx.doi.org/10.1063/1.3691835]

The layout of the material parameters for cloaks that manipulate electromagnetic waves to flow around an object without any scattering can conveniently be found by analytical transformation optics approaches.^{1,2} However, the required material parameters for fully enclosing or complementary medium-based³ cloaks are extreme in some regions of the cloak. Typical realizations⁴ rely on resonances having a narrow band and lossy response. Furthermore, sub-wavelength artificial structuring is challenging for optical frequencies. On the other hand, material parameters for all-dielectric carpet cloaks⁵ need not to be extreme, thus circumventing the above challenges. Both two-dimensional (2D) and recently three-dimensional (3D) macroscopic all-dielectric carpet cloaks have been demonstrated (cf. Refs. 6–9). Here, we address the more challenging problem of designing fully enclosing, all-dielectric cloaks.

Recent results¹⁰ show that gradient-based topology optimization¹¹ can be used to find the permittivity distribution for a low-contrast, all-dielectric, fully enclosing optical cloak that hides an ideal metallic cylinder for up to 4 symmetrically distributed angles of incidence or for an incoming angular interval, of ± 5 . The study was based on distributing material with a higher permittivity than the background material (free space) and illuminating by an E_z -polarized wave. In this letter, we present fully enclosing, all-dielectric cloaks effective for both E_z and H_z polarizations simultaneously. Furthermore, we study the cloaking effect of distributing material with either higher or lower permittivity than the background material. The optimized designs for the former case delay the waves in regions of higher permittivity than the background and, subsequently, phase match them to the waves outside. Intuitively, distributing dielectric material having a lower permittivity than the background material would result in cloaking performance on the same level or better; however, this is not the case as we will show.

The numerical setup is identical to the previous study.¹⁰ The computational domain is given in 2D using 3 concentric circles, see Fig. 1. The inner, middle, and outer domains represent the perfectly electric conducting (PEC) cylinder, the

cloak, and the surroundings, respectively. Assuming invariance of the electromagnetic properties along the cylinder axis, Maxwell's equations simplify to the scalar Helmholtz equation. The problem is solved using the finite-element method (FEM).^{12,13} A scattered-field formulation with $H_z = H_z^s + H_z^i$, where H_z^s and H_z^i are the scattered and incident fields, respectively, is used in order to reduce the dispersion error. For the incident field H_z^i , we consider plane wave illumination and solve the wave equation

$$\nabla \cdot \left(\epsilon_r^{-1} \nabla H_z \right) + k_0^2 \mu_r H_z = 0, \quad (1)$$

where ϵ_r is the relative permittivity, μ_r is the relative permeability, and k_0 is the free space wave number. The computational domain is truncated on the outer boundary Γ_{ABS} using a first order absorbing boundary condition for the scattered field $\mathbf{n} \cdot \epsilon_r^{-1} \nabla H_z^s + j k_0 \sqrt{\epsilon_r^{-1} \mu_r} H_z^s = 0$, where \mathbf{n} is the outward-pointing normal vector of the boundary and $j = \sqrt{-1}$. Equivalent equations for the E_z polarization are easily obtained by interchanging $H_z \leftrightarrow E_z$ and $\mu_r \leftrightarrow \epsilon_r$.

We mimic a strongly scattering object by imposing a PEC boundary condition, $\mathbf{n} \times \mathbf{E} = 0$, at Γ_{PEC} . For the E_z polarization, this is equivalent to $E_z = 0$ (no field on the

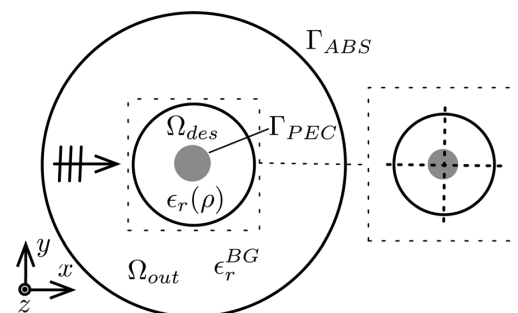


FIG. 1. (Color online) Schematics of a cylindrical cloak illuminated by either an E_z - or an H_z -polarized uniform plane waves in a background permittivity ϵ_r^{BG} (either vacuum or a typical dielectric). In the design domain Ω_{des} , the permittivity $\epsilon_r(\rho)$ can be varied continuously on an element basis to create the cloaking effect of a PEC cylinder (innermost region).

^{a)}Electronic mail: jban@mek.dtu.dk.

boundary) while $\mathbf{n} \cdot (\epsilon_r^{-1} \nabla H_z) = 0$ for the H_z polarization (the field is not necessarily zero, while the radial derivative is). The latter case may support surface waves, and this difference will have an important effect on the performance of the optimized cloaks.

We employ a standard density-based topology optimization method¹¹ and we restrict our investigations to non-magnetic materials ($\mu_r = 1$). In the cloak domain wrapped around the cylinder, the relative permittivity can be varied continuously on an element basis between free space permittivity $\epsilon_r^{\min} = 1$ and an upper bound on the permittivity $\epsilon_r^{\max} = 2$, achievable with a broad range of naturally occurring transparent dielectric materials. For each element, we introduce a design variable, $\rho \in [0; 1]$, as a relative element material density. Furthermore, we make a linear interpolation of $\epsilon_r(\rho)$ so that

$$\epsilon_r(\rho) = \epsilon_r^{\min} + \rho(\epsilon_r^{\max} - \epsilon_r^{\min}). \quad (2)$$

In this analysis, we test cloaks of either graded index material, which permits intermediate values of the permittivity, or discrete material designs, which do not. The graded or discrete designs are achieved by introducing a density filter^{14,15} or a Heaviside projection filter¹⁶ with a robust formulation,¹⁷ respectively. The permittivity of the background material, ϵ_r^{BG} , is set to either 1 or 2, depending on whether we are distributing dielectric material having a higher or lower permittivity than the background material, respectively. A volume constraint is imposed along with symmetry constraints on the design with two symmetry lines around which the 4 equally sized sub-domains can be mirrored as shown in Fig. 1. Utilizing the symmetry lines, all cloaks are designed to be effective for two antiparallel angles of incidence (0° and 180°).

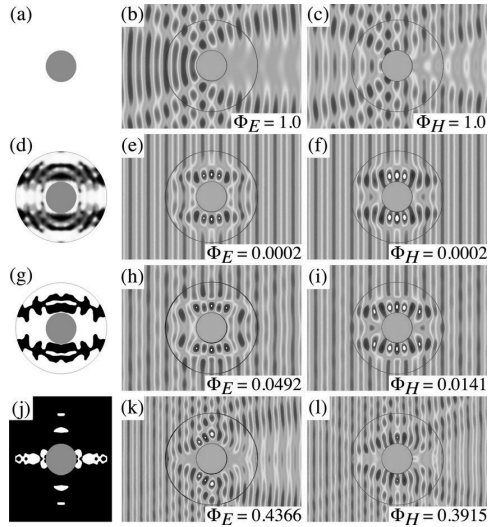


FIG. 2. (Color online) Polarization-independent cloak designs and the associated objective values Φ [Eq. (3)] for E_z and H_z -polarized waves. The middle and rightmost panels show the total fields for E_z and H_z polarizations, respectively. Panels (a)–(c) show total fields for scattering of the PEC cylinder itself. Panels (d)–(f) show graded cloak designs with $\epsilon_r^{\text{BG}} = 1$, while (g)–(i) show the discrete counterparts. Likewise, panels (j)–(l) show the discrete design with $\epsilon_r^{\text{BG}} = 2$. In the linear gray-scale plots, white and black color correspond to $\epsilon_r = 1$ and $\epsilon_r = 2$, respectively.

In order to cloak the cylinder, the objective is to minimize the norm of the scattered field in the surroundings,

$$\Phi = \Phi_E + \Phi_H = \frac{1}{W_E} \int_{\Omega_{\text{out}}} |E_z^s|^2 d\mathbf{r} + \frac{1}{W_H} \int_{\Omega_{\text{out}}} |H_z^s|^2 d\mathbf{r}, \quad (3)$$

where W is the norm of the scattered field in the outer domain when no cloak is present. This normalization makes $\Phi_{E,H}$ dimensionless and easy to interpret. If $\Phi_{E,H} < 1$, cloak and cylinder produce less scattering than the non-cloaked cylinder. The design is updated iteratively using the gradient-based optimization routine method of moving asymptotes (MMA).¹⁸ The sensitivities are obtained using the adjoint method.¹⁹

Graded and discrete designs that minimize the scattering from both E_z and H_z polarizations simultaneously are presented in Fig. 2 (leftmost panels). The total fields for E_z and H_z polarizations are shown in the middle and rightmost panels, respectively. The fields from the non-cloaked cylinders for E_z and H_z polarizations with $\epsilon_r^{\text{BG}} = 1$ are shown in Figs. 2(b) and 2(c) as a reference. In case of $\epsilon_r^{\text{BG}} = 1$, the graded design result in scattering less than 1% of the non-cloaked cylinder and even for the more restrictive case with a discrete design scattering is reduced to less than 5% for both polarizations. The H_z polarization for the discrete design yields less scattering than the E_z polarization, due to the less restrictive boundary condition for the H_z polarization. Contrary to simple intuition, considerable scattering is produced by all designs with $\epsilon_r^{\text{BG}} = 2$. Graded designs with $\epsilon_r^{\text{BG}} = 2$ produce more scattering than the discrete counterparts; hence, we have omitted graded designs and show only the discrete design. To analyze the cause for the degeneration in cloaking performance for designs with $\epsilon_r^{\text{BG}} = 2$, we relax the problem and investigate whether or not effective cloaks with $\epsilon_r^{\text{BG}} = 2$ can be designed individually for either the E_z or H_z polarization.

The optimized cloaks and total fields for E_z and H_z polarizations are shown in Figs. 3 and 4, respectively. Even though we relax the problem and optimize individually for either one or the other polarization, both the graded and

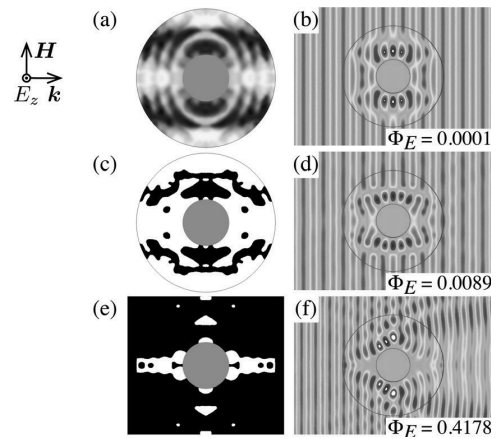


FIG. 3. (Color online) Cloak designs and associated objective values Φ [Eq. (3)] for E_z polarization. For a description of the individual panels, see caption of Figs. 2(d)–2(l).

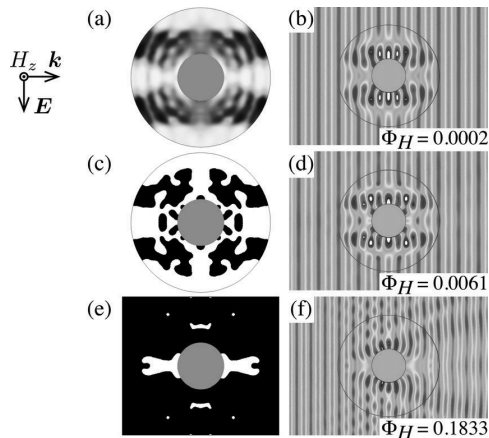


FIG. 4. (Color online) Cloak designs and associated objective values Φ [Eq. (3)] for H_z polarization. For a description of the individual panels, see caption of Figs. 2(d)–2(l).

discrete designs with $\epsilon_r^{\text{BG}} = 2$ result in poor cloaking performance. We thereby see that the limited cloaking performance for designs with $\epsilon_r^{\text{BG}} = 2$ is not caused by the requirement on the cloaks to be effective for both polarizations simultaneously. Instead, we conclude that it is a consequence of optical modes tending to concentrate their electric- or magnetic-field energy in regions of high dielectric values.²⁰ For the designs with $\epsilon_r^{\text{BG}} = 1$, the field energy is concentrated in regions of higher permittivity, wherein the wave is delayed and subsequently phase matched to the waves outside the cloak. For the designs with $\epsilon_r^{\text{BG}} = 2$, we can only design regions, which the field avoids. Hence, it is possible to split the waves in front of the object with very limited backscattering. However, the waves cannot be collected on the backside of the object without scattering. For the H_z polarization, a surface wave can exist on the PEC boundary as mentioned previously. The scattering is reduced by a factor of two for H_z polarization with $\epsilon_r^{\text{BG}} = 2$ compared with E_z polarization by coupling the wave into the surface mode, which makes it easier for the wave to flow around the object.

Finally, we address the radar cross section from back-scattering to forward-scattering produced by either the individually optimized discrete designs or the non-cloaked cylinders (as reference), see Fig. 5. The radar cross section is normalized by the radar cross section in the backscattering direction from the non-cloaked cylinder for the E_z polarization. For $\epsilon_r^{\text{BG}} = 2$, the backscattering of the designs are reduced significantly and are on level with the designs for $\epsilon_r^{\text{BG}} = 1$. On the contrary, the radar cross section for $\epsilon_r^{\text{BG}} = 2$ is comparable to that of the non-cloaked cylinders around the forward scattering direction.

In conclusion, we have presented directional topology optimized all-dielectric low-contrast cloaks that minimize scattering for combined E_z and H_z polarized waves. Near-perfect cloaking is achieved for the graded design with $\epsilon_r^{\text{BG}} = 1$ and even for a discrete design scattering for both polarizations is reduced to less than 5% of that from the non-cloaked cylinder. Furthermore, the effect of the background material has been investigated. The results indicate that fully

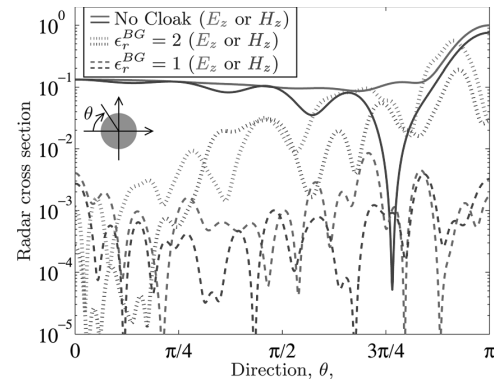


FIG. 5. (Color online) Radar cross section from back-scattering ($\theta = 0$) to the forward-scattering ($\theta = \pi$) for the discrete designs with a background permittivity of $\epsilon_r^{\text{BG}} = 1$ (dashed lines) or $\epsilon_r^{\text{BG}} = 2$ (dotted lines) illuminated by either an E_z or an H_z -polarized waves. Designs with $\epsilon_r^{\text{BG}} = 2$ cause limited backscattering, but with significant forward scattering. For comparison, results for the non-cloaked cylinder are also included (solid lines).

enclosed, all-dielectric, low-contrast cloaks can be designed effectively when distributing a material with higher permittivity than the background material. However, contrary to simple intuition this is not possible for the “inverse” case, i.e., when distributing a material with lower permittivity than the background material. The backscattering is reduced significantly for all optimized designs. For an H_z -polarized wave, the optimized designs can take advantage of the surface mode at the PEC boundary and achieve less scattering than the optimized designs for the E_z -polarized wave.

This work was supported by the Villum Foundation (the NextTop project) and by the Danish Research Council for Technology and Production (Grant No. 274-06-0507).

¹J. B. Pendry, D. Schurig, and D. R. Smith, *Science* **312**, 1780 (2006).

²U. Leonhardt, *Science* **312**, 1777 (2006).

³Y. Lai, H. Y. Chen, Z.-Q. Zhang, and C. T. Chan, *Phys. Rev. Lett.* **102**, 093901 (2009).

⁴D. Schurig, J. J. Mock, B. J. Justice, S. A. Cummer, J. B. Pendry, A. F. Starr, and D. R. Smith, *Science* **314**, 977 (2006).

⁵J. Li and J. B. Pendry, *Phys. Rev. Lett.* **101**, 203901 (2008).

⁶J. Valentine, J. Li, T. Zentgraf, G. Bartal, and X. Zhang, *Nature Mater.* **8**, 568 (2009).

⁷X. Chen, Y. Luo, J. Zhang, K. Jiang, J. B. Pendry, and S. Zhang, *Nat. Commun.* **2**, 176 (2011).

⁸J. Zhang, L. Liu, Y. Luo, S. Zhang, and N. A. Mortensen, *Opt. Express* **19**, 8625 (2011).

⁹T. Ergin, N. Stenger, P. Brenner, J. B. Pendry, and M. Wegener, *Science* **328**, 337 (2010).

¹⁰J. Andkjær and O. Sigmund, *Appl. Phys. Lett.* **98**, 021112 (2011).

¹¹M. P. Bendsøe and O. Sigmund, *Topology Optimization: Theory, Methods and Applications* (Springer, Berlin, 2003).

¹²J. Jin, *The Finite Element Method in Electromagnetics* (Wiley, New York, 2002).

¹³COMSOL Multiphysics 3.5a, COMSOL AB, Stockholm.

¹⁴B. Bourdin, *Int. J. Numer. Methods Eng.* **50**, 2143 (2001).

¹⁵T. E. Bruns and D. A. Tortorelli, *Comput. Methods Appl. Mech. Eng.* **190**, 3443 (2001).

¹⁶J. K. Guest, J. H. Prévost, and T. Belytschko, *Int. J. Numer. Methods Eng.* **61**, 238 (2004).

¹⁷F. Wang, B. S. Lazarov, and O. Sigmund, *Struct. Multidiscip. Optim.* **43**, 767 (2011).

¹⁸K. Svandberg, *Int. J. Numer. Methods Eng.* **24**, 359 (1987).

¹⁹J. S. Jensen and O. Sigmund, *J. Opt. Soc. Am. B* **22**, 1191 (2005).

²⁰J. Joannopoulos, R. Meade, and J. Winn, *Photonic Crystals: Molding the Flow of Light* (Princeton University, New Jersey, 1995).

Publication [P3]

Topology optimized acoustic and
all-dielectric optical cloaks

Topology optimized acoustic and all-dielectric optical cloaks

J. Andkjær¹ and O. Sigmund¹

¹Department of Mechanical Engineering
 Technical University of Denmark
 2800 Kgs. Lyngby, Denmark
 email: jban@mek.dtu.dk, sigmund@mek.dtu.dk

Abstract

In this paper we present an alternative way of designing electromagnetic and acoustic cloaks based on isotropic and non-extreme materials. Using the standard gradient-based topology optimization method we vary the isotropic material properties within the cloak in an iterative approach, such that the norm of the scattered (electric, magnetic or acoustic) field in the surroundings is minimized. Both optimized graded-index designs and optimized designs based on circular inclusions in a background material are presented. For the specified angle of incidence the cloaking properties is shown numerically to be nearly perfect in a limited frequency range.

1. Introduction

In order to hide a given object for a specific frequency range in the acoustic or electromagnetic spectrum it is necessary to obtain the material properties of these so-called acoustic or electromagnetic cloaks and be able to realize the properties. The material properties, for electromagnetic or acoustic cloaks can be derived by a coordinate transformation in transformation optics [1] or transformation acoustics [2], respectively. Several simplified electromagnetic cloaks have been realized (e.g. [3]) and all-dielectric carpet cloaking has been demonstrated [4]. In the acoustic case realizations of the material properties derived by transformation acoustics are more cumbersome due to the anisotropic mass density, which is not common in naturally occurring materials. A recent realization, in which they make use of a transmission line approach to overcome the above challenge, of an acoustic cloak in water waves for ultrasound has been demonstrated [5]. All the theoretical work and realizations of electromagnetic and acoustic cloaks are to the authors knowledge based on anisotropic material parameters, however, we have in this work systematically addressed the intriguing question: How efficiently can we cloak when using conventional simple isotropic media readily available in nature?. Results [6] show that gradient-based topology optimization [7] can be used to find the permittivity distribution for a low-contrast all-dielectric optical cloak that hides a perfectly electric conducting cylinder in a limited frequency range for up to 4 symmetrical distributed angles of incidence. The physics of time-harmonic acoustic waves and time-harmonic E_z - or H_z -polarized electromagnetic waves are governed by an identical mathematical form; the scalar Helmholtz equation as shown below in equation (1). The differences in the Helmholtz equation for acoustic, E_z - and H_z -polarized waves are found in the material properties and state variable; mathematical the equations are the same form. Thus with a limited reformulation, the initial methodology of designing optical cloaks can also be used to design an acoustic cloak with isotropic material properties to circumvent the problems of the anisotropic mass density.

Wave-type	u	A	B
E_z -polarized	E_z	μ_r^{-1}	ϵ_r
H_z -polarized	H_z	ϵ_r^{-1}	μ_r
Acoustic	p	ρ_r^{-1}	κ_r^{-1}

Tab. 1: Parameter relations for a general notation of Helmholtz' equation.

2. Method

The scalar Helmholtz equation governs the physics of both an E_z -polarized, H_z -polarized and acoustic wave and in a general form we can state this as

$$\nabla \cdot (A \nabla u) + k_0^2 B u = 0 \quad (1)$$

where A , B and u are given in Tab. 1, $k_0 = \omega/c$ is the free space wave vector, ω is the angular frequency, $c = (\epsilon_0 \mu_0)^{-1/2}$ is the speed of light in vacuum for an electromagnetic wave or $c = (\rho_0 \kappa_0^{-1})^{-1/2}$ is the speed of sound in air for an acoustic wave, ϵ is the permittivity, μ is the permeability, ρ is the density, κ is the bulk modulus, the subscripts r and 0 denotes the relative parameters to that of free space and air for the electromagnetic and acoustic wave, respectively.

The problem is modeled in 2D using 3 concentric circles and solved using the finite element method [8]. The inner, middle and outer domain represent the hidden cylinder, the cloak and the surroundings, respectively. The material of the hidden cylinder is iron for the acoustic problem and a perfectly electric conductor for the electromagnetic problem. Using the standard gradient-based topology optimization method [7] we vary the isotropic material properties A and B within the cloak in an iterative approach, such that the norm of the scattered (electric, magnetic or acoustic) field in the surroundings is minimized. In case of the electromagnetic cloak we set the relative permeability to 1 in order to mimic a non-magnetic material. Hence for the electromagnetic problem the relative permittivity, ϵ_r , is varied continuously on an element basis between two materials using a linear interpolation and for the acoustic problem the relative density, ρ_r , and the bulk modulus, κ_r , are varied. Without any penalization of intermediate material properties a graded index material is obtained from the optimization. Hence the Material-Mask Overlay Strategy (MMOS) [9] is used in order to achieve designs without intermediate material properties. Furthermore the shape of one material is confined to circles, which make the designs easier to realize. The MMOS formulation results in an optimization problem, in which the position and radii of the prescribed circles are varied.

3. Results

Using the method outlined we have optimized for an E_z -polarized and an acoustic wave. In Fig. 1 (a) and (f) the non-cloaked cylinder illuminated by a uniform plane E_z -polarized and acoustic wave are presented, respectively. The interference pattern from the scattered field is very notable, especially as a shadow region behind the cylinders. For the E_z -polarized problem we interpolate the relative permittivity, ϵ_r , between 1 and 6 for the graded design in Fig. 1 (b). The design obtained from MMOS results in circular inclusions with a relative permittivity of 3 in a background material of a relative permittivity of 1 in Fig. 1 (d). The circular inclusions gives a layout of effective permittivity that mimics the graded design. Both optimized designs for the E_z -polarized wave are basically waveguides which guide and delay the waves inside the cloak and phase match them to the waves outside. For the acoustic problem we interpolate the relative density, ρ_r , between 1 (air) and $6.54 \cdot 10^3$ (iron) and the relative bulk modulus, κ_r , between 1 (air) and $1.20 \cdot 10^6$ (iron). The graded design with intermediate material properties and resulting field is presented in Fig. 1 (g) and (h), respectively. A physical interpretation of the graded

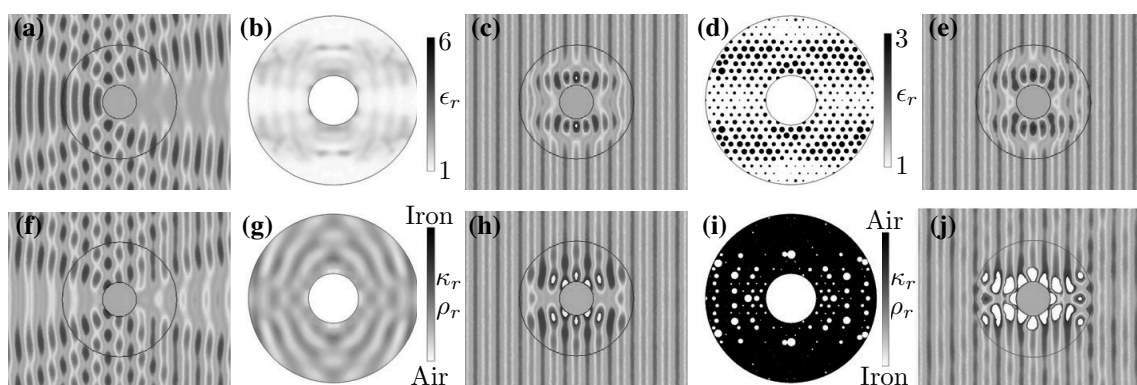


Fig. 1: The cloak designs and FE simulations for an E_z polarized wave (a)-(e) and an acoustic wave (f)-(j). (a) and (f) show the non-cloaked cylinders. (b), (c), (g) and (h) show the graded designs and resulting fields. (d), (e), (i) and (j) show the designs obtained using MMOS and resulting fields.

design for the acoustic problem with a linear interpolation between air and iron is not straight-forward, but included here as a reference. Using MMOS a design containing iron-rods of varying radii and position are obtained and presented in Fig. 1 (i) with the resulting field shown in Fig. 1 (j). However, the presented designs for both the electromagnetic and the acoustic problem are both highly resonant to the frequency and highly localized to the considered angle of incidence. Hence a perturbation in either the frequency or angle of incidence have a negative effect on the cloaking properties of the designs.

4. Conclusion

We have numerically demonstrated that topology optimization can be used to find the layout of isotropic material in both electromagnetic and acoustic cloaks. Both optimized graded-index designs and optimized designs based on circular inclusions in a background material are presented. For the specified angle of incidence the cloaking properties is nearly perfect in a limited frequency range. The method of designing cloaks can further be extended in several ways, e.g. by optimizing for wider frequency ranges, radar cross sections or directive properties.

References

- [1] J. B. Pendry, D. Schurig and D. R. Smith, Controlling electromagnetic fields, *Science*, vol. 312, pp. 1780-1782, 2006.
- [2] S. A. Cummer and D. Schurig, One path to acoustic cloaking, *New J. Phys.*, vol. 9, 45, 2007.
- [3] D. Schurig, J. J. Mock, B. J. Justice, S. A. Cummer, J. B. Pendry, A. F. Starr and D. R. Smith, Metamaterial electromagnetic cloak at microwave frequencies, *Science*, vol. 314, pp. 977-980, 2006.
- [4] J. Valentine, J. Li, T. Zentgraf, G. Bartal and X. Zhang, An optical cloak made of dielectrics, *Nat. Mater.*, vol. 8, pp. 568-571, 2009.
- [5] S. Zhang, C Xia and N. Fang, Broadband Acoustic Cloak for Ultrasound Waves, *Phys. Rev. Lett.*, vol. 106, p. 024301, 2011.
- [6] J. Andkjær and O. Sigmund, Topology optimized low-contrast all-dielectric optical cloak, *Appl. Phys. Lett.*, vol. 98, p. 021112, 2011.
- [7] M. P. Bendsøe and O. Sigmund, *Topology Optimization: Theory, Methods and Applications*, Springer, Berlin, 2003.
- [8] J. Jin, *The Finite Element Method in Electromagnetics*, John Wiley & Sons Inc., New York, 2002.
- [9] C. Jain and A. Saxena, An improved material-mask overlay strategy for topology optimization of structures and compliant mechanisms, *J. Mech. Design*, vol. 132, p. 061006, 2010.

Publication [P4]

Annular Bragg gratings as minimum
backscattering cloaks

Annular Bragg gratings as minimum backscattering cloaks

Jacob Andkjær* and Ole Sigmund

Department of Mechanical Engineering, Technical University of Denmark, 2800 Kongens Lyngby, Denmark

(Dated: March 21, 2012)

We demonstrate that an annular Bragg grating cloak made of non-absorbing, isotropic, standard dielectric materials, readily available in nature, efficiently can eliminate the backscattering from strongly scattering cylindrical objects illuminated by plane waves. The backscattering reduction improves with increasing number of rings and/or increased permittivity contrast. Numerical results indicate that the position and thickness of the Bragg rings converge to those of a conventional annular quarter-wavelength Bragg grating when the size of the cylinder becomes much larger than the wavelength.

Backscattering from hard obstacles illuminated by electromagnetic waves can be reduced either by absorbing materials or by cloaking approaches that deflect waves around objects making them invisible to the observer[1–3]. Examples of absorbers are Dallenbach layers, Salisbury Screens[4] and Jaumann Layers. Dallenbach layers use the bulk material for absorption, whereas Salisbury Screens and Jaumann Layers use resistive sheets placed a multiple of a quarter wavelength from a plane surface. For curved and cylindrically shaped objects a degeneration in performance of both Salisbury Screens[5] and Jaumann absorbers[6, 7] has been reported. Material layouts for cloaks that manipulate electromagnetic waves to flow around an object without any scattering can conveniently be found with the aid of analytical transformation optics[1–3]. The required material parameters are extreme in some regions of the cloak, which makes realizations challenging. A relaxed form of the cloaking problem that does not involve singularities is the carpet cloak[8]. The carpet cloak does not need extreme material parameters and hence realizations of micro- and macroscopic carpet cloaks at optical frequencies have been demonstrated using all-dielectric structures, see e.g. Refs. 9–11.

Here we relax the original cloaking problem by only requiring elimination of backscattering in a limited angular range. Although relaxed the cloaking problem is highly relevant in e.g. radar-setups where source and detector are coincident. As it turns out, this relaxation results in readily realizable omnidirectional backscattering cloaks made of isotropic, low-contrast, non-absorbing, all-dielectric materials readily available in nature. The idea comes from a systematic numerical optimization approach followed by extensive analytical and numerical studies.

Assuming invariance of the electromagnetic properties along the cylinder axis, Maxwell’s equations simplify to the scalar Helmholtz equation which for E_z polarized waves is given by

$$\nabla \cdot (\mu_r^{-1} \nabla E_z) + k_0^2 \epsilon_r E_z = 0 \quad (1)$$

where ϵ_r is the relative permittivity, μ_r the relative permeability, and k_0 the free space wave number. We mimic the strongly scattering object as a cylindrical obstacle with perfect electric conducting (PEC) boundary conditions. The PEC cylinder is illuminated by a plane wave propagating in free space ($\epsilon_r = \mu_r = 1$). This setup is almost identical to the setup in Ref. 12 which demonstrates how gradient-based topology optimization[13] can be used to find the permittivity distribution for a low-contrast, all-dielectric, fully enclosing optical cloak that hides a PEC cylinder for discrete angles of incidence. Here, we use the same optimization approach to investigate the possibilities of designing omnidirectional backscattering cloaks by minimizing the norm of the scattered field in a circular trapezoidal domain enclosed at $\pm 10^\circ$ from the backscattering direction and with inner and outer radii given as 1.75 and 5 free space wavelengths from the obstacle, respectively (see Ω_{out} in Fig. 1(a)). In principle, the algorithm allows for free (but circular symmetric) distribution of material properties belonging to the interval $\epsilon_r \in [1, 2]$, however the obtained solutions are almost ”discrete” in the sense that the optimizer selects material properties at the upper or lower bounds with just small areas of intermediate values. To enforce fully discrete designs we artificially penalize intermediate material values.

The results of the optimization process are surprisingly simple annular Bragg gratings with layer dimensions that depend on the obstacle radius R_{PEC} and rings with distances close to but not equal to the quarter-wavelength. Fig. 1(a) shows a topology optimized design for a radius to free space wavelength ratio of $R_{PEC}/\lambda = 0.8$ with the resulting total field shown in Fig. 1(b). The structure consists of a thin coating of the obstacle surrounded by three concentric rings. A slightly increased cylinder radius ($R_{PEC}/\lambda = 0.83$) almost eliminates the inner coating layer (Figs. 1(c) and (d)) and slightly shifts the positions of the 3 concentric rings inwards. Topology optimized designs for other R_{PEC}/λ ratios show similar layered patterns with varying thickness of the inner coating layer. An amplification of the total field in the layered region is observed for all optimized designs as indicated in Fig. 1(i). The optimized structure acts as an annular Bragg grating with a defect introduced by the PEC

*jban@mek.dtu.dk

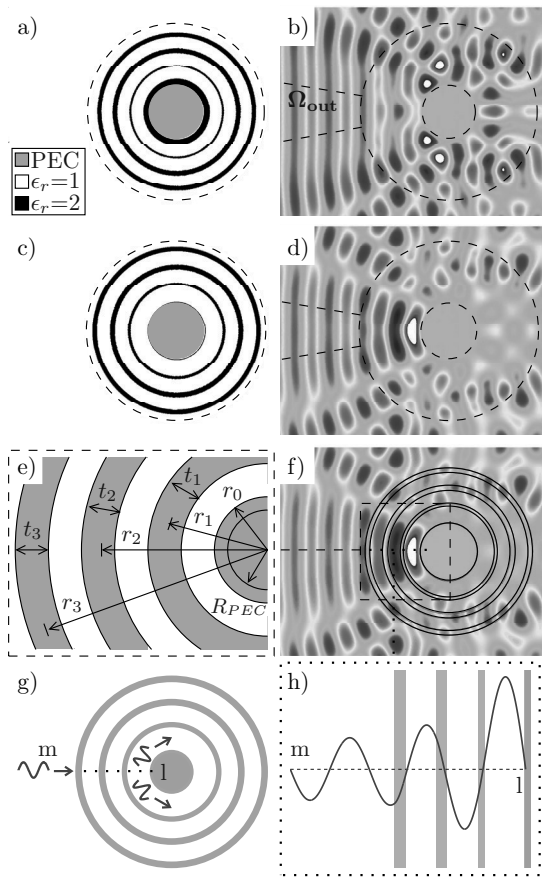


FIG. 1. (a), (c): Topology optimized designs for R_{PEC}/λ ratios of 0.8 and 0.83, respectively, and total fields (b), (d) calculated by finite element analysis. (e): The positions of layers with $\epsilon_r = 2$ are represented by 7 parameters for a 3 layer structure. (f) Total field for $R_{PEC}/\lambda = 0.82$ obtained by the analytic solution. (g) The incident wave couples to circumferentially propagating ring modes that lead the energy around the obstacle. (h) Amplification of the field due to the annular Bragg grating, where the PEC cylinder acts as an annular defect.

cylinder[14]. For a flat obstacle the incoming wave would simply be reflected, however, due to the curvature of the grating, the incoming wave couples to circumferentially propagating and confined ring modes[14] that lead the energy around the obstacle (c.f. Fig. 1g+h), resulting in scattering in all but the backscattering direction.

Multilayered concentric cylinders, composed of different dielectric materials, intended for other purposes have been treated analytically[15–17] in a cylindrical coordinate system (ρ, θ) . The analytic solution to the scattered field, E_z^s , in the outer region is given as

$$E_z^s(\rho, \theta) = E_0 \sum_{n=-\infty}^{\infty} j^n A_n H_n^{(1)}(k_1 \rho) e^{jn\theta} \quad (2)$$

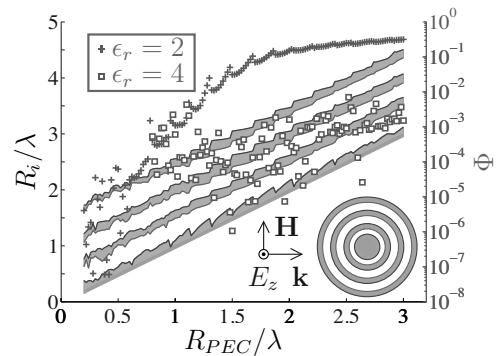


FIG. 2. Optimized positions of 3 rings illuminated by an E_z -polarized plane wave and the cloaking performance for $0.2 \leq R_{PEC}/\lambda \leq 3.0$. Optimized radial dimensions of the layers with $\epsilon_r = 2$ indicated by grey bands and confined by inner radii (red) and outer radii (blue) are measured by the left axis. Optimized

cloaking performances for $\epsilon_r = 2$ (green crosses) and $\epsilon_r = 4$ (green squares) are measured by the right axis.

where $j = \sqrt{-1}$, $E_0 = 1$ is the normalized amplitude of the incident plane wave, $H_n^{(1)}$ are the Hankel functions of the first kind, k_1 is the wave number in the outer region and A_n are the unknown coefficients, which can be determined from the boundary conditions. Apart from the PEC boundary condition at the innermost boundary, two independent continuous boundary conditions and two sets of unknown coefficients are introduced for each boundary yielding a linear equation system to be solved. We solve it directly, however Richmond’s recursive method[18] could have been used as well. The total field obtained from the analytic solution with the extracted positions of the layers from the topology optimized design for $R_{PEC}/\lambda = 0.83$ is shown in Fig. 1(f) and shows almost perfect agreement with the finite element solution (c.f. Fig. 1(d)).

From the topology optimized designs (Fig. 1a+b) we see that the layered design should start with a high index ($\epsilon_r = 2$) layer as the innermost ring (coating) and alternate between free-space and high index material. Based on this interpretation, the topology of the rings can be parameterized as shown in Fig. 1(e). The outer radius of the coating layer is given by r_0 and ring n is parameterized by its center radius r_n and its thickness t_n . Together with the analytical solution from Eq. (2), these parameters are used as inputs to a simpler optimization procedure based on the `fmincon` function in Matlab. Instead of minimizing the norm of the scattered field in a domain just next to the cloak we now minimize the norm of the field on a $\pm 10^\circ$ arc line Γ_{out} , in the far-field of the backscattering direction. This allows some scattering to occur in the near-field of the cloak, but minimizes scattering in the far-field. The far-field is here defined as 60 wavelengths from the center of the PEC cylinder. Given

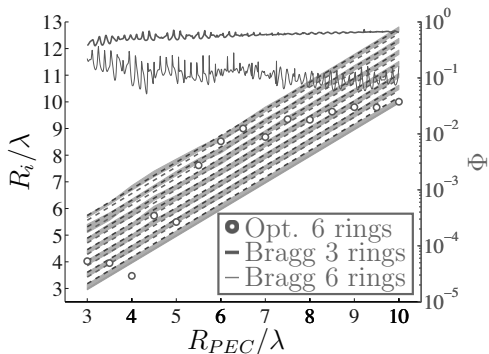


FIG. 3. Optimized positions of a 6-ring ($\epsilon_r = 2$) cloak illuminated by an E_z -polarized plane wave and the cloaking performance for $3.0 \leq R_{PEC}/\lambda \leq 10.0$. Optimized radial grating dimensions, represented by the gray-shaded areas, for the $\epsilon_r = 2$ layers are given by the left axis and the corresponding cloaking performances (green circles) are given by the right axis. Dashed red and blue lines represent the positions of conventional quarter-wavelength annular Bragg grating with corresponding cloaking performance given by the solid green lines.

the analytic solution to the scattered field from Eq. (2) the objective to be minimized is formulated as

$$\Phi = \frac{1}{W} \int_{-10^\circ}^{10^\circ} |E_z^s(\rho = 60\lambda, \theta)|^2 d\theta \quad (3)$$

where W is the norm of the scattered field on Γ_{out} for the non-cloaked PEC cylinder. When Φ is less than unity backscattering from the layered cylinder is less than the backscattering from the non-cloaked cylinder.

Optimized radial dimensions of the grating layers are indicated by grey bands confined by inner radii (red) and outer radii (blue) in Fig. 2 for three-grating-layer structures and varying obstacle diameter. The corresponding cloaking performance Φ as defined by Eq. (3) is indicated by green crosses. The varying width of the inner coating layer is observed here as well. The radii vary less for large R_{PEC}/λ ratios and the cloaking performance converges asymptotically to 1 (i.e. no cloaking). The results show that good cloaking performance ($\Phi < 0.01$) for 3 rings is achieved when $R_{PEC}/\lambda < 1.3$, however for larger ratios the cloaking performance deteriorates. Better performance can be achieved by doubling the permittivity and reoptimizing the positions and thicknesses of the rings. The cloaking performance of the optimized designs for $\epsilon_r = 4$ is presented by green squares in Fig. 2 and shows a significant improvement compared to the results for $\epsilon_r = 2$. The higher permittivity makes it possible to achieve both a higher amplification and a higher confinement of the ring modes, such that backscattering can be reduced more efficiently. It should be noted that all the shown results are optimized for a specific R_{PEC}/λ ratio (one frequency). Hence the cloaking performance will deteriorate for all other frequencies than the one optimized

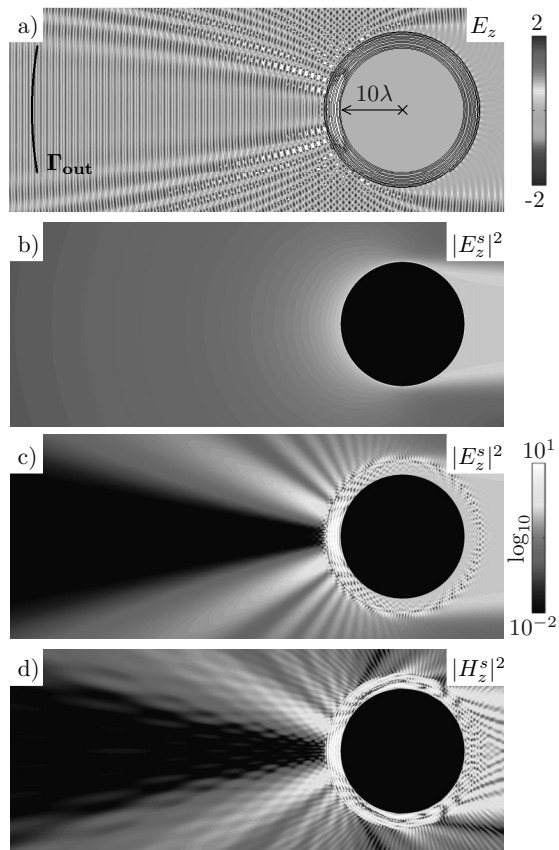


FIG. 4. Total field (a) for an optimized 6-ring cloak ($\epsilon_r = 4$, $R_{PEC}/\lambda = 10$) illuminated by an E_z -polarized wave. Norms of the scattered field are given in a \log_{10} -scale for the non-cloaked (b) and the cloaked PEC cylinder (c). Even if illuminated by an H_z -polarized plane wave (d) the E_z -optimized cloak shows good backscattering performance.

for. A remedy could be to optimize for a wider frequency range at the cost of reduced cloaking efficiency but this idea is not further pursued here.

Increasing the number of rings is another intuitive way of improving the cloaking performance and this is illustrated in Fig. 3 for $3.0 \leq R_{PEC}/\lambda \leq 10.0$. Here the permittivity is fixed to 2, however, the number of rings is doubled to 6. The positions, represented by the gray-shaded areas, of the 6 rings and the coating radius are optimized with the outlined method. At $R_{PEC}/\lambda = 3.0$ the norm of the scattered field for 3 position-optimized rings is only reduced to 0.32 (see Fig. 2) compared to the non-cloaked cylinder, whereas it has been reduced to $5.3 \cdot 10^{-5}$ for 6 rings (see green circles in Fig. 3).

We have tried to identify a simple rule for the optimal dimensions of the cloak. However, the problem is more complicated than for simple annular Bragg resonators[19] due to the coupling of the incoming wave to the cir-

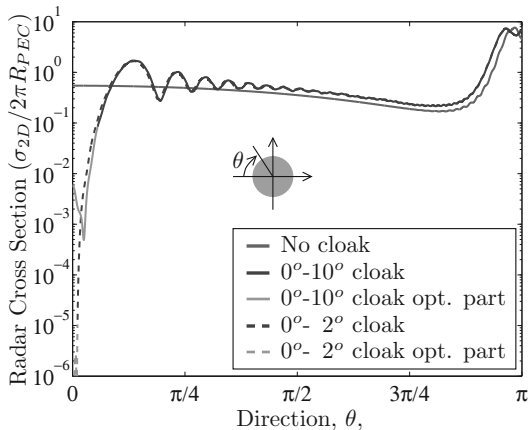


FIG. 5. Radar cross section from backscattering ($\theta = 0$) to the forward-scattering ($\theta = \pi$) for 6 position-optimized rings (blue) and non-cloaked (red) PEC cylinder illuminated by an E_z -polarized wave. The minimized part of the radar cross section is given in green. Solid and dashed lines represent angle intervals of $\pm 10^\circ$ and $\pm 2^\circ$, respectively.

cumferential waves. The semi-periodic variation of the radius of the inner coating is attributed to the optimized structure adapting itself to new ringmodes that enable the confinement. Since the effective circumferential index is hard to compute we do not believe that it is possible to define a closed-form rule for the optimal dimensions of the cloak. Nevertheless, we compare our optimized results with a simple quarter-wavelength annular Bragg grating cloak and find fairly good response - especially for larger obstacle radii. The dashed red and blue lines in Fig. 3 indicate the boundaries for a conventional constant-period, quarter-wavelength annular Bragg grating designed with periodic pairs of layers with thickness $d_i = \lambda/4n_i$ (where n_i is the refractive index of layer i), starting with high index material in the innermost layer (coating). The cloaking performances for regular Bragg gratings composed of 3 and 6 high index rings are indicated by thick and thin curves, respectively (Fig. 3). When the radius of the PEC cylinder becomes much larger than the wavelength, both the layout and the cloaking performance for the optimized 6-ring structure converge to those of the corresponding simple annular Bragg grating with 6 equidistant rings.

Fig. 4(a) shows the total field for an optimized 6-ring structure ($\epsilon_r = 4$) illuminated by an E_z -polarized wave. Figs. 4(b) and (c) show the norms $|E_z^s|^2$ of the scattered field for the non-cloaked cylinder and the optimized 6-layer structure, respectively. Even though the radius of the PEC cylinder is 10 times the wavelength the norm of the scattered field in the backscattering direction is less than 2% of the norm of the scattered field from the non-cloaked cylinder.

The outlined optimization procedure can equivalently be used in the H_z -polarized case. However, it turns out that the optimized structures for this polarization converge to those of the E_z -polarization case for large cylinder radii ($R_{PEC} > 10\lambda$) and hence also towards the simple quarter-wavelength Bragg grating. Hence, the cloak optimized for an E_z -polarized wave is also very efficient when illuminated by a H_z -polarized wave as shown in Fig. 4(c).

The angle interval ($\pm 10^\circ$) is chosen somewhat arbitrarily. If the requirement to the size of the angle interval is relaxed, one can get even better cloaking performance in the smaller angular interval. The radar cross section for the non-cloaked cylinder (solid red) and the optimized 6-layer structure (solid blue) from Fig. 4 for an E_z -polarized wave are presented in Fig. 5. The 6-layer structure from Fig. 4 minimizes the norm of the scattered field in the angle interval $\pm 10^\circ$, however, minimizing the norm in the reduced angle interval $\pm 2^\circ$ results in a significantly stronger reduction of the backscattering in the reduced angular range.

In conclusion, we have shown that the backscattering from a PEC cylinder illuminated by a plane wave can be minimized by wrapping the cylinder in a cloak composed of annular rings made of non-absorbing, low-contrast, dielectric material readily available in nature. This concept constitutes a new application for annular Bragg gratings, which amplify and couples the incoming field into confined ring-modes, which lead the wave around the obstacle hence reducing backscattering. Cloaking performance can be improved by increasing the number of rings wrapped around the PEC cylinder and/or increasing the permittivity of the high index material. For small obstacle to wavelength ratios the cloak must be optimized independently for E_z and H_z -polarized waves, however, for larger ratios (i.e. $R_{PEC}/\lambda > 10$), optimized structures converge towards simple quarter-wavelength annular Bragg gratings. Due to the polarization independence for larger obstacles we predict that the concept is extendable to the backscattering minimization of 3D coated spheres as well.

Finally, it is worthwhile emphasizing that the proposed annular structure is different from the onion-ring cloaks previously proposed in the literature (cf. Refs. 20 and 21) since these are not directly manufacturable from standard available materials but require special tailored anisotropic micro structures with periodicity much smaller than the wavelength of the incoming wave and abnormal material parameters less than unity. Along the same line of thought it should also be noted that the proposed annular Bragg structure cannot be found using a transformation optics approach since it relies on structural details at the same scale as the incoming waves.

Apart from minimizing the backscattering from smaller objects the findings of this paper may be of interest for other design problems where scattering by particles is involved, such as design of solar panels, color

coatings and sun screens.

This work was supported by the Villum Foundation (the NextTop project) and the Danish Research Council for Technology and Production (Grant No. 274-06-0507).

-
- [1] J. B. Pendry, D. Schurig, and D. R. Smith, *Science* **312**, 1780 (2006).
- [2] U. Leonhardt, *Science* **312**, 1777 (2006).
- [3] Y. Lai, H. Y. Chen, Z.-Q. Zhang and C. T. Chan, *Phys. Rev. Lett.* **102**, 093901 (2009).
- [4] W. W. Salisbury, U.S. Patent 2 599 944, June 10 (1952)
- [5] R. L. Fante and M. T. McCormack, *IEEE Trans. Antennas Propag.* **36**, 1443 (1988)
- [6] J. J. Bowman and V. H. Weston, *IEEE Trans. Antennas Propag.* **14**, 760 (1966)
- [7] E. F. Knott and K. B. Langseth, *IEEE Trans. Antennas Propag.* **28**, 137 (1980)
- [8] J. Li and J. B. Pendry, *Phys. Rev. Lett.* **101**, 203901 (2008).
- [9] J. Valentine, J. Li, T. Zhengraf, G. Bartal, and X. Zhang, *Nat. Mater.* **8**, 568 (2009).
- [10] T. Ergin, N. Stenger, P. Brenner, J. B. Pendry and M. Wegener, *Science* **328**, 337 (2010).
- [11] J. Zhang, L. Liu, Y. Luo, S. Zhang and N. A. Mortensen, *Opt. Express* **19**, 8625 (2011).
- [12] J. Andkjær and O. Sigmund, *Appl. Phys. Lett.* **98**, 021112 (2011).
- [13] M. P. Bendsøe and O. Sigmund, *Topology Optimization: Theory, Methods and Applications* (Springer-Verlag, Berlin, 2003).
- [14] J. Scheuer and A. Yariv, *J. Opt. Soc. Am. B* **20**, 2285 (2003)
- [15] A. W. Adey, *Can. J. Phys.* **34**, 510 (1956)
- [16] C. C. H. Tang, *J. Appl. Phys.* **28**, 628 (1957)
- [17] M. Kerker and E. Matijevic, *J. Opt. Soc. Am.* **51**, 506 (1961)
- [18] H. E. Bussey and J. H. Richmond, *IEEE Trans. Antennas Propag.* **14**, 723 (1975)
- [19] M. A. Kaliteevski, R. A. Abram, V. V. Nikolaev and G. S. Sokolovski, *J. Mod. Opt.* **46**, 875 (1999)
- [20] B.-I. Popa and S. A. Cummer, *Phys. Rev. A* **79**, 023806 (2009).
- [21] C. W. Qiu, L. Hu, B. Zhang, B.-I. Wu, S. G. Johnson and J. D. Joannopoulos, *Opt. Express* **17**, 13467 (2009)

Publication [P5]

Topology optimization of grating couplers
for the efficient excitation of surface
plasmons

Topology optimization of grating couplers for the efficient excitation of surface plasmons

Jacob Andkjær,^{1,*} Shinji Nishiwaki,² Tsuyoshi Nomura,³ and Ole Sigmund¹

¹Department of Mechanical Engineering, Technical University of Denmark, Nils Koppels Alle, Building 404, 2800 Kgs. Lyngby, Denmark

²Department of Mechanical Engineering and Science, Kyoto University, Kyoto 606-8501, Japan

³Toyota Central R&D Laboratories Inc., Aichi 480-1192, Japan

*Corresponding author: jban@mek.dtu.dk

Received June 15, 2010; accepted June 26, 2010;
posted July 7, 2010 (Doc. ID 130211); published August 18, 2010

We propose a methodology for a systematic design of grating couplers for efficient excitation of surface plasmons at metal–dielectric interfaces. The methodology is based on a two-dimensional topology optimization formulation based on the H -polarized scalar Helmholtz equation and finite-element method simulations. The efficiency of the method is demonstrated by optimized designs for input and output grating couplers for an Ag-SiO₂ interface. The results indicate that slanted groove gratings may raise the coupling efficiency above 68% where the highest previously reported value was 50%. © 2010 Optical Society of America
OCIS codes: 240.6680, 050.1590, 050.2770.

1. INTRODUCTION

Surface plasmons are electromagnetic waves trapped at the interface between a metal with a negative real part and a dielectric with a positive real part of the permittivity [1]. Surface plasmonic effects may be used in the realization of pure photonic circuits which potentially will be much faster than electronic circuits, in the lighting industries for light-emitting diodes or organic light-emitting diodes [2,3] and in solar cells [4]. Common for all applications is the problem of efficient coupling of light into the surface plasmon or vice versa. For more detailed overviews of surface plasmonic effects see [5,6].

Surface plasmons can be excited by electrons or photons. In this work we use photons in the form of a light beam directed toward the interface between a dielectric material and a metal. The incoming photons are scattered and transfer momentum to the nearly free electrons of the metals. With the right coupling, the nearly free electrons of the conductor will collectively oscillate in resonance with the incoming beam. This causes the light to be trapped at the interface and form a plasma oscillation in the optical frequency range. Figure 1 shows the theoretically predicted electromagnetic field for a surface plasmon. The nearly free electrons oscillate in resonance with the incoming light and the “+” and “−” regions represent regions with low and high surface charge densities, respectively. The magnitude of the electric field E is higher in the dielectric than in the metal due to the energy dissipation in the metal. The electric field oscillates in the (x,y) -plane making the surface plasmons transverse magnetic in character; hence the magnetic field H_z is given in the z -direction.

Efficient coupling of light into the interface is crucial. Common methods for coupling light into a surface plasmon are based on prism couplers (e.g., Kretschmann and Otto configuration) or grating couplers [1]. On small

scales the use of a prism is impractical, which motivates the use of grating couplers. A grating coupler comprises a topology that enables a wave vector match between the incident light and the surface plasmon, without the use of a prism. The topology of these grating couplers can be designed in many ways and the design has a big influence on the efficiency of the coupling. This leads to the use of optimization techniques for finding the most optimal design. Three decades ago Tamir and Peng [7] performed analytical as well as simple numerical studies on the effect of different groove designs on the coupling efficiency. Other contributions have been presented in [8–10], and lately Lu *et al.* [11] performed a systematic optimization of coupling into a surface plasmon. Using a hierarchical search optimization algorithm, varying the width and position of 14 grooves the authors achieved an excitation efficiency of 50%, which is the highest efficiency reported in the literature for a grating coupler. In the present paper we extend the work of Lu *et al.* [11] to allow free shapes and topologies of the grooves and we study not only the case of coupling into the plasmon but also the coupling of light from the plasmon into the dielectric surroundings. By increasing the design freedom using the topology optimization method we manage to improve the coupling efficiency from 50% reported by Lu *et al.* [11] to more than 68% which is obtained for a coupling topology with slanted grooves.

Topology optimization is a computational tool that optimizes material distribution for a given objective function with geometrical and/or physical constraints [12]. The concept was introduced more than two decades ago in [13] for structural mechanics, but the method has later been used to tailor new materials or mechanisms in various fields of engineering such as fluid dynamics (e.g., [14]), micro-electro-mechanical systems (e.g., [15]), photonics (e.g., [16]), and multiphysics problems (e.g., [17]). Us-

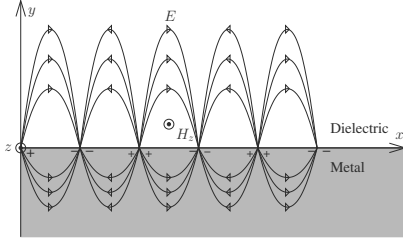


Fig. 1. A surface plasmon induced in the interface between a metal and a dielectric. + and - signs represent regions with low and high surface charge densities, respectively. The electric field E oscillates in the (x,y) -plane making the surface plasmons transverse magnetic in character (hence magnetic field H_z in the z -direction).

ing topology optimization it is possible to find solutions that are not easily found by intuition, such as materials with negative Poisson's ratio [18] and negative thermal expansion coefficient [19]. Thus topology optimization is a suitable method to use in order to design grating couplers for the efficient excitation of surface plasmons.

The layout of the paper is as follows. Section 2 summarizes the theory behind modeling topology optimization of surface plasmonic problems. Optimized designs of grating couplers are presented in Section 3 and conclusions are given in Section 4.

2. TOPOLOGY OPTIMIZATION OF TWO-DIMENSIONAL SURFACE PLASMON GRATING COUPLERS

The implementation of the two-dimensional topology optimization problem is based on the finite-element method using a combination of the commercial programs COMSOL 3.4 and MATLAB 7.5.0 (R2007b). We use the material and geometry settings from [11]. The computational models for the input and output couplers are presented in Figs. 2(a) and 2(b), respectively. Both models consist of a SiO_2 -domain, Ω_{SiO_2} ; an Ag-domain, Ω_{Ag} ; and a design domain, Ω_{des} , where SiO and Ag shall be distributed freely. The design domain Ω_{des} has a width and height of $2.5 \mu\text{m}$ and 50 nm , respectively. For the input coupler a time-harmonic wave is excited at Γ_{inp} with a free-space wavelength of 476 nm . The wave is Gaussian shaped with a

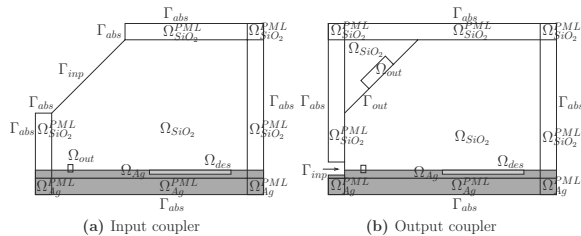


Fig. 2. Computational models for the input and output couplers containing a dielectric (Ω_{SiO_2}), a metal (Ω_{Ag}), and a design domain (Ω_{des}). A plane wave is excited at Γ_{inp} . A surface plasmon will be induced in the interface between the two media and the energy flux is measured in the domain Ω_{out} . To avoid reflections from the boundaries, PML domains (Ω^{PML}) and absorbing boundary condition Γ_{abs} have been introduced. All interior boundaries have continuous boundary condition.

full width at half-maximum (FWHM) = $1 \mu\text{m}$ and has an incident angle of 45° . For the output grating coupler the surface plasmon is excited at Γ_{inp} with an exponentially shaped electromagnetic wave matching the skin depth. For both cases, the permittivities of SiO_2 and Ag corresponding to the given wavelength are $\epsilon_r = 2.25$ and $\epsilon_r = -7.06 - i0.27$, respectively, and the permeability is assumed to be $\mu_r = 1$ for both materials. For the input coupler the incident beam will induce a surface plasmon at the Ag- SiO_2 interface when the wave vectors match due to the grating coupler and vice versa for the output coupler. The power flux of the surface plasmon is measured using the averaged Poynting vector in the domain Ω_{out} . Reflections from the boundaries are eliminated using perfectly matched layers (PMLs) [20]. Furthermore, absorbing boundary conditions Γ_{abs} have been introduced on all outer boundaries.

A. Governing Equation

The wave propagation problem is governed by the H -polarized scalar Helmholtz equation,

$$\nabla \cdot (\epsilon_r^{-1} \nabla H_z(\mathbf{r})) + k_0^2 H_z(\mathbf{r}) = 0 \quad \text{in } \Omega, \quad (1)$$

$$\frac{\partial}{\partial x} \left(\frac{s_y}{s_x} \epsilon_r^{-1} \frac{\partial H_z(\mathbf{r})}{\partial x} \right) + \frac{\partial}{\partial y} \left(\frac{s_x}{s_y} \epsilon_r^{-1} \frac{\partial H_z(\mathbf{r})}{\partial y} \right) + s_x s_y k_0^2 H_z(\mathbf{r}) = 0 \quad \text{in } \Omega^{\text{PML}}, \quad (2)$$

where $k_0 = \omega/c$ is the free-space wave number, ω is the angular frequency, c is the speed of light in vacuum, $H_z(\mathbf{r})$ is the unknown magnetic field in the plane $\mathbf{r} = (x, y)$, and s_x and s_y are complex functions of the position and govern the damping properties of the PML.

The boundary conditions are specified for both problems as

$$\mathbf{n} \cdot (\epsilon_r^{-1} \nabla H_z(\mathbf{r})) = 0 \quad \text{on } \Gamma_{\text{con}}, \quad (3)$$

$$\mathbf{n} \cdot (\epsilon_r^{-1} \nabla H_z(\mathbf{r})) + ik_0 \sqrt{\epsilon_r^{-1}} H_z = 0 \quad \text{on } \Gamma_{\text{abs}}, \quad (4)$$

where $i = \sqrt{-1}$ and \mathbf{n} is the outward-pointing normal vector. The boundary condition for the input coupler with the Gaussian shaped beam is

$$\mathbf{n} \cdot (\epsilon_r^{-1} \nabla H_z(\mathbf{r})) = ik_0 \sqrt{\epsilon_r^{-1}} \left[2 \exp \left(-\frac{(x-x_0)^2}{2 \left(\frac{1}{\sqrt{2}} \sigma \right)^2} \right) H_0 - H_z \right] \quad \text{on } \Gamma_{\text{inp}}, \quad (5)$$

where x_0 is the x -coordinate at the center of Γ_{inp} , $\sigma = \text{FWHM}/[2\sqrt{2} \log 2]$, and H_0 is the incident magnetic field amplitude. For the output coupler the boundary condition is modeled with an exponentially shaped field, using knowledge of the skin depth and the vertical wave vector $k_{y,\text{Ag}}$ in the silver,

$$\mathbf{n} \cdot (\epsilon_r^{-1} \nabla H_z(\mathbf{r})) = ik_0 \sqrt{\epsilon_r^{-1}} [2 \exp(-|k_{y,\text{Ag}}||y_0 - y|) H_0 - H_z] \text{ on } \Gamma_{\text{inp}}, \quad (6)$$

where $k_{y,\text{Ag}}$ is found analytically to be $13.5 \times 10^6 \text{ m}^{-1}$ and y_0 is the y -coordinate of the interface.

B. Design Variables, Material Interpolation, and Design Field

Following the standard topology optimization approach, the material distribution in the design domain Ω_{des} can be changed by varying the permittivity of individual finite elements continuously between the material values for SiO_2 and Ag. The design variables are relative element material densities $\rho_e \in [0; 1]$, where $\rho_e = 0$ corresponds to Ag and $\rho_e = 1$ corresponds to SiO_2 . The following interpolation models the relation between element densities and element permittivities:

$$\epsilon_r(\rho_e) = \epsilon'_{\text{Ag}} + \rho_e(\epsilon'_{\text{SiO}_2} - \epsilon'_{\text{Ag}}) - i[\epsilon''_{\text{Ag}} + \rho_e(\epsilon''_{\text{SiO}_2} - \epsilon''_{\text{Ag}})] + i4d(\rho_e^2 - \rho_e), \quad (7)$$

where ' and '' , respectively, denote the real and the imaginary parts of the permittivity for the given material and d is a factor introducing artificial damping. This damping induces an energy loss for intermediate values of ρ and disfavors non-discrete (0/1) values in the final design [21]. Remark that the continuous design variables are introduced in order to be able to use efficient gradient-based math-programming methods for solving the optimization problem, in turn assuring convergence within a couple of hundred finite-element analyses.

To ensure manufacturable and mesh independent designs we use image processing-based filtering techniques. An overview of different filtering techniques is presented in [22] but in this work we use the latest Guest filter [23] which ensures a minimum length scale for both the silica and the silver phases. This means that regions with silica or silver cannot become smaller than the chosen filter size. Thus the designs can be tailored to meet manufacturing criteria. We denote the filtered design variables by $\bar{\rho}_e$.

C. Objective Function and Optimization Problem

The goal of the optimization problem is to maximize the averaged Poynting vector (power flow) in Ω_{out} in the negative direction of the x -axis, $\mathbf{n} = (-1, 0)$, for the input coupler and in the beam direction, $\mathbf{n} = (-\sqrt{2}/2, \sqrt{2}/2)$, for the output coupler. The gradient-based optimization routine method of moving asymptotes (MMA) [24] is applied to update the design variables in an iterative approach until convergence. A volume constraint is added to the optimization problem, not because we want to limit the usage of one material, but to avoid excess islands of material and ensure a cleaner final design. Thus the optimization problem is formulated as

$$\max_{\bar{\rho}} \Phi(H_z(\bar{\rho})) = P_{\text{out}} = \int_{\Omega_{\text{out}}} \frac{1}{2L_x \epsilon_0 \omega} \Re(i \epsilon_r^{-1} H_z^* \nabla H_z) \cdot \mathbf{n} d\mathbf{r},$$

s. t. Helmholtz equation (8)

Boundary conditions

$$\frac{1}{V_{\Omega_{\text{des}}}} \int_{\Omega_{\text{des}}} \bar{\rho}(\mathbf{r}) d\mathbf{r} - \beta \leq 0, \quad 0 \leq \rho(\mathbf{r}) \leq 1,$$

where * denotes complex conjugate, P_{out} is the averaged power flow through Ω_{out} , L_x is the width of Ω_{out} , \mathbf{n} gives the direction of the power flux, $\Re(\cdot)$ is the real part, $V_{\Omega_{\text{des}}}$ is the total volume of Ω_{des} , and β is the maximum allowed volume fraction of SiO_2 .

D. Efficiency

The decay length of the surface plasmon and its skin depth in the two materials are used to evaluate the power flux of the surface plasmon perpendicular to the interface at the first groove of the grating. The electric field of the surface plasmon along the interface decreases with the distance $|x|$ to the grating as $\exp(-2k''_{x,\text{SP}}|x|)$, where $k''_{x,\text{SP}}$ is the imaginary part of the surface plasmon wave vector along the interface and can be derived analytically to $k''_{x,\text{SP}} = 214.6 \times 10^3 \text{ m}^{-1}$ for this problem. At the decay length, $\delta_{\text{SP}} = 2.33 \times 10^{-6} \text{ m}$, the electric field has decreased by a factor of $\exp(-1)$. Thus the horizontal center of the output domain Ω_{out} is positioned exactly at the decay length of the surface plasmon, and hence P_{out} should be divided by the factor $\exp(-1)$ in order to find the power flow at the first groove of the grating. Likewise the electric field of the surface plasmon normal to the interface decays with the distance $|y|$ as $\exp(-|k_y||y|)$, where k_y is the real part of the surface plasmon wave vector perpendicular to the interface. The wave vector is dependent on the material in which it propagates; thus the wave vectors are analytically found to be $k_{y,\text{Ag}} = 42.5 \times 10^6 \text{ m}^{-1}$ and $k_{y,\text{SiO}_2} = 13.5 \times 10^6 \text{ m}^{-1}$, and thus the skin depths become $\delta_{\text{Ag}} = 23.5 \times 10^{-9} \text{ m}$ and $\delta_{\text{SiO}_2} = 73.9 \times 10^{-9} \text{ m}$. The height of the output domain Ω_{out} is set to the skin depth in the two materials, and thus the power flow through an infinite line perpendicular to the interface can be found as $P_{\text{out}}/[1 - \exp(-1)]$. For the input coupler the efficiency of the coupling is found as the power flux of the surface plasmon at the first groove of the grating divided by the power flux at the input boundary Γ_{inp} ,

$$\text{Efficiency} = \frac{P_{\text{out}}}{\exp(-1)[1 - \exp(-1)]P_{\text{inp}}}. \quad (9)$$

To avoid reflections from the incident beam on the silver surface, the power flow at the input, P_{inp} , boundary is found when all domains are set to silica.

In the reverse case (output coupler) the efficiency is found as the power flow through the line parallel to the output domain Ω_{out} divided by the power flux of the surface plasmon at the first groove of the grating. In order to find the power flow of the surface plasmon at the first grating, we use the power flow at the input boundary and the distance L_{SP} from the boundary to the first grating to calculate the decrease in the electric field due to energy dissipation along the interface,

$$\text{Efficiency} = \frac{P_{\text{out}}}{\exp(-2k''_{x,\text{SP}}L_{\text{SP}})P_{\text{inp}}}, \quad (10)$$

where P_{inp} and P_{out} are evaluated at Γ_{inp} and Γ_{out} , respectively.

E. Discretization

The modeling problem is solved using the finite-element method; thus the discretized set of equations can be written in the form

$$\mathbf{S}(\rho)\mathbf{u} = \mathbf{f}, \quad (11)$$

where $\mathbf{S}(\rho)$ is the system matrix (which directly depends on the density variables), \mathbf{u} is the state field, and \mathbf{f} is the load vector. The design domain Ω_{des} is discretized using 500,000 bi-linear quadrilateral elements and the rest of the domains are discretized using triangular linear elements with a maximum length of 25 nm. This yields a total of 680,842 elements in the input coupler case and 696,172 elements in the output coupler case, and the design elements have a side length of 0.5 nm. This rather fine resolution is not strictly required from convergence considerations; however, we have chosen this fine discretization in order to be able to reproduce the grating coupler from [11] using a regular element division. The state field \mathbf{u} is given by continuous elements, whereas the design field is modeled using piecewise constant elements in order to obtain sharp material boundaries at interfaces.

F. Sensitivity Analysis

The adjoint method is used in order to find the sensitivities for the gradient-based optimization algorithm, MMA. The sensitivities for a discretized problem in the form of Eq. (11) with the objective function Φ are given in [21] as

$$\frac{d\Phi}{d\tilde{\rho}_e} = \frac{\partial\Phi}{\partial\tilde{\rho}_e} + 2\Re\left[\boldsymbol{\lambda}^T\left(\frac{\partial\mathbf{S}}{\partial\tilde{\rho}_e}\mathbf{u} - \frac{\partial\mathbf{f}}{\partial\tilde{\rho}_e}\right)\right], \quad (12)$$

where the adjoint vector $\boldsymbol{\lambda}$ is obtained from the solution of the adjoint problem

$$\mathbf{S}^T\boldsymbol{\lambda} = -\frac{\partial\Phi}{\partial\mathbf{u}}. \quad (13)$$

The rightmost term of Eq. (12) is zero due to the design domain not being a part of the output domain. The terms $\partial\mathbf{S}/\partial\tilde{\rho}_e$ and $\partial\mathbf{f}/\partial\tilde{\rho}_e$ are known as part of the direct solution of Eq. (11). For the present finite-element problem the system matrix \mathbf{S} is symmetric and hence the solution of the adjoint problem in Eq. (13) can be performed very efficiently by the reuse of the factorization of \mathbf{S} computed for the direct analysis stated in Eq. (11). To summarize, this means that the computational costs associated with obtaining the sensitivities is ignorable compared to the solution of the original problem in Eq. (11). For simplification we use the notation $A = 1/(2L_x\epsilon_0\omega)\Re(i\epsilon_r^{-1}\mathbf{u}^*\nabla\mathbf{u})\cdot\mathbf{n}$. Thus the derivatives with respect to the state variables, $\partial\Phi/\partial\mathbf{u}$, can then be found by the chain rule to be

$$\frac{\partial\Phi}{\partial\mathbf{u}} = \int_{\Omega_{\text{out}}} \left(\frac{\partial A}{\partial\mathbf{u}} + \frac{\partial A}{\partial\nabla\mathbf{u}} \cdot \nabla \right) d\mathbf{r}, \quad (14)$$

where

$$\frac{\partial A}{\partial\mathbf{u}} = \frac{-1}{4L_x\epsilon_0\omega} i\epsilon_r^{-1} \nabla\mathbf{u}^* \cdot \mathbf{n}, \quad (15)$$

$$\frac{\partial A}{\partial\nabla\mathbf{u}} = \frac{1}{4L_x\epsilon_0\omega} i\epsilon_r^{-1} \mathbf{u}^* \cdot \mathbf{n}. \quad (16)$$

G. Algorithm

The overall optimization algorithm is described in a simplified pseudocode in [22]. We stop the optimization when the maximum difference of the densities in two iterations is less than 1% or 1000 iterations are reached. The regularization filter [23] will lead to designs with a small transition area of intermediate densities. Such designs are non-realizable; hence all densities lower than 0.9 are set to zero and the rest of the densities are set to 1 after convergence, in order to obtain discrete (0/1) designs. This step also ensures that the artificial damping, introduced in Eq. (7), does not contribute to the final computation of the problem in order to get the final efficiency.

3. RESULTS

We use an initial guess of pure silver in the design domain Ω_{des} , which is shown in Fig. 3(a) with length scales. For both input and output coupler cases we impose a volume fraction constraint on the silica of 0.3 and the minimum length scales are set to 5 nm for both material phases. The optimized designs for the input and output couplers obtained using the described methodology are presented in Figs. 3(b) and 3(c), respectively. For the purpose of comparison we have presented the grating coupler from [11] in Fig. 3(d).

The optimized design for the input coupler consists of 13 inclined grooves of increasing width and decreasing depth. The optimized design represents an efficiency of 68.7% which is a approximately a factor of 0.4 higher than the efficiency of the grating coupler from [11]. The optimized design of the output coupler is very similar to the optimized design of the input coupler. The output coupler has an extra groove at the right side of the design domain resulting in a total of 14 inclining grooves, the same number as the grating coupler from [11]. The 14th groove is also found in the design of the input coupler at intermediate steps in the optimization loop, but it disappears in later steps. The manufacturability of the optimized designs may be ensured by choosing appropriate minimum length scales. The designs presented here are shown as specific solutions; however, the general concept of the improved efficiency by inclined grooves may inspire future realizations of efficient grating couplers. Figure 4 shows the absolute magnetic fields of the optimized designs for

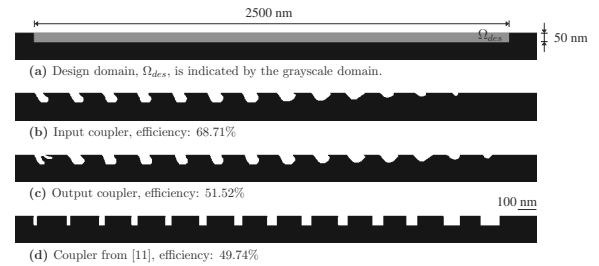


Fig. 3. Optimized designs.

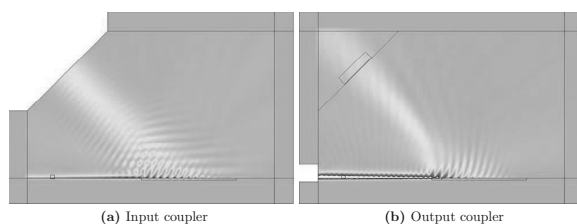


Fig. 4. (Color online) FE simulations showing the absolute magnetic field for the optimized designs.

the input and output couplers. At the end we note that the optimized output coupler is indeed better than the reversed input coupler. Equal topologies for the two cases are not expected due to different loss mechanisms in the incoming and outgoing wave cases.

4. CONCLUSION

This paper proves that the topology optimization method can be applied to the design of nano-phonic grating couplers. Results indicate that efficiencies beyond 68% are possible for slanted groove-based gratings. The highest reported efficiency for vertical groves is 50%. The big improvement may warrant the development of improved manufacturing technologies that allow slanted groves. Future work may include topology optimization of grating couplers for frequency ranges and variable input wave directions, which will ensure more robust but probably less efficient gratings.

ACKNOWLEDGMENTS

This work is supported from a Eurohorcs/ESF European Young Investigator Award [25] through the grant "Synthesis and topology optimization of optomechanical systems" and from the Danish Research Council for Technology and Production through the grant "Topology Optimization of Electromagnetic Metamaterials for Miniaturization of Wireless Communication Antennas" [26]. Fruitful discussions with members of the TopOpt-group [27] are also gratefully acknowledged.

REFERENCES

1. H. Raether, *Surface Plasmons on Smooth and Rough Surfaces and on Gratings* (Springer-Verlag, 1988).
2. W. L. Barnes, "Turning the tables on surface plasmons," *Nature Mater.* **3**, 588–589 (2004).
3. P. A. Hobson, J. A. E. Wasey, I. Sage, and W. L. Barnes, "The role of surface plasmons in organic light-emitting diodes," *IEEE J. Quantum Electron.* **8**, 378–386 (2002).
4. V. E. Ferry, L. A. Sweatlock, D. Pacifici, and H. A. Atwater, "Plasmonic nanostructure design for efficient light coupling into solar cells," *Nano Lett.* **8**, 4391–4397 (2008).
5. H. A. Atwater, "The promise of plasmonics," *Sci. Am.* **296**, 56–63 (2007).
6. W. L. Barnes, A. Dereux, and T. W. Ebbesen, "Surface plasmon subwavelength optics," *Nature* **424**, 824–830 (2003).
7. T. Tamir and S. T. Peng, "Analysis and design of grating couplers," *Appl. Phys.* **14**, 235–254 (1977).
8. C. Peng and W. A. Challener, "Input-grating couplers for narrow Gaussian beam: influence of groove depth," *Opt. Express* **12**, 6481–6490 (2004).
9. G. Leveque and O. J. F. Martin, "Numerical study and optimization of a diffraction grating for surface plasmon excitation," *Proc. SPIE* **5927**, 246–254 (2005).
10. Y. Huang, "Optimal design for the grating coupler of surface plasmons," in *Proceedings of the COMSOL Conference* (2008), 4980 <http://www.comsol.com/papers/4980>.
11. J. Lu, C. Petre, E. Yablonovitch, and J. Conway, "Numerical optimization of a grating coupler for the efficient excitation of surface plasmons at an Ag-SiO₂ interface," *J. Opt. Soc. Am. B* **24**, 2268–2272 (2007).
12. M. P. Bendsøe and O. Sigmund, *Topology Optimization: Theory, Methods and Applications* (Springer-Verlag, 2003).
13. M. P. Bendsøe and N. Kikuchi, "Generating optimal topologies in optimal design using a homogenization method," *Comput. Methods Appl. Mech. Eng.* **71**, 197–224 (1988).
14. T. Borrvall and J. Petersson, "Topology optimization of fluids in Stokes flow," *Int. J. Numer. Methods Fluids* **41**, 77–107 (2003).
15. J. Jonsmann, O. Sigmund, and S. Bouwstra, "Compliant thermal microactuators," *Sens. Actuators, A* **76**, 463–469 (1999).
16. P. I. Borel, A. Harpøth, L. H. Frandsen, M. Kristensen, J. S. Jensen, P. Shi, and O. Sigmund, "Topology optimization and fabrication of photonic crystal structures," *Opt. Express* **12**, 1996–2001 (2004).
17. O. Sigmund, "Design of multiphysics actuators using topology optimization—Part I: One-material Structures," *Comput. Methods Appl. Mech. Eng.* **190**, 6577–6604 (2001).
18. U. D. Larsen, O. Sigmund, and S. Bouwstra, "Design and fabrication of compliant mechanisms and material structures with negative Poisson's ratio," *J. Microelectromech. Syst.* **6**, 99–106 (1997).
19. O. Sigmund and S. Torquato, "Composites with extremal thermal expansion coefficients," *Appl. Phys. Lett.* **69**, 3203–3205 (1996).
20. M. Koshiba, Y. Tsuji, and S. Sasaki, "High-performance absorbing boundary conditions for photonic crystal waveguide simulations," *IEEE Microw. Wireless Compon. Lett.* **11**, 152–154 (2001).
21. J. S. Jensen and O. Sigmund, "Topology optimization of photonic crystal structures: a high-bandwidth low-loss T-junction waveguide," *J. Opt. Soc. Am. B* **22**, 1191–1198 (2005).
22. O. Sigmund, "Morphology-based black and white filters for topology optimization," *Struct. Multidiscip. Optim.* **33**, 401–424 (2007).
23. J. K. Guest, "Topology optimization with multiple phase projection," *Comput. Methods Appl. Mech. Eng.* **199**, 123–135 (2009).
24. K. Svanberg, "A class of globally convergent optimization methods based on conservative convex separable approximations," *SIAM J. Optim.* **12**, 555–573 (2002).
25. EURYI, <http://www.esf.org/euryi>.
26. TopAnt, <http://www.topant.dtu.dk>.
27. <http://www.topopt.dtu.dk>.

Publication [P6]

Topology optimized Fresnel zone plate
lenses

Topology optimized half-opaque Fresnel zone plate lenses

Jacob Andkjær,^{1, a)} Ole Sigmund,¹ Shinji Nishiwaki,² and Tsuyoshi Nomura³

¹⁾ *Technical University of Denmark, Department of Mechanical Engineering, 2800 Kgs. Lyngby, Denmark*

²⁾ *Department of Mechanical Engineering and Science, Kyoto University, Kyoto 606-8501, Japan*

³⁾ *Toyota Central R&D Laboratories Inc., Aichi 480-1192, Japan*

(Dated: 1 February 2012)

(Lorem ipsum dolor sit amet pede feugiat nibh enim pharetra sit pulvinar non vel amet tincidunt id est eget vestibulum integer non varius quisque bibendum quis justo viverra inceptos sapien nulla egestas aenean in quisque fringilla nec integer faucibus a in neque nulla blandit amet ipsum tellus sollicitudin pretium porttitor sapien sollicitudin est magnis molestie dui integer scelerisque sed dui aliquam ultricies ante justo porta condimentum quam nec at suscipit est aptent metus in dui facilisi aliquet odio nibh elit id purus donec lorem vitae lectus vitae ac laoreet felis arcu magna eu pellentesque magna risus.)

The concept of Fresnel zone plate (FZP) lenses was developed more than a century ago in the pioneering work by Fresnel, Lord Rayleigh, Soret and Wood¹. FZP lenses work by means of diffraction instead of refraction and reflection and can be divided into two types, half-opaque FZPs and phase-correcting FZPs. The first type is built of alternating transparent and opaque concentric rings to block out alternating Fresnel zones, whereas the latter type is constructed to correct phases in various zones by varying the dielectric constant or the depth of the profile.

Refractive optics cease to be effective for wavelengths shorter than the visible spectrum until the hard X-ray region², because solids in this spectrum are strongly absorbing. Half opaque FZPs, however, have been shown to work well in this spectrum³. Further, FZPs in general are desirable as focusing devices due to their simplicity of design, easy fabrication and low cost. FZP concepts have spurred the development of photon sieves⁴ for work with soft X-rays, which have achieved sharper image formation by distributing pinholes over the Fresnel zones.

A disadvantage of the half-opaque FZP lens type is that approximately half the energy of the incident wave is lost, due to the opaque zones, resulting in low aperture efficiency. This shortcoming can to some extent be remedied by combining several zone plate structures as a layered FZP^{5,6} or by using a reflector based FZP⁷.

Several design methodologies have been developed to give the FZP special features such as designing dual-band FZPs⁸, bifocal FZPs⁹ and non-planar shaped FZPs⁷. Furthermore, the spatial distribution of either opaque material (for half-opaque FZPs) or dielectric material (for phase-correcting FZPs) calls for an optimization technique and several optimization methodologies have been reported¹⁰⁻¹² using search algorithms in the two first cited references and a genetic algorithm in the latter. Thus there is no lack of methodologies for designing FZPs, however, none has yet given a methodology that can handle a broad spectrum of features in one combined

approach.

We will, in this work, show that efficient half-opaque FZP lenses can be designed using gradient-based topology optimization¹³ and optimized examples of single layer, multiple layer, broad-band, multiple foci, reflector-based and convex-shaped FZPs are presented to show the strength and versatility of this new design methodology.

A planar FZP lens is traditionally designed using a simple formula derived from geometric-optics¹⁴

$$r_n = \sqrt{\frac{2nf\lambda}{P} + \left(\frac{n\lambda}{P}\right)^2} \quad (1)$$

where r_n is the radius from the focal axis to the outer edge of the n 'th zone, n is the zone number, f is the focal length, λ is the wave-length and P is the number of phase corrections ($P = 2$ for a half-opaque FZP). However, Eq. 1 is not optimal and a more efficient design is achieved by compressing the zone plate radially using a scalar coefficient k less than unity $r_n^{new} = k r_n$ where $k = 0.98$ was found to yield a higher efficiency for the half-opaque FZP⁷. This motivates us to develop an optimization technique that can find optimized designs that take into account the spatial position of the opaque rings.

The wave incident on the FZP is given as an E_z -polarized plane wave. The wave problem is governed by Maxwell's equation in time-harmonic form and can be reformulated into a scalar Helmholtz equation for the E_z -polarized wave in free-space. We choose to solve the boundary value problem using the finite element method (FEM)^{15,16}. A scattered-field formulation is used in order to reduce the dispersion error. The infinite domain is truncated by a Perfectly Matched Layer (PML) domain backed up by a first order absorbing boundary condition (ABS)¹⁵ as an approximation to the Sommerfeld radiation condition. The opaque rings of the FZP can be modeled as perfect electrically conducting (PEC) boundaries.

The idea of the presented optimization algorithm is to be able to continuously vary, between full transmission and opacity in each element at a design boundary. To do so, the design boundary is modeled by a transition

^{a)} Electronic mail: jban@mek.dtu.dk

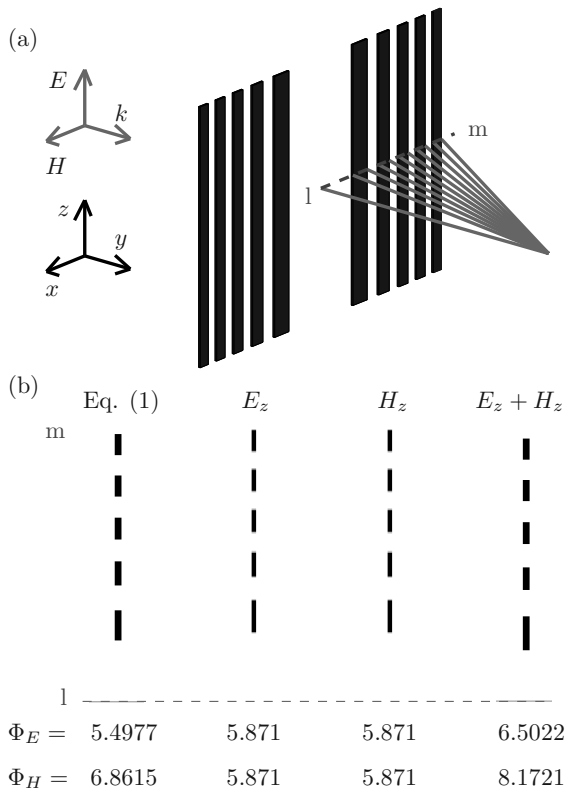


FIG. 1. Computational Domain.

boundary condition⁷ for an E_z or H_z polarized wave, which respectively can be formulated as

$$\eta \mathbf{n} \times (\mathbf{H}_1 - \mathbf{H}_2) + E_z = 0 \quad (2)$$

$$\eta \mathbf{n} \times (\mathbf{E}_1 - \mathbf{E}_2) + \mathbf{n} \times \mathbf{E}_1 = 0 \quad (3)$$

where η is the surface impedance. When $\eta \rightarrow \infty$ Eq. 2 and 3 mimic full transmission and when $\eta = 0$ Eq. 2 and 3 is equivalent to the PEC condition (opaque). This property of the transition boundary conditions can be exploited in the topology optimization approach using a density method¹³. A design variable, $\rho_e \in [0; 1]$, for each boundary element is introduced as a relative element material density in order to interpolate between opacity and full transmission mimicked by $\eta^{min} = 10^{-2}$ and $\eta^{max} = 10^6$, respectively. Due to the big difference in orders of magnitude, a power interpolation function¹⁷ is used

$$\eta_e(\rho_e) = 10^{\log_{10}(\eta^{min})\rho_e + \log_{10}(\eta^{max})(1-\rho_e)} \quad (4)$$

A density filter^{18–20} is introduced to aid realizations of the optimized designs by enforcing a minimum length scale on the design. Additionally a volume constraint is imposed.

Intermediate values of the impedance in the final design are in this problem not physically sound or realizable. In order to convert the converged continuous design

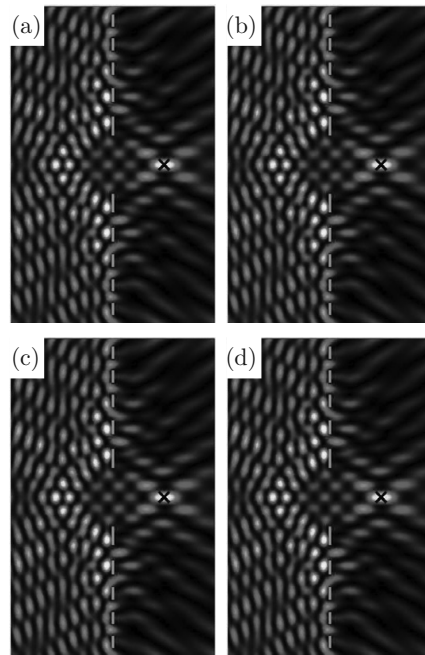


FIG. 2. Computational Domain.

into a binary zone plate, we impose a threshold value of $\eta_{threshold} = 10^2$. I.e. all elements with $\eta > \eta_{threshold} \rightarrow \eta = \eta^{max}$ and $\eta \leq \eta_{threshold} \rightarrow \eta = \eta^{min}$.

In order to focus the electromagnetic radiation, the objective is to maximize the norm of the total field at the specified focal point, as follows.

$$\Phi = \frac{1}{\Phi_0} E_z \overline{E_z} \quad (5)$$

where the bar denotes the complex conjugate and Φ_0 is the norm of the electric field at the specified focal point when no FZP is present. The reference value, Φ_0 , is included in order to make the objective dimensionless as well as easy to interpret. The gradient-based optimization routine, method of moving asymptotes (MMA)²¹, is applied to update the design in an iterative approach. The sensitivities are obtained using the adjoint method²².

NUMERICAL EXAMPLES

This work is supported from the Eurohorcs/ESF European Young Investigator Award (EURYI) and from the Danish Research Council for Technology and Production.

¹J. C. Wiltse, SPIE Proc. **2**, 722–725 (1999).

²B. Lengeler, C. G. Schroer, M. Kuhlmann, B. Benner, T. F. Gunzler, O. Kurapova, F. Zontone, A. Snigirev and I. Snigireva, J. Phys. D: Appl. Phys. **38** 10A, 218–222 (2005).

³A. V. Baez, Nature **168**, 958 (1960).

⁴L. Kipp, R. L. Johnson, R. Berndt, R. Adelung, S. Harm and R. Seemann, Nature **414**, 184–188 (2001).

- ⁵G. Z. Jiang and W. X. Zhang, SPIE Proc., **1**, 472–475 (1997).
- ⁶W. X. Zhang and G. Z. Jiang, SPIE Proc., **2**, 734–737 (1999).
- ⁷I. Minin and O. Minin, *Diffractional Optics of Millimetre Waves* (Institute of Physics Publishing, Bristol, 2004).
- ⁸J. C. Wiltse, SPIE Proc., 3062, 181–185 (1997).
- ⁹W. D. Furlan, J. A. Monsoriu and G. Saavedra, SPIE Proc., 6317, 63171B-1-9 (2006).
- ¹⁰P. Srisungsitthisunti, O. K. Ersoy and X. Xu, J. Opt. Soc. Am. A **26**, 2114–2120 (2009).
- ¹¹L. C. J. Baggen and M. H. A. J. Herben, Int. J. Infrared Milli.Waves **14**, 1341–1352 (1993).
- ¹²D. R. Reid and G. S. Smith, Microw. Opt. Tech. Lett. **51**, 2223–2227 (2009).
- ¹³M. P. Bendsøe and O. Sigmund, *Topology Optimization: Theory, Methods and Applications* (Springer-Verlag, Berlin, 2003).
- ¹⁴J. C. Wiltse, SPIE Proc., 5790, 167–179 (2005).
- ¹⁵J. Jin, *The Finite Element Method in Electromagnetics* (John Wiley & Sons Inc., New York, 2002).
- ¹⁶Comsol Multiphysics, COMSOL AB, Stockholm, www.comsol.se
- ¹⁷A. R. Diaz and O. Sigmund, Struct. Multidisc. Optim. **41**, 163–177 (2010).
- ¹⁸B. Bourdin, Int. J. Numer. Meth. Eng. **50**, 2143 (2001).
- ¹⁹T. E. Bruns and D.A. Tortorelli, Comput. Method Appl. M. **190**, 3445 (2001).
- ²⁰O. Sigmund, Struct. Multidisc. Optim. **33**, 401 (2007).
- ²¹K. Svandberg, Int. J. Numer. Meth. Eng. **25**, 359 (1987).
- ²²J. S. Jensen and O. Sigmund, J. Opt. Soc. Am. B **22**, 1191 (2005).

DTU Mechanical Engineering
Section of Solid Mechanics
Technical University of Denmark

Nils Koppels Allé, Bld. 404
DK- 2800 Kgs. Lyngby
Denmark
Phone (+45) 45 25 42 50
Fax (+45) 45 93 14 75
www.mek.dtu.dk
ISBN: 978-87-90416-71-3

DCAMM
Danish Center for Applied Mathematics and Mechanics

Nils Koppels Allé, Bld. 404
DK-2800 Kgs. Lyngby
Denmark
Phone (+45) 4525 4250
Fax (+45) 4593 1475
www.dcam.dk
ISSN: 0903-1685